Demonstration of normalized differential detection using smart pixels with smart illumination

by XiaoFang Chen

A thesis submitted in partial fulfillment of the requirements for the degree of Master of Science in Physics
Montana State University

Abstract:
Smart Pixels with Smart Illumination (SPSI) is a new concept in sensor array technology. It connects the emitters and detectors of an integrated array dynamically, which greatly improves the sensor functionality and opens the door to many exciting potential applications. We use a single pixel that consists of one Vertical Cavity Surface Emitting Laser (VCSEL) and two Metal Semiconductor Metal (MSM) detectors on an opto-electronic (OE) chip to demonstrate normalized differential detection with the SPSI concept. Our experimental data match the theoretical predictions well, which shows that normalized differential detection with the SPSI concept is practical. Two VCSEL/MSM OE chips were characterized and the data are presented in this thesis for documentation and comparison.

DEMONSTRATION OF NORMALIZED DIFFERENTIAL DETECTION USING SMART PIXELS WITH SMART ILLUMINATION

by

XiaoFang Chen

A thesis submitted in partial fulfillment
of the requirements for the degree

of

Master of Science

in

Physics

MONTANA STATE UNIVERSITY–BOZEMAN
Bozeman, Montana

May 2000

APPROVAL

of a thesis submitted by

XiaoFang Chen

This thesis has been read by each member of the thesis committee and has been found to be satisfactory regarding content, English usage, format, citations, bibliographic style, and consistency, and is ready for submission to the College of Graduate Studies.

William R. Babbitt, Ph. D — (Signature) — 5/18/00 Date

Approved for the Department of Physics

John C. Hermanson, Ph. D — (Signature) — 5-18-00 Date

Approved for the College of Graduate Studies

Bruce R. McLeod, Ph. D. — Bruce R. McLeod (Signature) — 5-25-00 Date

STATEMENT OF PERMISSION TO USE

Signature

Date May 19, 2000

ACKNOWLEDGMENTS

I would like to thank a number of people for helping me complete my project and this thesis. I send special thanks to Dr. Kevin Repasky, who designed the optical part for my project, gave me the constant support in research, read my thesis carefully and offered many suggestions on how to improve it. I own him a lot for my progress in this thesis. I am also appreciative to other members in Dr. Babbitt's lab for creating a friendly and intellectual atmosphere. I thank Norman Williams for helping me machine the metal holders for my project. I am thankful to Steve Kelly, who helped me build the printed circuit boards. I also thank Lei Meng for taking the wonderful photographs for my thesis. A warm thanks goes to Margaret Jarrett, who helped me deal with all kinds of paper work so I could focus on my research. I am obliged to Dr. Alain Tchouassi, who spent a lot of time to read my thesis and help me improve it.

I am most grateful to my advisor and mentor, Dr. William Randall Babbitt. Dr. Babbitt introduced me to this exciting topic, gave me the freedom to do this research, and was always there when I needed help. He never blamed me for my mistakes, instead he encouraged me to learn from them and felt happy when I did. His skills as a mentor helped me through every critical part of my project. His attitude towards research and life had a wonderful influence on me that cannot easily be measured.

I am indebted to my family back in China. Even though they are not here with me, I can feel their encouragement everyday. They are the source of my strength.

TABLE OF CONTENTS

Page

1. INTRODUCTION 1

2. THEORY 4

Optical Design 6
Optical Tolerance 12
Opto-Electronic Feedback Loop 20

3. OPTICAL CHARACTERIZATION 23

Layout of VCSEL/MSM chip 23
VCSEL's Performance 26
MSM Performance 39
Summary 45

4. EXPERIMENTAL 46

Optical Setup 49
Opto-Electronic Feedback Circuit 60
Results 64

5. CONCLUSION 91

REFERENCE CITED 93

APPENDIX - Electronic Feedback Circuit 97

LIST OF TABLES

Table | Page

1. Tolerance for Single Element 17
2. Tolerance for the Whole System 19
3. Polarization Characteristics of VCSEL's on Chip D3G 31
4. Responsivity and Dark Current of MSM Detectors on Chip E3F 45
5. V' Values and Percentage Deviation from V_{ref} (V_{ref} = 134.8mV) 82
6. V' Values and Percentage Deviation from V_{ref} (V_{ref} = 159mV) 84
7. V' Values and Deviations from V_{ref} (V_{ref} = 52mV, T_1^2 = 0.121) 85
8. V' Values and Deviations from V_{ref} (V_{ref} = 56.4mV, T_1^2 = 0.141) 85
9. V' Values and Deviations from V_{ref} (V_{ref} = 120mV, T_1^2 = 0.883) 86
10. V' Values and Deviations from V_{ref} (V_{ref} = 52.4mV, T_2^2 = 0.121) 88
11. V' Values and Deviations from V_{ref} (V_{ref} = 56.8mV, T_2^2 = 0.141) 89
12. V' Values and Deviations from V_{ref} (V_{ref} = 123mV, T_2^2 = 0.883) 90

LIST OF FIGURES

Figure Page

1. Schematic of the Electronics and Optics for a Single SPSI Pixel........................ 5

2. Optical Setup for a Single SPSI Pixel... 6

3. Gaussian Beam Propagation for the Optical Design of a Single SPSI Pixel........ 9

4. Schematic of Spot Image Position for Tolerance Analysis 14

5. Schematic of the Unfold System for Tolerance Calculation 15

6. Block Diagram of the Opto-Electronic (OE) Feedback Loop 20

7. Bottom View of the OE chip 24

8. Microscope Picture of the Working Area of the Vertical Cavity Surface Emitting Lasers (VCSEL's)/Metal Semiconductor Metal (MSM) Detectors Chip 25

9. Array Layout of a VCSEL's/MSM Chip.. 25

10. Physical Positions of the VCSEL's and MSM Detectors.................................. 26

11. P-I curve for 15 VCSEL's on Chip D3G.. 27

12. Threshold and Power Distribution of the VCSEL's on Chip D3G 28

13. P-I Curves for VCSEL 8 (V8) on Chip D3G.. 29

14. P-I curves of the VCSEL's on Chip D3G in 0-100μW Range........................... 30

15. Setup for Characterizing the Polarization of VCSEL's on Chip D3G 30

16. P-I Curves of VCSEL's on Chip E3F... 32

17. Threshold and Power Distribution of VCSEL's on Chip E3F 33

18. P-I Curve for V14 on Chip E3F... 34

LIST OF FIGURES--continued

Figure Page

19. Spatial Intensity and Profile Plots of V14 Beam(V14 runs at 6mA) 36
20. Spatial Intensity Plot of V14 Beam(V14 runs at 10mA) 37
21. Spatial Intensity Plot of V14 Beam(V14 runs at 20mA) 37
22. Spatial Intensity Plot of V14 Beam Focused by a Microlens (V14 runs at 10mA) 38
23. Spatial Intensity Plot of V14 Beam Focused by a Microlens (V14 runs at 6mA) 38
24. MSM Biased with 5 Volts 39
25. Setup for Measuring the Photocurrent of MSM detectors on Chip D3G 40
26. I-P Curves for MSM Detectors on Chip D3G 41
27. Setup for Measuring Responsivity of MSM detectors on Chip E3F 42
28. Responsivity of MSM Detectors on Chip E3F 43
29. Responsivity (Current Less Than 50 μA) of MSM Detectors on Chip E3F 44
30. Responsivity of Detector 13 (D13) and Detector 10 (D10) on Chip E3F 44
31. Schematic of the Experimental Setup for a Single SPSI Pixel 47
32. Photograph of the Experimental Setup for the Whole System 48
33. Schematic of the Optical Part of the Experimental Setup for a Single Pixel 49
34. Photograph of the Optical Part of the Experimental Setup for a Single SPSI Pixel 50
35a. Photograph of the Mounting for Chip E3F, the Microlens Array, 8mm Lens, and BPG 51

LIST OF FIGURES--continued

Figure Page

35b. A Detail Portion of Figure 35a Displaying the Home Made Metal Mounts 51

36. Microlens Array Plate 53

37. V14 Beam Split by the BPG (V14 Runs at 4.7mA) 58

38. V14 Beam Split by the BPG (V14 Runs at 7mA) 59

39. V14 Beam Split by the BPG (V14 Runs at 15mA) 59

40. Photograph of the Current Driver and Detector Bias Circuit 61

41. Photograph of the Electronic Feedback Circuit 61

42. Block Diagram of the OE Feedback Circuit 63

43. Beam 1 Is Attenuated by Different Value of ND Filter 67

44. V_1 Versus I and the Linear Fit ($R_1 = R_2 = 0$) 69

45. V_2 Versus I and the Linear Fit ($R_1 = R_2 = 0$) 70

46. ($V_1 - k_1I - d_{k1}$) Versus I and the Linear Fit ($R_2 = 0$) 71

47. ($V_2 - k_2I - d_{k2}$) Versus I and the Linear Fit ($R_1 = 0$) 71

48. ($V_1 - k_1I - d_{k1}$) Versus R_2I and the Linear Fit 72

49. ($V_2 - k_2I - d_{k2}$) Versus R_1I and the Linear Fit 73

50. V_1 Versus I ($T_1 = T_2 = 1$) 74

51. V_2 Versus I ($T_1 = T_2 = 1$) 74

52. V_1 Versus I ($T_1^2 = 1, T_2^2 = 0.612$) 75

53. V_1 Versus I ($T_1^2 = 1, T_2^2 = 0.487$) 76

LIST OF FIGURES--continued

Figure Page

54. V_1 Versus I ($T_1^2 = 1, T_2^2 = 0.335$) ... 76

55. V_1 Versus I ($T_1^2 = 1, T_2^2 = 0.195$) ... 77

56. V_1 Versus I ($T_1^2 = 1, T_2^2 = 0.119$) ... 77

57. V_1 Versus I ($T_1^2 = 1, T_2^2 = 0.085$) ... 78

58. V_2 Versus I ($T_1^2 = 1, T_2^2 = 0.612$) ... 78

59. V_2 Versus I ($T_1^2 = 1, T_2^2 = 0.487$) ... 79

60. V_2 Versus I ($T_1^2 = 1, T_2^2 = 0.335$) ... 79

61. V_2 Versus I ($T_1^2 = 1, T_2^2 = 0.195$) ... 80

62. V_2 Versus I ($T_1^2 = 1, T_2^2 = 0.119$) ... 80

63. V_2 Versus I ($T_1^2 = 1, T_2^2 = 0.085$) ... 81

64. Experimental V_{out} and Theoretical V_{out} ($T_1^2 = 1$) ... 82

65. Experimental V_{out} and Theoretical V_{out} ($T_2^2 = 1$) ... 83

66. Experimental V_{out} and Theoretical V_{out} ($T_1^2 = 0.121$) ... 84

67. Experimental V_{out} and Theoretical V_{out} ($T_1^2 = 0.141$) ... 85

68. Experimental V_{out} and Theoretical V_{out} ($T_1^2 = 0.883$) ... 86

69. Experimental V_{out} and Theoretical V_{out} ($T_2^2 = 0.121$) ... 88

70. Experimental V_{out} and Theoretical V_{out} ($T_2^2 = 0.141$) ... 89

71. Experimental V_{out} and Theoretical V_{out} ($T_2^2 = 0.883$) ... 90

72. Schematic of the Actual Electronic Feedback Circuit ... 99

ABSTRACT

Smart Pixels with Smart Illumination (SPSI) is a new concept in sensor array technology. It connects the emitters and detectors of an integrated array dynamically, which greatly improves the sensor functionality and opens the door to many exciting potential applications. We use a single pixel that consists of one Vertical Cavity Surface Emitting Laser (VCSEL) and two Metal Semiconductor Metal (MSM) detectors on an opto-electronic (OE) chip to demonstrate normalized differential detection with the SPSI concept. Our experimental data match the theoretical predictions well, which shows that normalized differential detection with the SPSI concept is practical. Two VCSEL/MSM OE chips were characterized and the data are presented in this thesis for documentation and comparison.

DEMONSTRATION OF NORMALIZED DIFFERENTIAL DETECTION
USING SMART PIXELS WITH SMART ILLUMINATION

XiaoFang Chen, 2000

ABSTRACT

Smart Pixels with Smart Illumination (SPSI) is a new concept in sensor array technology. It connects the emitters and detectors of an integrated array dynamically, which greatly improves the sensor functionality and opens the door to many exciting potential applications. We use a single pixel that consists of one Vertical Cavity Surface Emitting Laser (VCSEL) and two Metal Semiconductor Metal (MSM) detectors on an opto-electronic (OE) chip to demonstrate normalized differential detection with the SPSI concept. Our experimental data match the theoretical predictions well, which shows that normalized differential detection with the SPSI concept is practical. Two VCSEL/MSM OE chips were characterized and the data are presented in this thesis for documentation and comparison.

DEMONSTRATION OF NORMALIZED DIFFERENTIAL DETECTION USING SMART PIXELS WITH SMART ILLUMINATION

XiaoFang Chen, 2000

ABSTRACT

Smart Pixels with Smart Illumination (SPSI) is a new concept in sensor array technology. It connects the emitters and detectors of an integrated array dynamically, which greatly improves the sensor functionality and opens the door to many exciting potential applications. We use a single pixel that consists of one Vertical Cavity Surface Emitting Laser (VCSEL) and two Metal Semiconductor Metal (MSM) detectors on an opto-electronic (OE) chip to demonstrate normalized differential detection with the SPSI concept. Our experimental data match the theoretical predictions well, which shows that normalized differential detection with the SPSI concept is practical. Two VCSEL/MSM OE chips were characterized and the data are presented in this thesis for documentation and comparison.

Student: XiaoFang Chen
Semester of Graduation: Summer 2000
Advisor: William Randall Babbitt
Title: Demonstration of Normalized Differential Detection Using Smart Pixels with Smart Illumination
Keywords: Smart Pixels with Smart Illumination, normalized differential detection, Vertical Cavity Surface Emitting Laser (VCSEL)/Metal Semiconductor Metal (MSM) detector chip, Opto-Electronic (OE) feedback

CHAPTER 1

INTRODUCTION

Smart pixel[1-6] arrays integrate optical devices and processing electronics on a single semiconductor chip. Current research with smart pixel[7-13] arrays exploits their capability to perform parallel processing of large pixelated images. Though the major focus of smart pixels research has been optical interconnects[14-19], the image sensing applications can also take advantage of the smart pixel technology.

Generally, a scene needs to be illuminated by some kind of light source in order to be sensed by a photodetector sensor array. Conventional sensors rely on illumination that has no connection with the detectors. The simplest source of illumination is ambient light whose random nature such as its unpredictable spatial, temporal, and spectral characteristics leads to sensing problems. An improved source of illumination is built-in illumination with fixed illuminating power. The illuminating power level is set to keep the detectors within their dynamic range when light is reflected from a scene. However, the variations of reflectivity of the scene can affect the sensor performance. A scene with high reflectivity will saturate the detectors, while a scene with low reflectivity will be below the detector's noise floor. Smart pixels with smart illumination (SPSI)[20-22], as described below, is a new concept in image sensor technology. SPSI can alleviate the problem stated above, and can open the door to many potential applications. These applications[20-22] include edge detection, scribe line tracking, spotlight tracking, background subtraction, crosstalk elimination, neural networks, etc.

SPSI connects the emitters and detectors of an integrated array dynamically. Each pixel includes one emitter and one (or more) detector. The emitter is the illumination light source and its illuminating power level can be adjusted dynamically, for instance according to different reflectivities of the scene. Thus, the reflected light from the scene can be sensed by the detectors and always be within the sensor's dynamic range. This goal is reached through electronic feedback from the pixel's detectors to its emitter.

Feedback is used in electronic circuits for stabilizing amplifiers, improving bandwidth, and de-sensitizing the performance of circuit to random variations in device parameters. SPSI couples the electronic feedback to its optical path and greatly improves the sensor functionality. Using SPSI, the image itself can provide information to dynamically control the illumination. A much more efficient sensor can be made if SPSI is utilized successfully.

This thesis uses a single SPSI pixel to demonstrate normalized differential detection with the SPSI concept. The single SPSI pixel explored in this thesis consists of one laser and two detectors on an opto-electronic (OE) integrated chip. The configuration of this single SPSI pixel is depicted in Figure 1. It is one of SPSI's many configurations. The feedback is the sum of the electronic signals generated by the two detectors and can dynamically control the laser output power. The output of this system is the difference of the electronic signals generated by the two detectors and measures the normalized difference of two reflectivites. An SPSI edge detector can detect small variations in reflectivity of images whose reflectivities vary slowly spatially. The demonstration system in this thesis is very useful for the research of SPSI edge detector.

In this thesis, two OE chips were characterized. One laser and two detectors with the best qualities were selected to comprise the single SPSI pixel. The optical part of the pixel was designed and the optics were aligned successfully. The electronic circuits for the pixel were built and performed excellently. The simple model of the single SPSI pixel was modified to describe the experimental system. The experimental results match the prediction of the new model well.

This thesis is organized as follows.

Chapter 2 uses the demonstration system to explain SPSI concept. The optical design for a single SPSI pixel is described. In this thesis, a binary phase grating forms the basis of an optical train used to demonstrate SPSI. The tolerance of the optical system is studied. The block diagram of the OE feedback circuit is described.

Chapter 3 describes the characteristics of the OE chip being used. The power-current (P-I) relationship of the lasers and polarization properties are characterized. The method of determining the spot size of the laser is described. The current-power relationship (I-P) of the detectors is presented.

Chapter 4 describes the optical and electronic setup for the demonstration of SPSI. The alignment procedure is described and accuracy of the alignment is studied. Finally, experimental results are compared with theoretical calculations

A brief discussion of the results is presented in Chapter 5.

CHAPTER 2

THEORY

SPSI pixels can have many configurations. One possibility is illustrated in Figure 1, which represents a single pixel performing normalized differential detection, the building block for an SPSI edge detector. This configuration is explored in this thesis. The light output of the laser, P_{out}, is split by a binary phase grating into two equal-intensity beams. Those two beams illuminate two adjacent spots (1 and 2) on the object. The two spots have reflectivity of $\Re_1$ and $\Re_2$. The beam reflected by spot 1 is split by the grating again. One of the split beam (P_1) is focused onto detector 1 (D_1) and the other split beam is focused back to the laser. Similarly, the beam reflected by spot 2 is split into two beams, one of which (P_2) is focused to detector 2 (D_2) and the other one is focused back to the laser. Although about half of P_{out} is fed back to the laser, no instability of the laser operation is observed in the experiment. Other configurations have been suggested to alleviate this loss in efficiency and feedback into the laser, but require polarization control of the lasers, which is not available yet. The electronic circuit generates some voltage signal V_1 (V_2) proportional to the illuminating power P_1 (P_2) on the detector. The sum (V') of V_1 and V_2 is compared to a pre-set reference voltage V_{ref}. The output voltage of the comparator modulates the output of the current driver and therefore modulates P_{out}. P_{out} is adjusted automatically through the optical and electronic

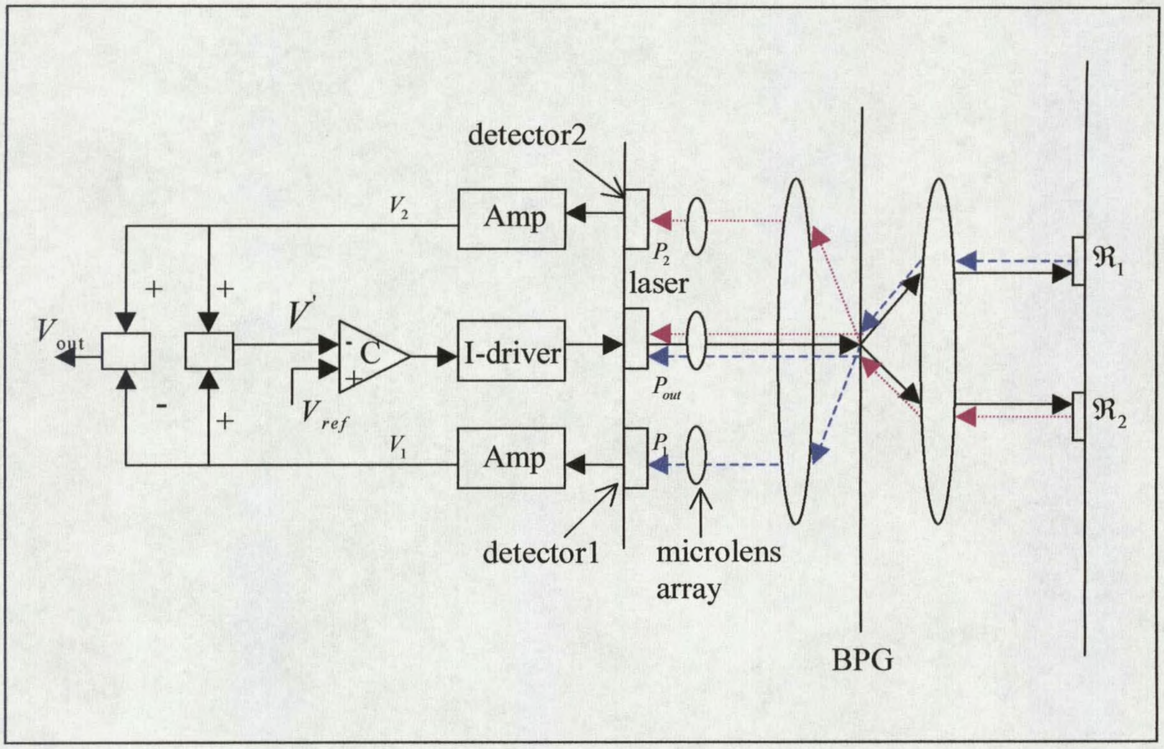

Figure 1. Schematic of the electronics and optics for a single SPSI pixel. C is a comparator, Amp is an amplifier, I-driver is a current driver, BPG is a binary phase grating. $\Re_1$ and $\Re_2$ are reflectivities of the two spots on the object.

feedback. For example, when V' is less than V_{ref}, the feedback function will make P_{out} increase. On the other hand, when V' is more than V_{ref}, the feedback function will make P_{out} decrease. This forces the total laser output that is proportional to V' to be adjusted so that $V' = V_{ref}$. Since $V' = V_1 + V_2$, this means the average optical power on the detectors is held constant. This can be used to keep the detectors in their optical operating range. The output of the pixel, V_{out}, is the difference between V_1 and V_2. V_{out} is proportional to the normalized difference of the reflectivities: $\frac{\Re_2 - \Re_1}{\Re_2 + \Re_1}$. This will be shown in section 3 of this chapter.

Optical Design

Figure 2 shows a schematic of the optical part of a single SPSI pixel. The task of the optical train is to split the outgoing laser beam into two beams for illuminating two spots on the object. Then, it images the illuminated spots onto corresponding detectors. A binary phase grating (BPG) is used to split the laser beam. The f-to-f Fourier imaging[23]

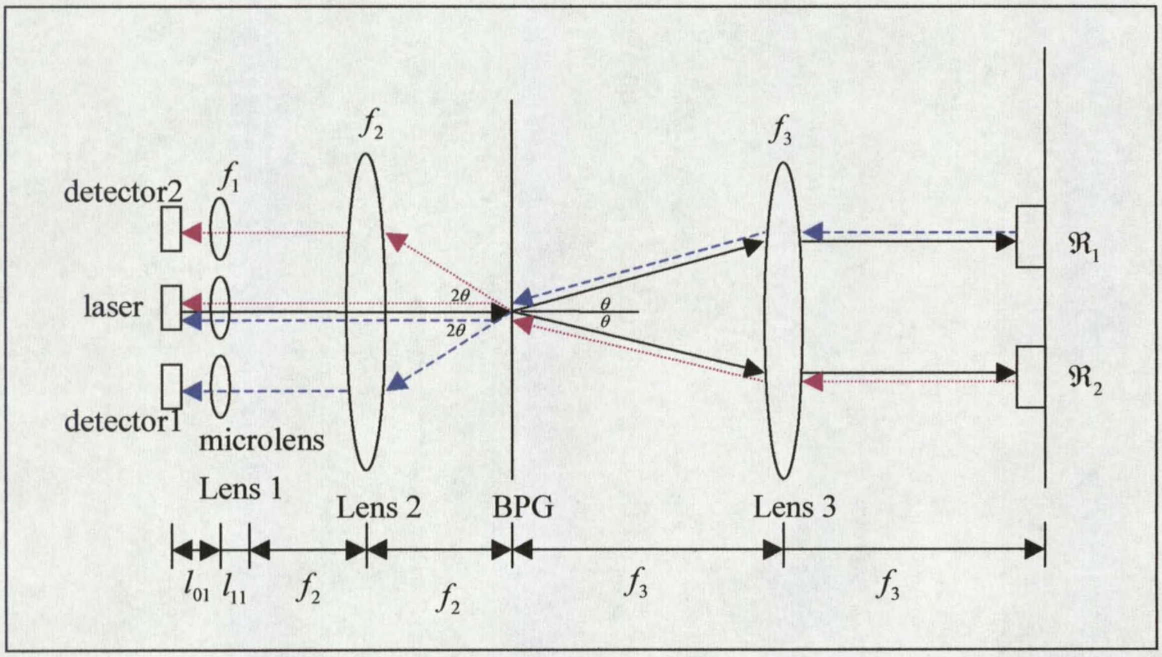

Figure 2. Optical setup for a single SPSI pixel. BPG is a binary phase grating. l_{01} is the distance between the microlens and the laser waist radius[24], l_{11} is the distance between the microlens and the new waist radius after the laser beam passes through the microlens, f_1 is the focal length of the microlens, f_2 is the focal length of Lens 2, f_3 is the focal length of Lens 3.

is used in this optical setup. The beam of the laser used in this thesis expands very quickly. Therefore, a lens with a very short focal length is needed to collect as much laser light as possible. For this reason, a microlens array with a focal length (f_1) of $672\mu m$ designed by Charlie Kuzis of University of Southern California and Allan Willner of Digital Optics Corporation was used in this thesis. To make the whole optical system compact, lens 2 should have a short focal length (f_2). An $8mm$ lens was chosen as lens 2[25]. Once lens 2 is chosen and the center-to-center distance of the detector and laser is known, the period of the BPG can be calculated so that the laser beam will be imaged onto the detectors. With the $8mm$ lens as lens 2, a BPG with a period of $77\mu m$ designed by Kevin Repasky of Montana State University was used. A considerable number of periods of the BPG need to be illuminated for the BPG to work efficiently (large ratio of spot separation to spot size). That means the spot on the BPG can not be too small. For example, if the laser beam is less than $77\mu m$ so that only half a period is illuminated, then the split will be less than a beam width. The required size of the spot on the BPG determines the microlens position since lens 2 (f_2) is used in an f-to-f imaging configuration. The calculations for designing the BPG period and determining the microlens position are given in the following part of this section. Lens 3 with a different focal length determines the distance between the two laser spots on the object. In the actual experiment those two spots need to be separated so that a neutral density (ND) filter can be positioned to attenuate one laser beam without affecting the other one. To this end, a $500mm$ lens is used for f_3. In the experiment, a mirror and ND filters are used to simulate the object.

The BPG used in this thesis produces two strong first diffraction orders[26]. The relative intensity of each of the first orders is 40.5% as compared to 5% for each of the third orders[26]. Equation (1) describes the period of the BPG[26], where d is the period, λ is the wavelength, D is the spatial shift from one order to the next order, s is the distance between the grating and the output plane:

$$d = \frac{\lambda s}{D} \tag{1}$$

It can been seen from Figure 2 that if lens 3 is taken as the output plane and the spatial shift from the 0_{th} order to the 1_{st} order is considered, then $s = f_3$ and $D = f_3 \tan(\theta)$. After the values of s and D are plugged into Equation (1), Equation (2) yields:

$$d = \frac{\lambda}{\tan(\theta)} \tag{2}$$

To find the value of d, the value of θ needs to be determined first. From Figure 2 one sees that the angle θ can be described by Equation (3), where L is the center-to-center distance between the detector and the laser:

$$\tan(2\theta) = \frac{L}{f_2} \approx 2\theta \qquad \text{for } \frac{L}{f_2} \ll 1 \tag{3}$$

The center-to-center distance is $L = 176.8\mu m$ for the OE chip used in this thesis. The focal length of lens 2 is $f_2 = 8mm$. From Equation (3), $\theta = 0.63^\circ$. The laser used in the experiment has $\lambda = 0.85\mu m$. With the values of θ and λ, Equation (2) yields $d = 77\mu m$.

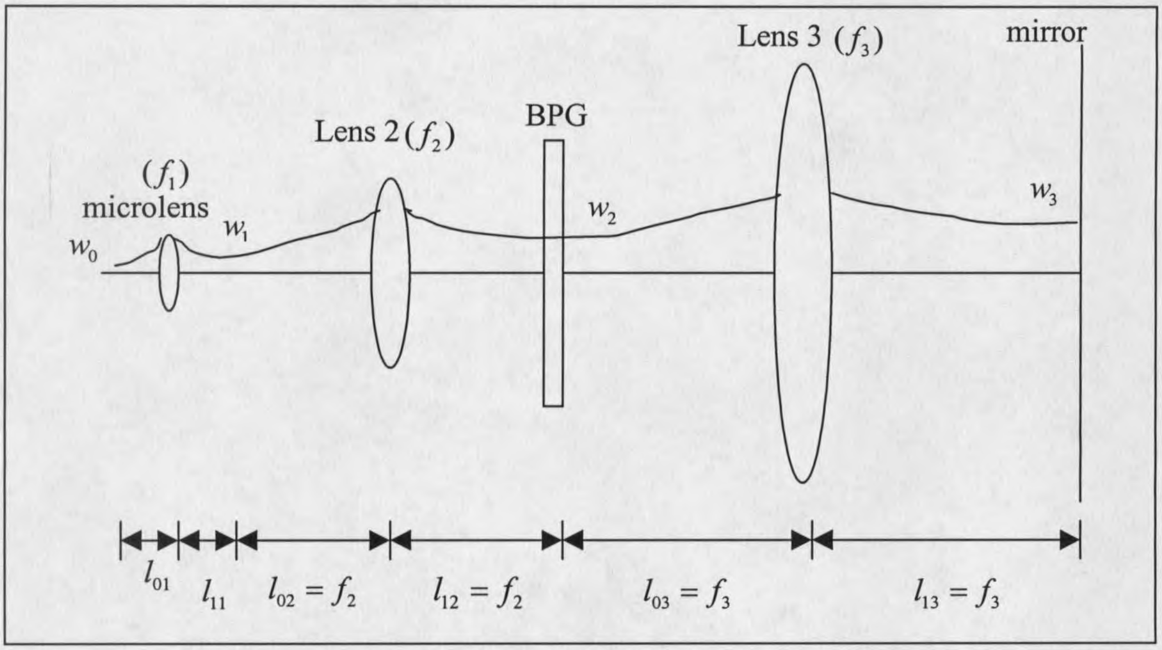

Figure 3. Gaussian beam propagation for the optical design of a single SPSI pixel. w_0 is the waist radius at the output of the laser, w_1 is the waist radius of the laser beam after it passes through the microlens, w_2 after it passes through lens 2, w_3 after it passes through lens 3. w_2 is at the BPG position, w_3 is at the mirror position. l_{01} is the distance between the positions of w_0 and the microlens, l_{11} is the distance between the positions of the micorlens and w_1. The distance between the positions of w_1 and lens 2 is f_2. The distance between the positions of lens 2 and the BPG is also f_2. The distance between the positions of the BPG and lens 3 is f_3. The distance between the positions of lens 3 and the mirror is also f_3.

Gaussian beam propagation is needed to determine the microlens' position. Figure 3 illustrates the laser beam propagation through the whole optical system ignoring the small angular deviation introduced by the BPG. As stated before, w_2 should be as big as possible for the laser beam to illuminate as many periods of the BPG as possible. However the size of w_2 is limited by the size of the mircolens. A big w_2 will lead to a small w_1 while a small w_1 will lead to a large spot (w_a) at the microlens. If w_a is bigger than the microlens' half width (W_m), less light can be collected. The criterions for w_2 and w_a are described by Equation (4) and (5) respectively. There is a trade-off between these two criterions. We try to meet the requirement of Equation (4) without sacrificing Equation (5) too much. This is because in order to get the system work, it is more important to have the BPG work efficiently.

$$w_2 \geq 2.5d \tag{4}$$

$$w_a < W_m \tag{5}$$

where $W_m = 88.5\mu m$ is the half width of the microlens (see Figure 36 in chapter 4), $d = 77\mu m$ is the period of the grating. According to the theory of Gaussian beam transmission through optical components[27], w_1 and w_a can be stated as Equation (6) and (7) respectively.

$$w_1 = \frac{\lambda f_2}{\pi w_2} \tag{6}$$

$$\begin{aligned} w_a &= w_0\sqrt{1+\left[l_{01}/\left(\pi w_0^{\ 2}/\lambda\right)\right]^2} \\ &\approx w_0\, l_{01}/\left(\pi w_0^{\ 2}/\lambda\right) \qquad \text{since } \left[l_{01}/\left(\pi w_0^{\ 2}/\lambda\right)\right]^2 \gg 1 \\ &= \lambda l_{01}/\left(\pi w_0\right) \end{aligned} \tag{7}$$

When we designed the optical part of the single SPSI pixel, we were told that the beam radius at the output of the laser w_0 is $5\mu m$, the VCSEL wavelength λ is $0.85\mu m$. From Equation (4) and (6) we get the criterion for w_1:

$$w_1 \le 11.2\mu m \tag{8}$$

From Equation (5) and (7) we get the criterion for l_{01}:

$$l_{01} < 1635\mu m \tag{9}$$

The relationship among w_1, l_{01} and l_{11} can be described by Equation (10) and (11)[27]:

$$l_{11} = \frac{f_1\gamma^2 - f_1^2 l_{01} + f_1 l_{01}^2}{\gamma^2 + f_1^2 - 2f_1 l_{01} + l_{01}^2} \tag{10}$$

$$w_1 = \sqrt{\frac{\lambda^2}{\pi^2 w_0^2}\left[(1-\frac{l_{11}}{f_1})^2\gamma^2 + (l_{01} + l_{11} - \frac{l_{01}l_{11}}{f_1})^2\right]} \tag{11}$$

Where $\gamma = \dfrac{\pi w_0^{\ 2}}{\lambda}$

With a laser beam $w_0 = 5\mu m$, Equation (8) and (9) can be easily satisfied. We picked $w_1 = 11.2\mu m$ and got $l_{01} = 957.4\mu m$ and $l_{11} = 2104.2\mu m$. Then, we designed and machined the metal holders (see section 1 of chapter 4) for the optical devices before the OE chip and the microlens array arrived. However, when we experimentally measured w_0 of the laser used in the experiment, it turned out that $w_0 = 1.38\mu m$ (see section 2 in chapter 3). The criterion for l_{01} becomes:

$$l_{01} < 451.5\mu m \tag{12}$$

When $l_{01} = 451.5\mu m$ is plugged into Equation (10) we get a negative value for l_{11}. Nonetheless, we want l_{11} to have positive value in this system, which means l_{01} needs to be larger than $f_1 = 672\mu m$. The reason we want l_{11} to have positive value is because experimentally we can not position the $8\,mm$ lens and the microlens much closer than $8\,mm$ (see Figure 35b). Though Equation (12) can not be satisfied, from this criterion we know that we need the value of l_{01} to be as close to $672\mu m$ as possible while satisfying Equation (8) at the same time. We plug $w_1 = 11.2\mu m$ (the maximum value that satisfies Equation (8)) and Equation (10) into Equation (11) and get $l_{01} = 754.5\mu m$. Then we plug $l_{01} = 754.5\mu m$ into Equation (10) and get $l_{11} = 6106.2\mu m$.

With $l_{01} = 754.5\mu m$, $w_a = 150\mu m$ is much larger than $W_m = 88.5\mu m$, the outgoing beam is clipped by the microlens. Nevertheless, we got satisfactory results with our setup.

With the values of l_{01}, l_{11}, f_1, f_2, f_3 and d, it can be seen from Figure 3 that the design of the optical system is completed.

Optical Tolerance

The optical system described in the previous section will image the illuminated spots on the object to the detectors. However, any mis-alignment of the optical components being used will introduce errors to the imaging. Therefore, it is important to find out the requirements of the alignment tolerances and if those requirements can be met in the experiment. The study of the optical tolerances is given below and shows that the requirements can be met.

In order to provide sufficient information to modulate the laser output and reduce the optical crosstalk between the two detectors of the single SPSI pixel, the $1/e$-width of the rays of the spot image should be within the detector area. This leads to the major alignment tolerance requirements. The alignment tolerance requirements can be describe by the criterion defined in Equation (13), where L is the center-to-center distance between the detector and the laser, L' is the distance between the center of the spot image on the detector and the center of the laser, w_0' is the beam radius of the spot image, w_{det} is the half width of the detector (see Figure 4). Rotational error is correctable with fine rotational control of the BPG and is thus not included in the tolerance analysis. The alignment criterion is:

$$w_0' + |L' - L| < w_{det} \tag{13}$$

The optical design under perfect alignment is $L' = L$ and $w_0' = w_0$. It can be seen from Equation (13) and Figure 4 that if the center of the spot image is at the center of the detector, which means $|L' - L| = 0$, the spot image can have a beam radius w_0' as large as the half width of the detector w_{det}, while the $1/e$-width of the rays of the image is still within the detector area. On the other hand, if the spot image is very tiny (w_0' is very small), the center of the spot image can be off the center of the detector about w_{det}, while the $1/e$-width of the rays of the image is still within the detector area. To simplify the analysis, Equation (13) can be broken into two conditions, which imposes only slightly

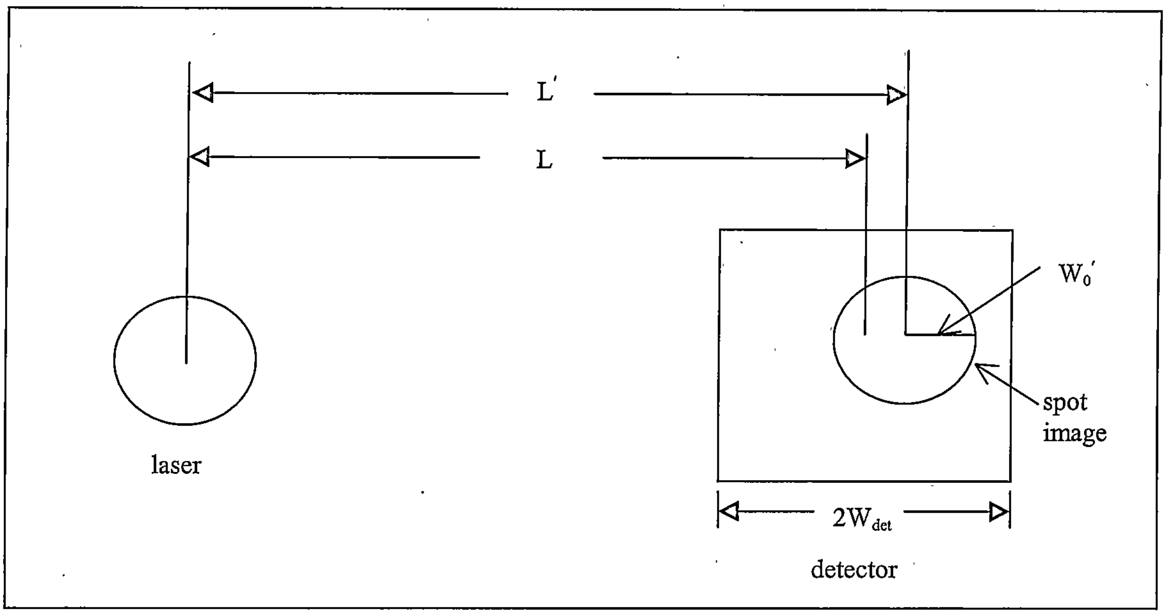

Figure 4. Schematic of spot image position for tolerance analysis. L is the center-to-center distance between the laser and the detector. L' is the center-to-center distance between the laser and the spot image on the detector. w_0' is the beam radius of the spot image.

more stringent alignment tolerances. When both conditions are satisfied simultaneously, Equation (13) is satisfied. These conditions are:

$$w_0' < \frac{w_{det}}{2} \tag{14a}$$

$$|L' - L| < \frac{w_{det}}{2} \tag{14b}$$

Since Equation (14a) deals with the size of the beam radius of the spot image, Gaussian beam propagation method is necessary to analyze it. Equation (14b) deals with the position of the spot image and ray tracing is used for its analysis. In general, it was found that Equation (14a) was a more stringent requirement than Equation (14b)(i.e., an optical alignment that satisfied Equation (14a) always satisfied Equation (14b).) Once alignment tolerances that satisfied Equation (14a) were found, they were checked to confirm that they also satisfied Equation (14b). Thus, the analysis just concentrates on satisfying Equation (14a).

To perform the analysis of the system from the laser to the mirror and back, the optical design was unfolded, as shown in Figure 5. An excel program was written to analyze both the ray tracing and Gaussian beam propagation for this setup.

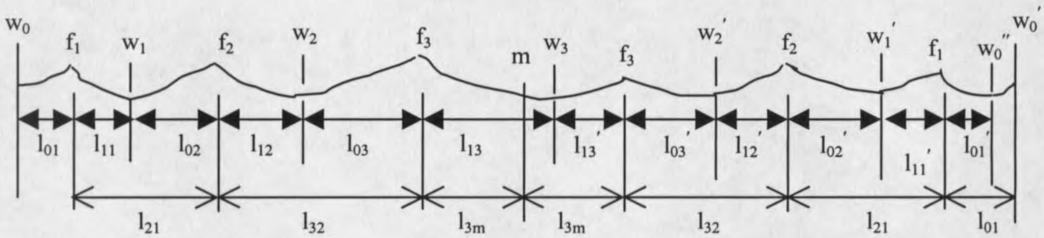

Figure 5. Schematic of the unfold system for tolerance calculation. m is a mirror.

The waist w_0 is the waist radius at the output of the laser, w_1 is waist radius of the beam after the microlens (f_1), w_2 after the $8mm$ lens (f_2), and w_3 after the $500mm$ lens (f_3). As the beam travels out to the mirror, the waist w_3 may occur before or after the mirror. The waist $w_2^{'}$ is the waist after f_3, $w_1^{'}$ is the waist after f_2, $w_0^{"}$ is the waist after f_1, and $w_0^{'}$ is the beam radius on the detector as the beam propagates back to the chip. l_{01} is the distance between the positions of w_0 and the microlens (f_1), l_{11} is the distance between the positions of the microlens (f_1) and w_1, l_{02} is the distance between the positions of w_1 and the $8mm$ lens (f_2), l_{12} is the distance between the positions of the $8mm$ lens (f_2) and w_2, l_{03} is the distance between the positions of the $500mm$ lens (f_3) and w_2, l_{13} is the distance between the $500mm$ lens (f_3) and w_3. l_{13}' is the distance between w_3 and f_3, l_{03}' is the distance between f_3 and w_2', l_{12}' is the distance between w_2' and f_2, l_{02}' is the distance between f_2 and w_1', l_{11}' is the distance between w_1' and f_1, l_{01}' is the distance between f_1 and w_0''. l_{21} is the distance between f_1 and f_2, l_{32} is the distance between f_2 and f_3, l_{3m} is the distance between f_3 and the mirror.

The value of w_0 is experimentally measured (see section 2 in chapter 3) and is used in the calculation for the microlens position. Hence, any error in this measurement will bring in inaccuracy to the imaging property of the system. The mis-alignment of the optical components means l_{01}, l_{21}, l_{32} and l_{3m} are not the same as their designed values. So w_0, l_{01}, l_{21}, l_{32} and l_{3m} are the variables which need to be investigated.

Given the values of w_0, l_{01}, l_{21}, l_{32} and l_{3m}, one can use the excel program to calculate the value of w_0'. If the measurement of $w_0 = 1.38\mu m$ is correct and l_{01}, l_{21}, l_{32} and l_{3m} all equal their designed values, w_0' equals w_0 and Equation (14a) is satisfied ($w_{det} = 37.5\mu m$ for the detector used in the experiment).

Our first approach to satisfying Equation (14a) is to assume that the influences of w_0, l_{01}, l_{21}, l_{32} and l_{3m} on the system are somewhat linear (i.e., the misalignment due to these errors add), so that Equation (14a) can be further simplified to Equation (15). If the deviation of each variable changes the beam radius of the spot image by an amount of $|w_0' - w_0|$, and the change satisfies Equation (15), the $1/e$-width of the rays of the spot image will remain within the detector area when all five changes are added together, assuming the changes are roughly independent.

$$|w_0' - w_0| < \frac{\frac{w_{\text{det}}}{2} - w_0}{5} \qquad (15)$$

To analyze the effect of each variable to first order, the other variables are held fixed. For example, to analyze the effect of the deviation of w_0 on the value of w_0' to first order, one sets l_{01}, l_{21}, l_{32} and l_{3m} to their designed values then varies the w_0 value to find out the maximum deviation of it when Equation (15) is no more satisfied. This approach is used to find out the maximum deviations of the five variables. The results are presented in Table 1. The values given are $\frac{\pm\Delta X}{X}$ in percentage.

X	$-\Delta X/X$	$+\Delta X/X$
w_0=1.38μm	-50%	50%
l_{01}=754.5μm	-1.90%	1.40%
l_{21}=14106.2μm	-10.00%	10.00%
l_{32}=508000μm	-40%	40%
l_{3m}=500000μm	-40%	40%

Table 1. Tolerance for single element.

When calculating the tolerance, we notice that a small deviation of l_{02} will cause huge deviation on l_{12}. For example, the designed value for l_{02} is $8mm$, then from Equation (16)[27] l_{12} can be calculated to be $8mm$ as well. However, if l_{02} becomes $8.001mm$, l_{12} is calculated as $8.296mm$. $1\mu m$ deviation of l_{02} causes $298\mu m$ deviation of l_{12}. This can be explained by examining the relationship between l_{12} and l_{02} more closely[26].

$$l_{12} = \frac{f_2\gamma_2^{\ 2} - f_2^{\ 2} l_{02} + f_2 l_{02}^{\ 2}}{\gamma_2^{\ 2} + f_2^{\ 2} - 2f_2 l_{02} + l_{02}^{\ 2}} \tag{16}$$

where $\gamma_2 = \frac{\pi w_1^{\ 2}}{\lambda}$, $w_1 = 11.2\mu m$, $\lambda = 0.85\mu m$, $f_2 = 8mm$

If Δ is used to symbolize the deviation of l_{02}, $l_{02}^{"}$ to symbolize the position of the new spot size when l_{02} is deviated by Δ from the designed value, Equation (16) becomes:

$$l_{12}^{"} = \frac{f_2\gamma_2^{\ 2} - f_2^{\ 2}(l_{02}+\Delta) + f_2(l_{02}+\Delta)^2}{\gamma_2^{\ 2} + f_2^{\ 2} - 2f_2(l_{02}+\Delta) + (l_{02}+\Delta)^2} \tag{17}$$

Since $l_{02} = f_2$, Equation (17) can be simplified as (assuming $\Delta << \gamma_2$):

$$l_{12}^{"} = f_2 + (\frac{f_2}{\gamma_2})^2 \Delta \tag{18}$$

where $(\frac{f_2}{\gamma_2})^2 = 297.7$

Now, it is obvious that for every deviation Δ of l_{02}, l_{12} will have deviation of 297.7Δ. However, as long as the deviation of l_{21} is within tolerance, a change of l_{12} will not cause a huge change in w_0'.

Unfortunately, when $w_0 = 1.38\mu m(1+50\%)$, $l_{01} = 754.5\mu m(1+1.4\%)$, $l_{21} = 8mm(1+10\%)$, $l_{32} = 500mm(1+40\%)$ and $l_{3m} = 500mm(1+40\%)$ are used to calculate w_0', it turns out that Equation (14a) is not satisfied. w_0' is off $\frac{w_{\det}}{2}$ by 116%. This means the effects of the deviation of each variable can not be simply added together.

While the linear analysis is instructive to determine the critical tolerance of individual elements, another approach is needed to analyze the system. First, the accuracy of positioning each optical element is estimated. We start by assuming l_{21}, l_{32} and l_{3m} can be positioned to ±1mm, ±5mm, and ±5mm respectively. The ±1% errors for f_2 and f_3 also take into account error in the specified focal lengths. Our estimated error in the measurement of w_0 is ±7%. There are 16 possible combinations of these errors. For each, a positive and negative tolerance on l_{01} can be found. The smallest (tightest) tolerance of these is reported in table 2.

	l_{01}=754.5μm	l_{21}=14106.2μm	l_{32}=508000μm	l_{3m}=500000μm	w_0=1.38μm
tolerance	±1.4%	±7%	±1%	±1%	±7%

Table 2. Tolerance for the whole system.

We see that our ability to position/measure l_{21}, l_{32}, l_{3m} and w_0 to high precision allows us to use their tolerance "quota" to relax the accuracy on l_{01}. The tolerance of ±1.4% of l_{01} is within our experimental precision, since the value of l_{01} is set by measuring w_0 to ±7% which yields a ±0.8% error in l_{01} that is less than the tolerance.

Opto-Electronic Feedback Loop

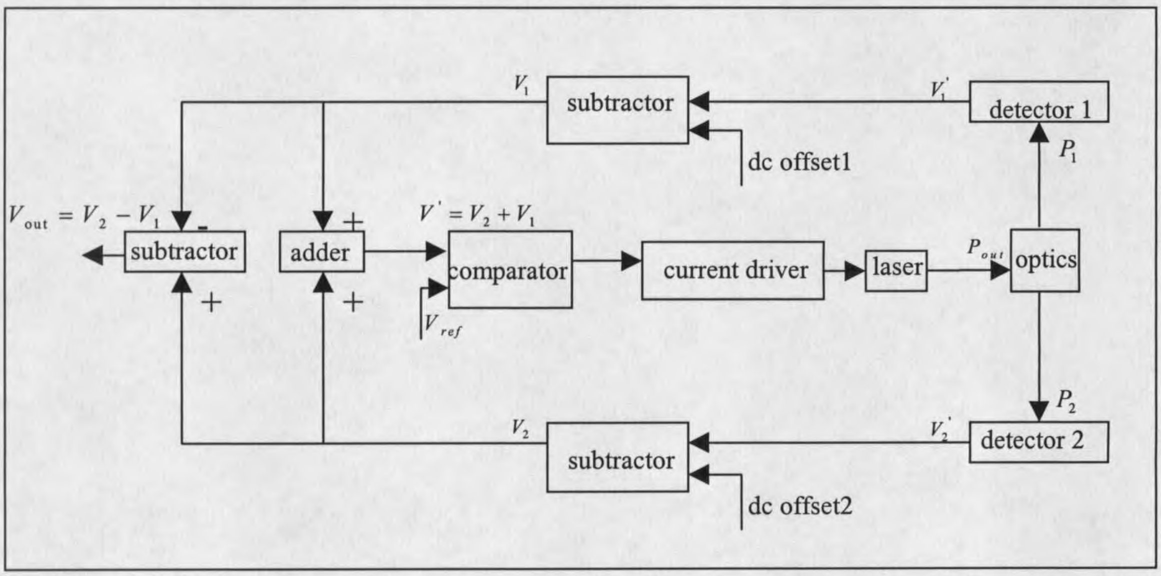

Figure 6. Block diagram of the opto-electronic feedback loop.

Figure 6 is the block diagram of the opto-electronic feedback loop. P_1 (P_2) represents the laser power on detector 1 (detector 2). When P_1 (P_2) is incident on detector 1 (detector 2), voltage V_1' (V_2') will be generated. The subtractor right after the detector is used to subtract the dc offset of the detector, producing V_1(V_2). $V_{out} = V_2 - V_1$ is the voltage output of the system. $V' = V_1 + V_2$ is fed to a comparator and compared to a pre-set voltage V_{ref}. The output of the comparator will be used to modulate the laser power P_{out}. $V_1(V_2)$ is proportional to $P_1(P_2)$. Equations (19) and (20) describe V_{out} and V' respectively.

$$V_{out} = V_2 - V_1 = \alpha P_2 - \alpha P_1 = \alpha(\Re_2 - \Re_1)P_{out} \tag{19}$$

$$V' = V_2 + V_1 = \alpha P_2 + \alpha P_1 = \alpha(\Re_2 + \Re_1)P_{out} \tag{20}$$

where α is the detector responsivity and $\Re_1$ and $\Re_2$ are the reflectivities of the two spots of the object. When the system is stable with sufficient gain (and is not limited in laser output):

$$V' = V_{ref}. \tag{21}$$

It can be seen from Equation (20) and Equation (21) that with a constant V_{ref}, the laser output P_{out} will change as the reflectivity of the object changes. If the reflectivity of the region is low, P_{out} will increase so the image will not be buried in the detector's noise. On the other hand, if the reflectivity of the region is high, P_{out} will decrease so the image will not saturate the detector.

From Equations (19), (20) and (21), V_{out} can be written:

$$V_{out} = \frac{\Re_2 - \Re_1}{\Re_2 + \Re_1} V_{ref} \tag{22}$$

V_{out} depends on the reflectivities of the two spots $\Re_1$, $\Re_2$ and the reference voltage V_{ref}. The laser power P_{out} and the detector responsivity α do not appear in the equation of V_{out}. So the output of the system V_{out} is de-coupled from the variation of the characteristics of the laser. As long as the laser output P_{out} can be changed enough to maintain the condition $V_{ref} = V_1 + V_2$, the actual power-current relation of the laser will not affect the performance of the system. V_{out} measures the normalized difference between two reflectivites. Therefore, an array of such pixels will be able to measure the normalized slope of the reflectivies of a scene. This functionality is well suited to carry out the edge detector function[20-22].

CHAPTER 3

OPTICAL CHARACTERIZATION

A combination of one Vertical Cavity Surface Emitting Laser (VCSEL) and two Metal Semiconductor Metal (MSM) detectors on an OE chip constitute a single SPSI pixel in this thesis. The OE chip was fabricated by Honeywell Corporate Technology Center. Each OE chip has an integrated 4x4 array of VCSEL's and MSM detectors on it (see Figure 8). All VCSEL's and MSM detectors on the chip were characterized so the VCSEL and MSM detectors with best qualities could be selected to compose a single SPSI pixel.

Two OE chips were characterized. The first one is labeled as D3G and the second one as E3F. They are identical in wiring, mapping and packaging. Because some damage was caused to our first chip Chip D3G half way through the experiment, Chip E3F was then characterized and used to carry out the experiment. The characterization for both chips is presented in this chapter for documentation and comparison.

In each section, except the one providing the chip layout information, the first part presents the data from Chip D3G and the second part presents data from Chip E3F.

Layout of VCSEL/MSM chip

The OE is packaged and wire-bonded to provide external access to single VCSEL's and detectors. The VCSEL's have a common cathode that is connected to two pins. Each VCSEL has a single anode that is connected to a single external pin. Each

MSM detector has two connections to two pins. Therefore, the whole chip has 18 pins for the VCSEL's and 32 for the MSM detectors. Figure 7 is the bottom view of the package. The round dots stand for pins. There are 68 pins all together. 50 of them are connected to VCSEL's and MSM detectors; the others are not connected. The top view of the working area of the package is shown in Figure 8.

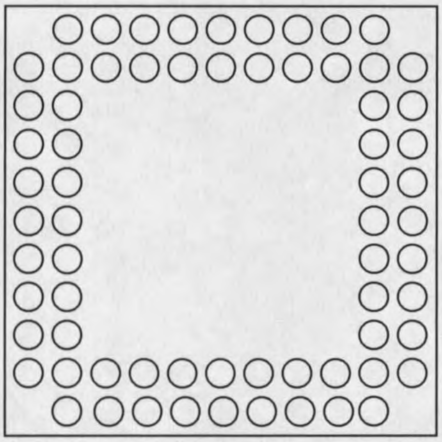

Figure 7. Bottom view of the OE chip. The round dots are pins.

Figure 8 is a microscope picture of the working area of a real chip. In this picture, the round dots are VCSEL's and the squares are MSM detectors. Figure 9 is the layout of the OE chip. The proton-implanted VCSEL's have $15\mu m$ apertures. The wavelength of the VCSEL light is $850nm$. The center-to-center spacing of the VCSEL's is $250\mu m$. The MSM detector size is $75\times 75\mu m$. The center-to-center spacing of the detectors is also $250\mu m$.

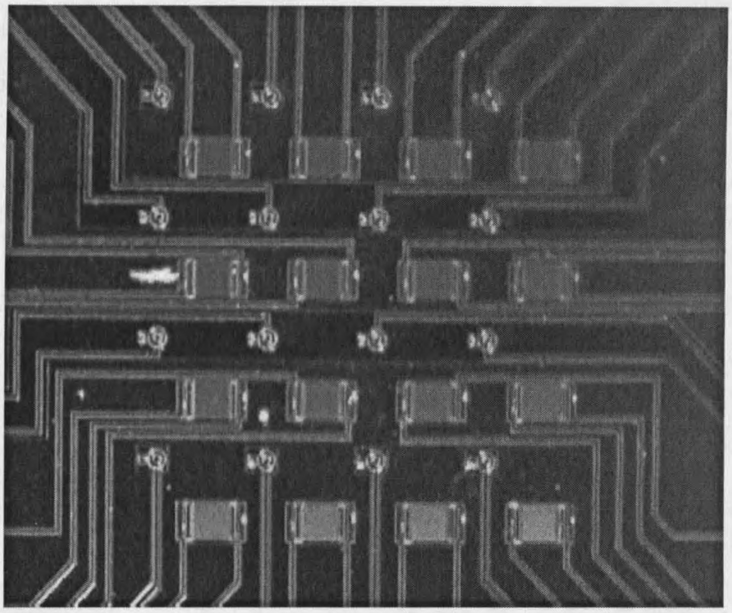

Figure 8. Microscope picture of the working area of the VCSEL's/MSM chip. The round dots are VCSEL's, the squares are MSM detectors, and the lines are wires connected to the pins on the bottom side of the chip. Each VCSEL has an anode connection. The common cathode connection can not be seen on this picture. Each MSM detector has two connections.

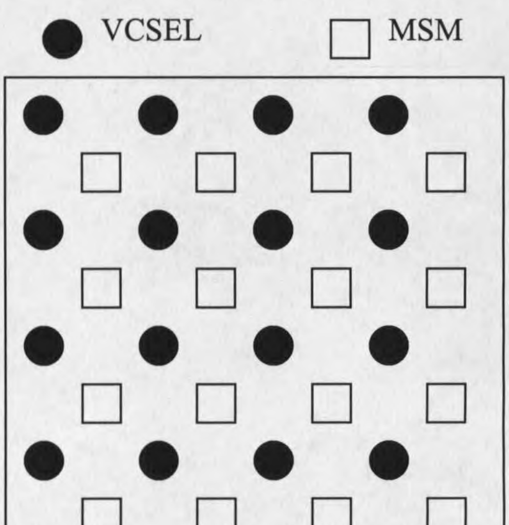

Figure 9. Array layout of a VCSEL's/MSM chip.

VCSEL's Performance

V-VCSEL D-MSM detector

V1		V2		V3		V4	
	D1		D2		D3		D4
V5		V6		V7		V8	
	D5		D6		D7		D8
V9		V10		V11		V12	
	D9		D10		D11		D12
V13		V14		V15		V16	
	D13		D14		D15		D16

Figure 10. Physical positions of the VCSEL's and MSM detectors.

Figure 10 shows the labeling used for the VCSEL's and MSM detectors on the OE chips (D3G and E3F). Another observation of Chip D3G under the microscope showed that VCSEL 1 (V1) is not connected. The other 15 VCSEL's were characterized. An ILX Lightwave Corporation current driver was used to drive the VCSEL's, and a wide area photo-detector was positioned as close to the chip as possible to measure the output power of the laser. Figure 11 is a plot of the output power as a function of the driving current for the 15 VCSEL's on Chip D3G. The maximum current used to drive the VCSEL's on Chip D3G was $10\,mA$ because that was the operating current. The error of the power reading was estimated to be $\pm 5\%$.

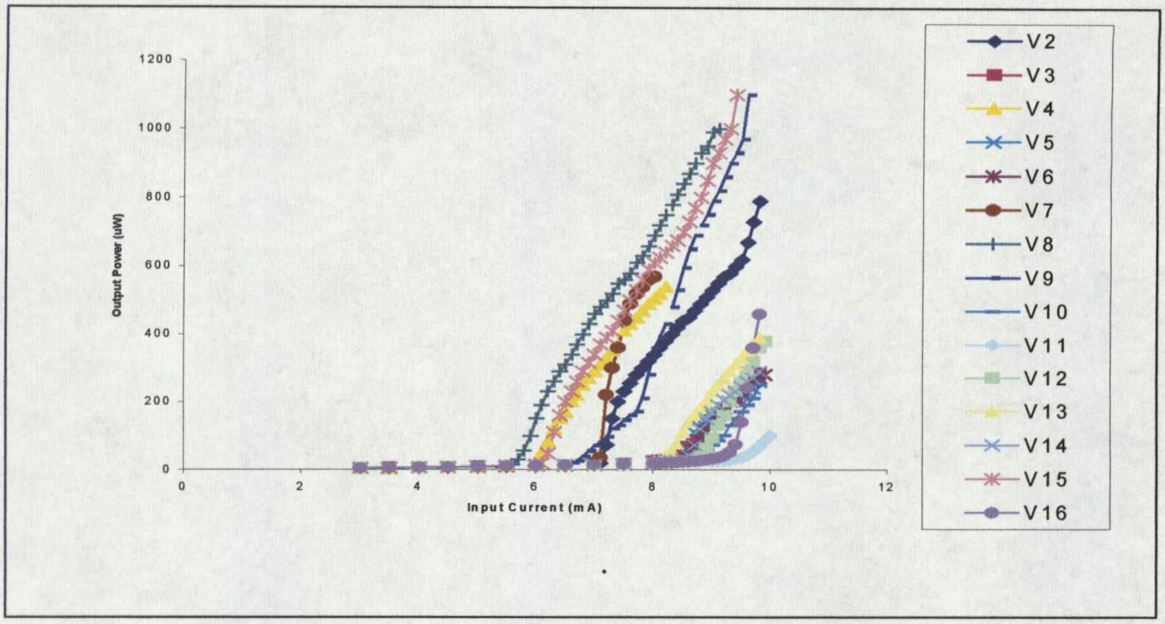

Figure 11. P-I curve for 15 VCSEL's on Chip D3G.

From the P-I curves, the threshold of each VCSEL was determined and is shown in Figure 12, along with output powers at $10\,mA$. Figure 12 shows that the threshold of the VCSEL's on Chip D3G varies from $5.8\,mA$ to $9.3\,mA$, the output power at $10\,mA$ varies from $100\,\mu W$ to $1100\,\mu W$. The VCSEL's on Chip D3G can be roughly divided into two groups; one group has low threshold ($\leq 7.2mA$) and high output power ($\geq 550\,\mu W$) at $10\,mA$, the other group had high threshold ($\geq 8.2mA$) and low output power ($\leq 490\,\mu W$) at $10\,mA$. That shows that the VCSEL's on Chip D3G do not have very good uniformity. But the variations are not correlated with the physical positions of the VCSEL's on the chip.

Threshold (mA)

	7.2	8.5	6.0
8.5	8.5	7.2	5.8
6.5	8.5	9.2	8.8
8.2	8.5	6.0	9.3

Output power (μW) at $10\,mA$

	800	100	550
290	300	580	1000
1100	300	100	390
400	300	1100	490

Figure 12. Threshold and power distribution of the VCSEL's on Chip D3G.

The nonlinear behavior of the lasers is recognized from Figure 11. To test that this behavior was repeatable, the P-I curve of V8 was measured again with a slightly different setup. The driving current was adjusted from $3\,mA$ to $9.1\,mA$, the corresponding output power was measured, and then the measuring procedure was repeated. These two groups of data are plotted with the original one in Figure 13. They matched each other within experimental error. That implies that the data shows the real behavior of the laser. Yet, though the P-I curves are non-linear well above threshold, Figure 14 shows that in the range of $0-100\mu W$ the lasers were quite linear.

The polarizations of some VCSEL's on Chip D3G were also characterized. The setup for making this measurement is shown in Figure 15. A $50\,mm$ lens was used to collimate the laser beam. A cubic polarizer was mounted on a rotating wheel that has angle marks. A NewPort power meter was used to measure the optical power. Chip D3G,

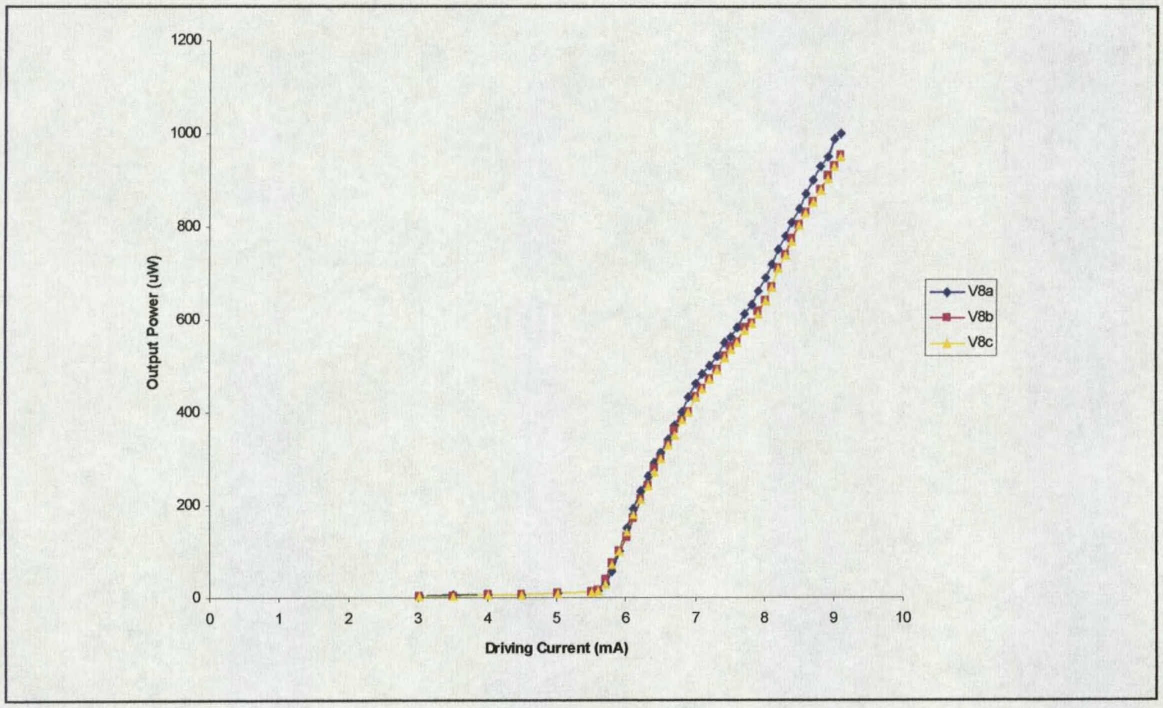

Figure 13. P-I curves for V8 on Chip D3G.

the lens, the rotating wheel and the power meter were mounted on the optics table. The wheel was rotated and the maximum and minimum transmission power and the angles were measured accordingly. The data in Table 3 show that the beam of the VCSEL's on Chip D3G are well polarized ($\frac{P_{max} - P_{min}}{P_{max} + P_{min}} = 0.81 \sim 0.94$) except V9 ($\frac{P_{max} - P_{min}}{P_{max} + P_{min}} = 0.32$). The polarization axes are approximately the same, but which axis is maximum and which axis is minimum are random. All the angles were measured relative to the same 0° reference. The fact that the polarizations are not all aligned is why we could not us polarization based image shifting and instead confined ourselves to using the BPG to split the beams.

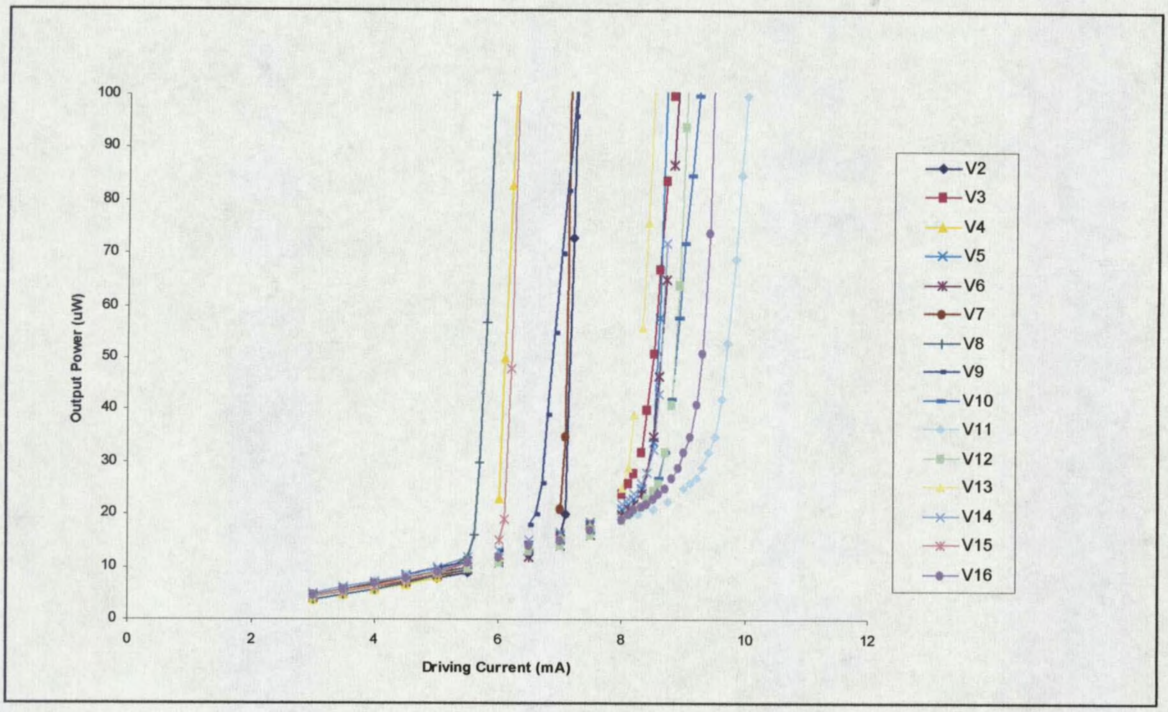

Figure 14. P-I curves of the VCSEL's on Chip D3G in $0-100\mu W$ range.

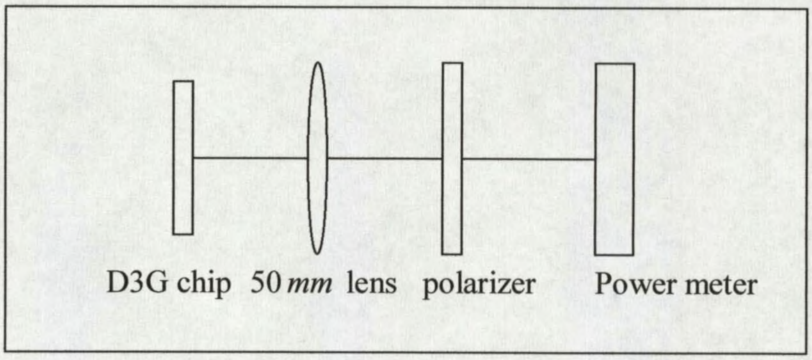

Figure 15. Setup for characterizing the polarization of VCSEL's on Chip D3G.

VCSEL	$\frac{P_{max} - P_{min}}{P_{max} + P_{min}}$	P_{max} _ *axis*	P_{min} _ *axis*
2	0.93	30°	117°
3	0.81	119°	14°
5	0.94	112°	17°
9	0.32	148°	38°
13	0.84	27°	112°

Table 3. Polarization characteristics of VCSEL's on Chip D3G.

A beam profiler was used to measure the waist radius of the VCSEL's beam. The laser beam of the VCSEL is a Gaussian beam. The beam profiler has a CCD camera that can record the laser light. Then its embedded software calculates the beam radius of the beam at the camera position. The CCD camera was put as far away from the OE chip as possible when the measurement was made. The beam radius calculated by the beam profiler has ±5% fluctuation. To average out the fluctuation, when the waist radius was measured, 50 readings were taken and their average was calculated as the final result. Then Mathematica was used to solve Equation (23)[27] to get the waist radius w_0. In Equation (23), z is the distance between the CCD camera and the OE chip, $w(z)$ is the beam radius at the CCD camera position, w_0 is the waist radius of the laser beam, $\lambda = 850nm$ is the wavelength of the laser. With ±5% fluctuation in $w(z)$, w_0 can be calculated within ±7%. w_0 was measured to be $1.38\mu m$ for the VCSEL used in the experiment.

$$w_0\sqrt{1+\frac{\lambda^2 z^2}{\pi^2 w_0^{\,4}}} = w(z) \tag{23}$$

When the P-I curve of the VCSEL's on Chip E3F was measured, a 50 *mm* lens was used to focus the VCSEL beam on the power meter. Though the laser beam expands very quickly, the lens can collect all the laser light. All 16 VCSEL's on this chip are connected. Current higher than 10 *mA* was used to drive the VCSEL's on Chip E3F to find out at what current the output power was saturated. Figure 16 is the P-I curve of the VCSEL's on Chip E3F.

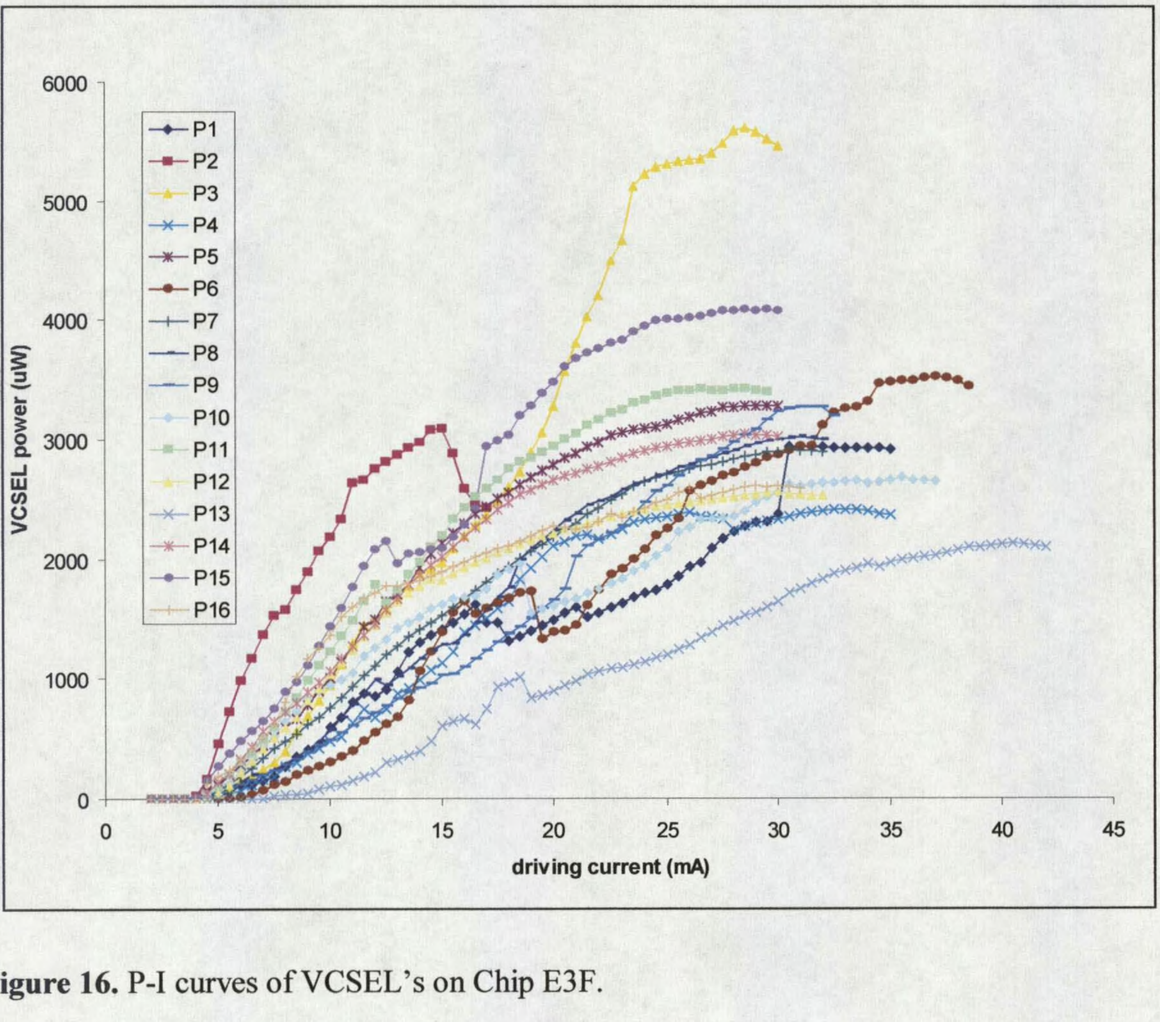

Figure 16. P-I curves of VCSEL's on Chip E3F.

The output power of most VCSEL's on Chip E3F saturated at about $30\,mA$. Some of the P-I curves are smooth, but some of them have "kinks". "Kinks" means that the curve is generally smooth but sometimes there is an abrupt increase or decrease over a very small range. The exact origin of kinks is not fully understood but they are sometimes seen on ion-implanted VCSEL's. We noticed some connection between the "kinks" and spatial mode shifts, but this was not well characterized. Since Chip E3F and Chip D3G are identical, the physical positions of their VCSEL's and MSM detectors are the same as depicted in Figure 10. Figure 17 shows the spatial distribution of the threshold and output power of the VCSEL's on Chip E3F at $10\,mA$. Compared to Chip D3G, VCSEL's on Chip E3F have more uniformity and lower thresholds. Most of the VCSEL's on Chip E3F have threshold of about $5\,mA$ except VCSEL 13 (V13) that has a threshold of $7.5\,mA$. V13 also has a lower Power-Current ratio than other VCSEL's. The VCSEL's on Chip E3F had higher output power at $10\,mA$ than those on Chip D3G.

Threshold (mA)

5.0	4.0	5.0	5.0
4.5	6.0	4.5	4.5
4.5	5.0	4.5	5.0
7.5	4.5	4.5	4.5

Output power (μW) at $10\,mA$

593	2185	949	483
1009	303	755	575
495	948	1227	1035
100	1064	1432	1363

Figure 17. Threshold and output power distribution of VCSEL's on Chip E3F.

VCSEL 14 (V14) on Chip E3F was chosen to be used for the SPSI demonstration in this thesis because it has very smooth P-I curve and a good position on the chip. Good position means the VCSEL and two MSM detectors are in a line parallel to the diagonal line of the OE chip, with the VCSEL in between the detectors. For example, D10 V14 D13 constitutes such an alignment (see Figure 10). A VCSEL and two detectors at such position can constitute a single SPSI pixel. Figure 18 is the P-I curve for V14 on Chip E3F.

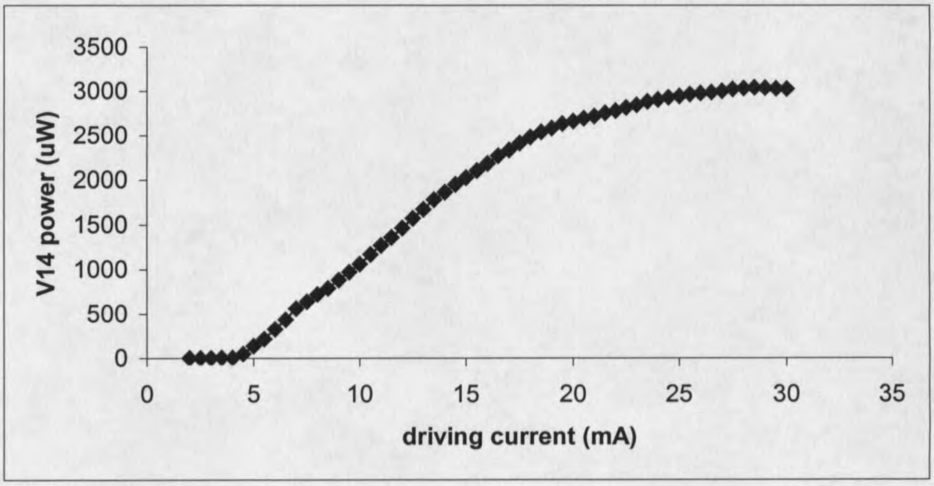

Figure 18. P-I curve of VCSEL 14 on Chip E3F.

The beam profiler was used to observe the spatial intensity profile of the VCSEL beam. Figure 19-Figure 23 are the spatial intensity plots of the V14 output beam at different driving currents. They were recorded by the beam profiler. The profile plots are also included in Figure 19. In the intensity plots, brighter color means higher intensity. When driven at $6\,mA$, the V14 beam is Gaussian. Figure 20 and Figure 21 show that when driven by higher currents, V14 emits in spatial multimode. Figure 22 and Figure 23 show the beam shape when the microlens was used to focus the beam. The spatial multimode behavior can be seen more clearly in these plots. It also can be seen from Figure 23 that when V14 was driven at $6\,mA$, the output beam had a shape closer to Gaussian shape. Similar phenomena were found in other 15 VCSEL's on Chip E3F. All VCSEL's of the type used in this thesis, and especially with greater than 3 μm aperture, radiate in spatial multimode. Reducing the driving current creates a more Gaussian profile but this is not truly TEM_{00} modes. There are always some higher order spatial modes that appear as current is increased. The optical design and tolerance calculation of the single SPSI pixel are based on Gaussian beam propagation and ray tracing theory, so the spatial multimode phenomenon might cause problem to the system. That is because a beam of higher order mode might be focused to a different position other than that of the detector or at least clipped by aperture in the system that otherwise pass the TEM_{00} design mode. But the experiment turned out to be successful in spite of the spatial multimode phenomenon.

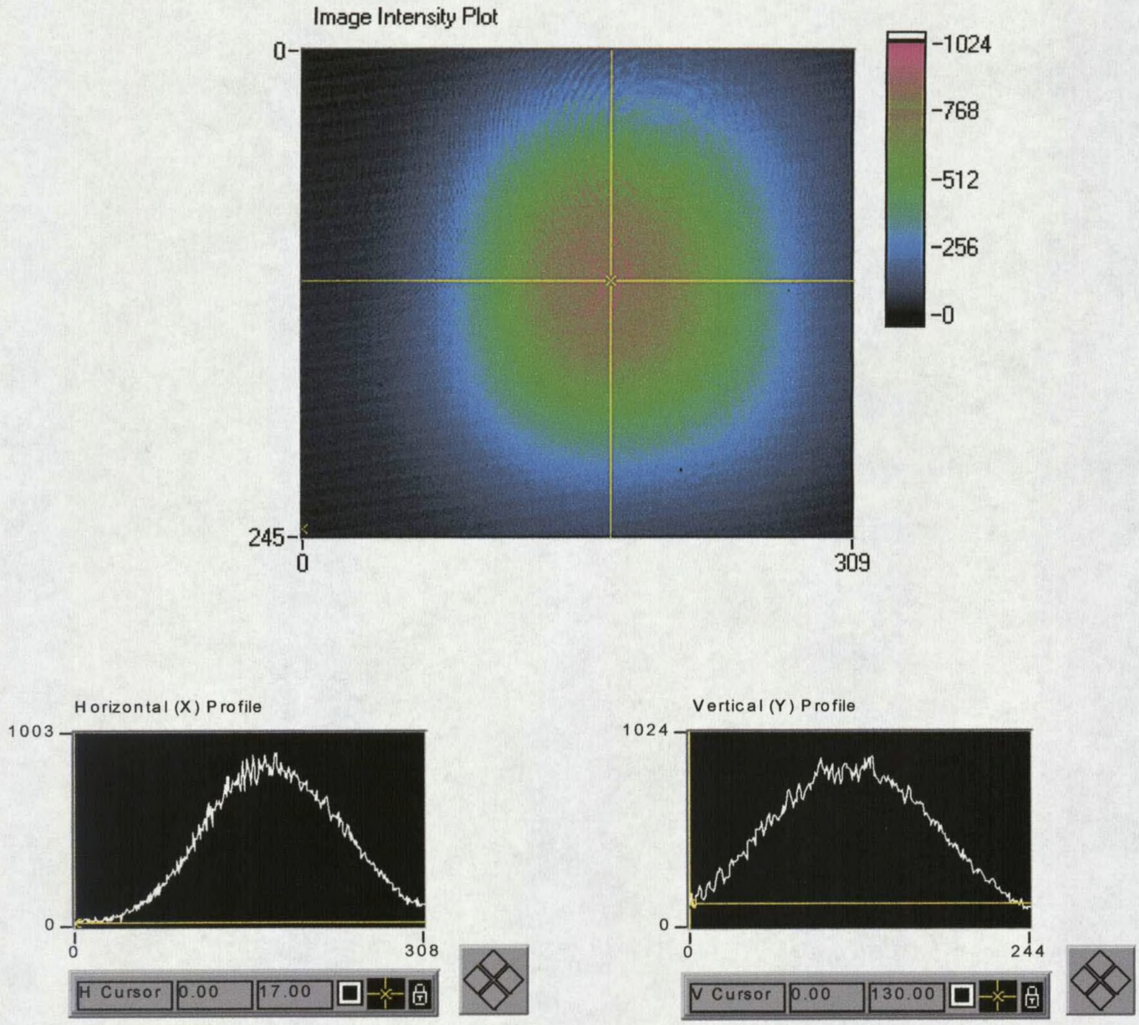

Figure 19. Spatial intensity and profile plots of V14 beam. V14 is driven at $6\,mA$.

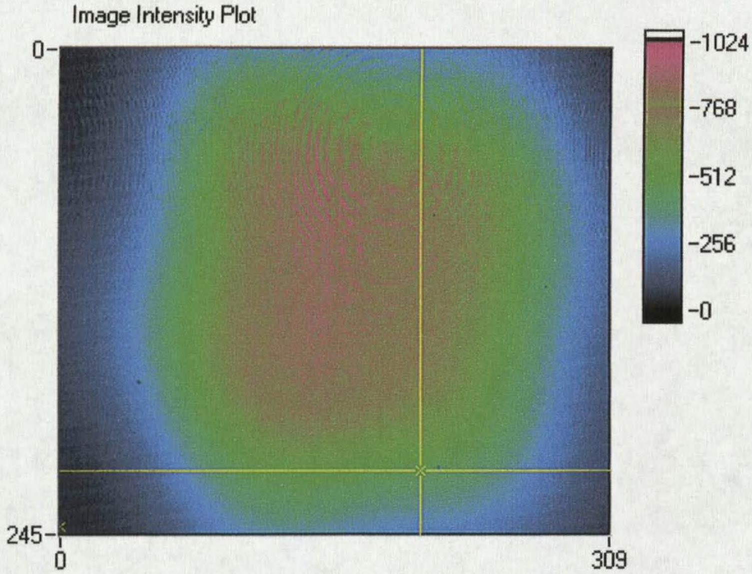

Figure 20. Spatial intensity plot of V14 beam. V14 is driven at $10\,mA$.

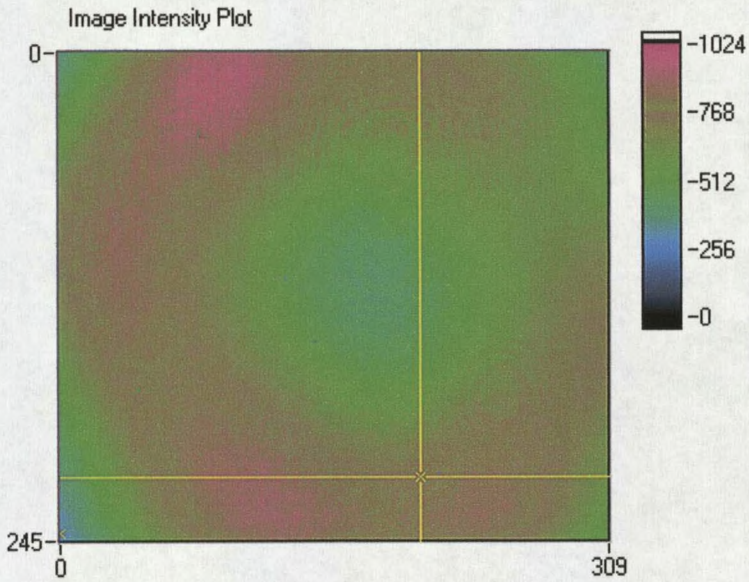

Figure 21. Spatial intensity plot of V14 beam. V14 is driven at $20\,mA$.

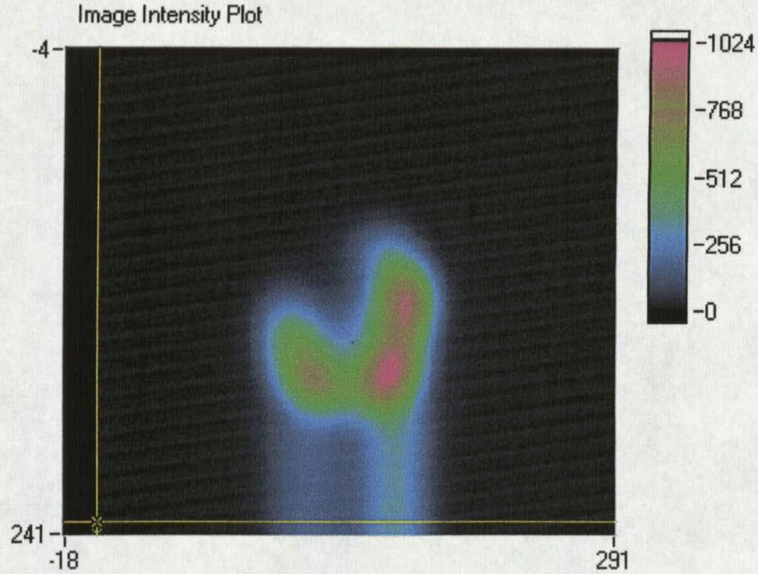

Figure 22. Spatial intensity plot of V14 beam focused by a microlens. V14 is driven at $10\,mA$. The straight trace on the bottom of the image is due to saturation of the CCD camera.

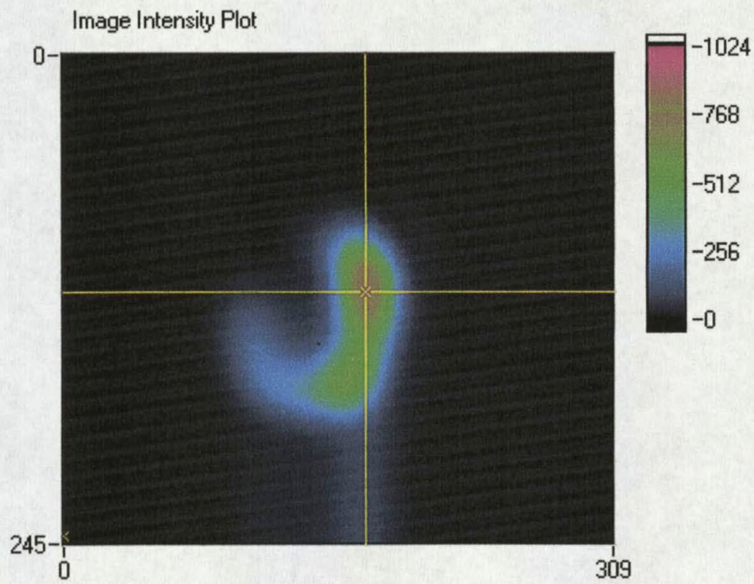

Figure 23. Spatial intensity plot of V14 beam focused by a microlens. V14 is driven at $6\,mA$.

MSM Performance

The MSM detector is like a back-to-back diode. To measure the photocurrent, the device needs to be biased with 2 to 5 volts. In the actual measurement for both chips, the device was biased with 5 volts with circuit shown in Figure 24. The voltage drop on the resistor was measured to calculate the photocurrent.

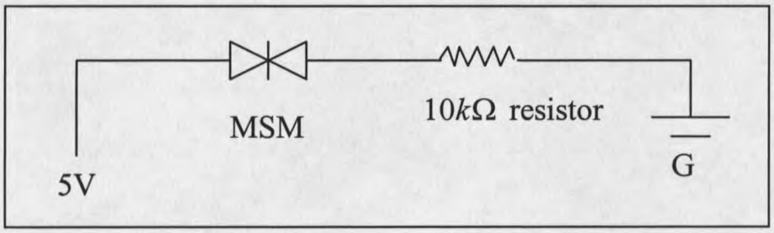

Figure 24. MSM biased with 5 volts.

The setup for measuring the photocurrent of the MSM detectors on Chip D3G is depicted in Figure 25. A VCSEL on the same chip was used as the light source for the detectors when their responsivities were measured. The 50 *mm* lens was used to collimate the laser beam, and the mirror was used to reflect the beam back to the detector. The reflected beam passing through the 50 *mm* lens was focused to a small spot. Even though the mirror could be adjusted to change the direction of the reflected beam, it was extremely difficult to steer the beam to hit the detector without seeing the detector. So a CCD camera was used to monitor the chip. Since the size of the VCSELs and MSM detectors is very small, a lens was needed to blow up the image of the working area of the chip in first place. Then, it was seen that when the reflected beam shined on the detector, the detector became very bright. Some fine adjustment of the mirror was done to get a maximum response from the detector.

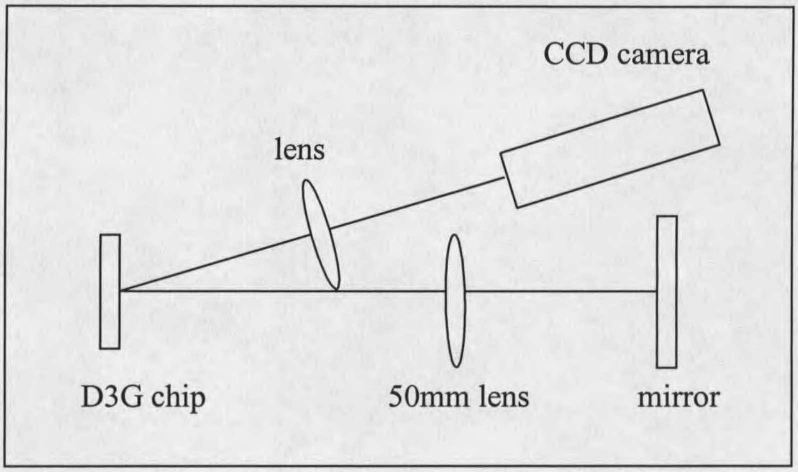

Figure 25. Setup for measuring the photocurrent of MSM detectors on Chip D3G.

Figure 26 is a plot of the output photocurrent of the MSM detectors on Chip D3G as a function of the input power of a VCSEL on the same chip. The laser power values in Figure 26 are the emitting power of the laser instead of the actual power that got on the detector, since the latter one could not be experimentally measured. The power loss on the mirror can be neglected, as the mirror used in this measurement has reflectivity >99% at the wavelength $850\,nm$. Therefore, the power loss was determined by how well the reflected beam would be focused to the detector. This could not be experimentally measured either. But one can see that the actual power on the detector is always equal or lower than the laser emitting power. So, the responsivity got from this measurement may be lower than the actual one. It can be seen from Figure 26 that the responsivity to

850*nm* light of the MSM detector on Chip D3G is pretty linear and all detectors have similar responsivities.

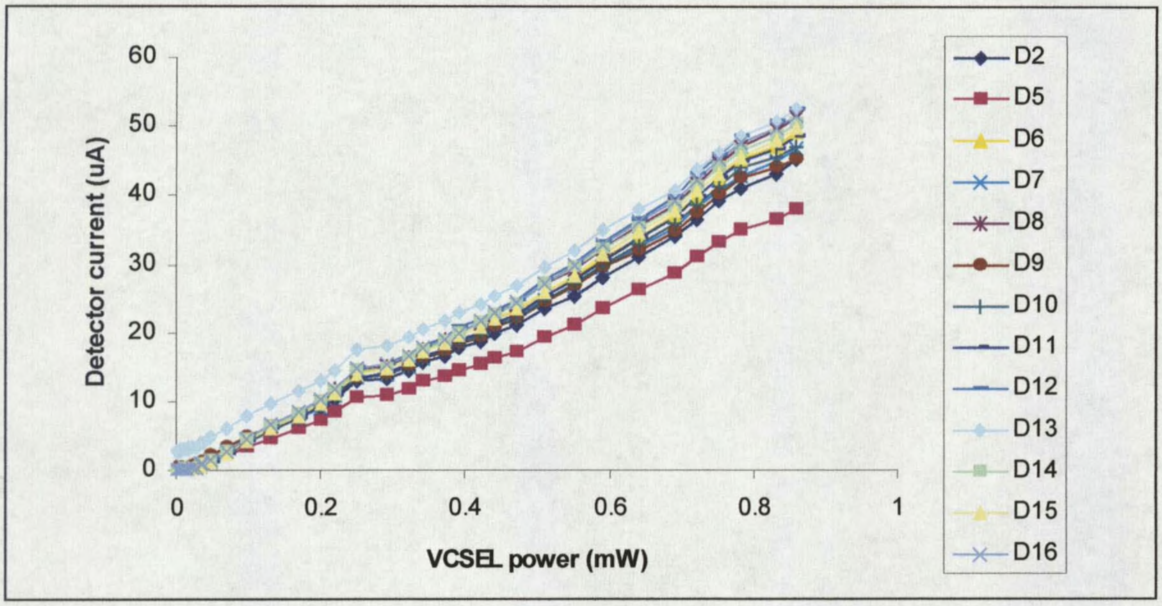

Figure 26. I(photocurrent)-P(power) curves for MSM detectors on Chip D3G.

The setup depicted in Figure 25 is very hard to repeat. An improved setup was used to characterize the responsivity of the MSM detector on Chip E3F. Figure 27 depicts the new setup. A 50 *mm* lens was used to collimate the VCSEL beam. When the collimated beam was reflected by mirror 1 and passed through the 50 *mm* lens again, it was focused to a small spot on the detector. The combination of the 50 *mm* lens and the 150 *mm* lens created an image three times of the size of the original size of the working area of Chip E3F, so the detectors could be seen on the CCD camera. A VCSEL on the same chip with the detectors was used as the light source when the responsivity of the detector was measured. A razor blade was positioned at the image plane of the 150 *mm* lens to block the VCSEL image. So, when that VCSEL was turned on, its light would not flood the detector images. Because the razor blade had to be positioned in the image plane, a 75 *mm* lens was used to create an equal size image on the camera.

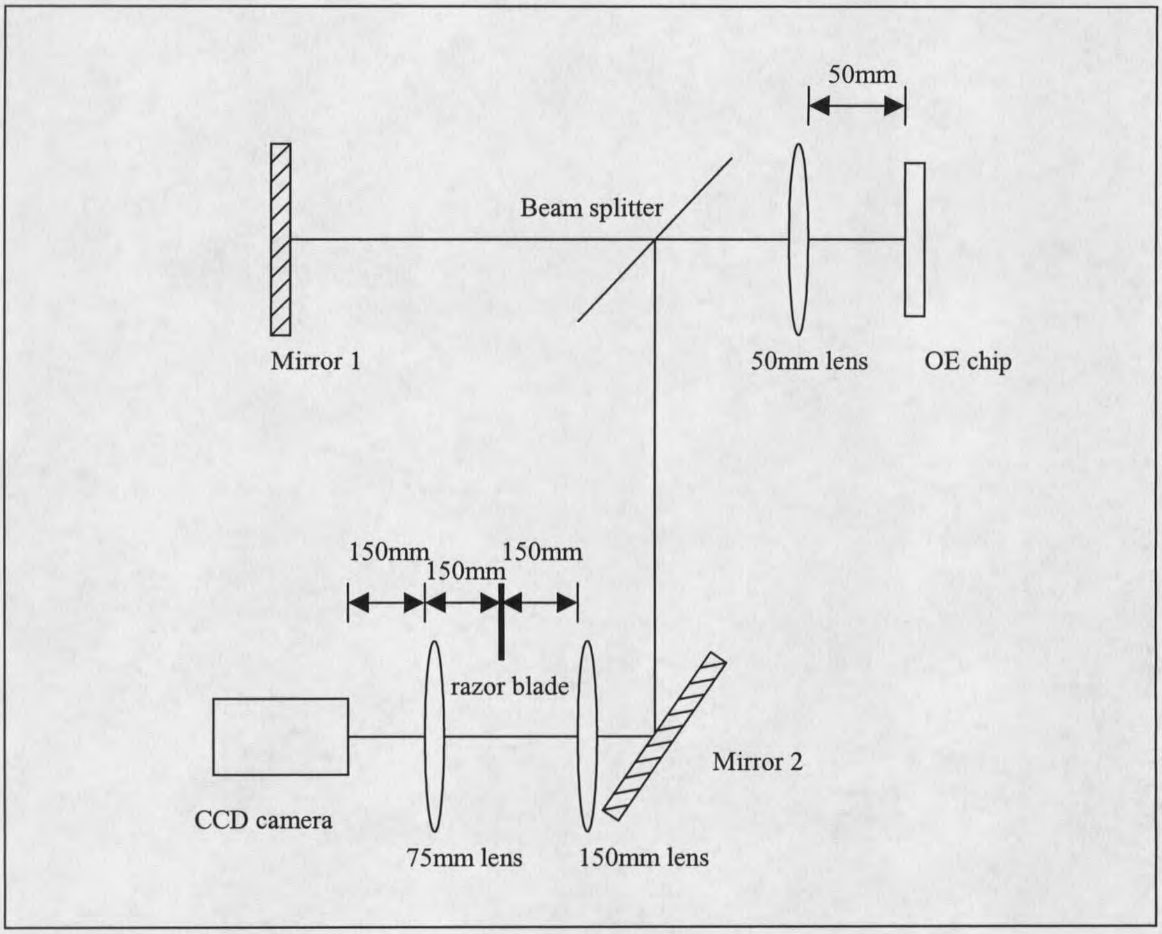

Figure 27. Setup for measuring responsivity of MSM detectors on Chip E3F.

Figure 28 is a plot of the output photocurrent of the MSM detectors on Chip E3F as a function of the input power of a VCSEL on the same chip. The laser power values used in this plot is the laser emitting power times $(60\% * 60\%)$. The power loss on mirror 1 is neglected because of its very high responsivity. 60% is the transmission of the beam

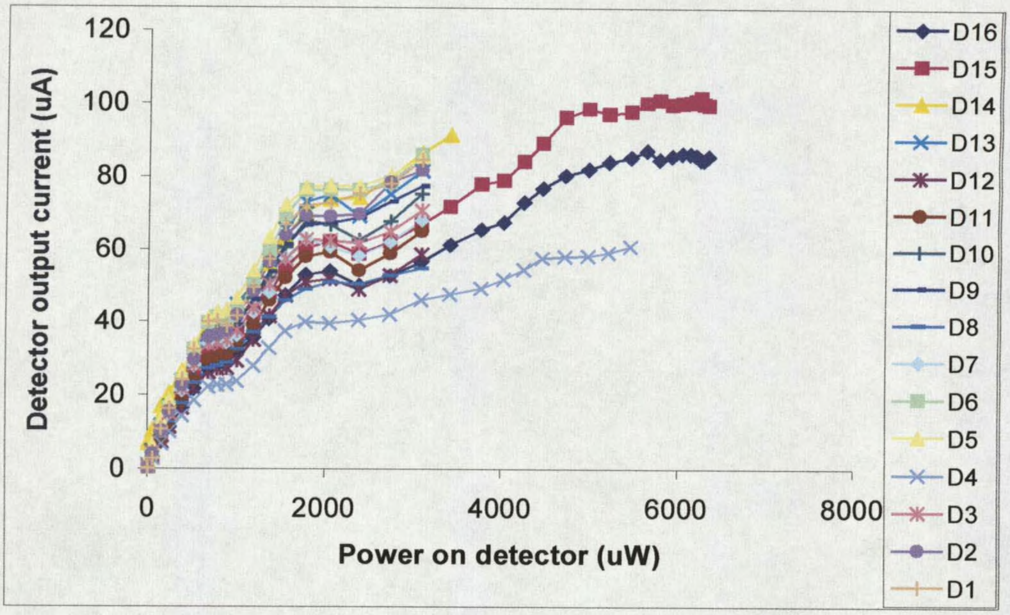

Figure 28. Responsivity of MSM detectors on Chip E3F.

splitter. It is squared because the beam passed through the beam splitter twice. Because of the same reason stated before, the actual light power on the detector might be lower than the one used in the plot, so the measured detector responsivity might be lower than the actual one. The detectors are saturated when photocurrents are about $50\mu A$. That is why when the photocurrents are higher than $50\mu A$, the detectors show nonlinear responsivity. Figure 29 shows the portion of Figure 28 where detector maximum output current is below $50\mu A$. The detector responsivity is mostly linear. But the reason why it has the dip when the input power is around $700\mu W$ to $900\mu W$ is unknown, though we again noticed spatial mode shifts at these dips. Table 4 shows the detector responsivities calculated from the data and the dark current values. Most of the detectors have responsivity about 0.1A/W and dark current about $0.02\mu A$.

Figure 30 is the responsivity plot for Detector 13 (D13) and Detector 10 (D10). They were the ones used in the demonstration of the single SPSI pixel in this thesis.

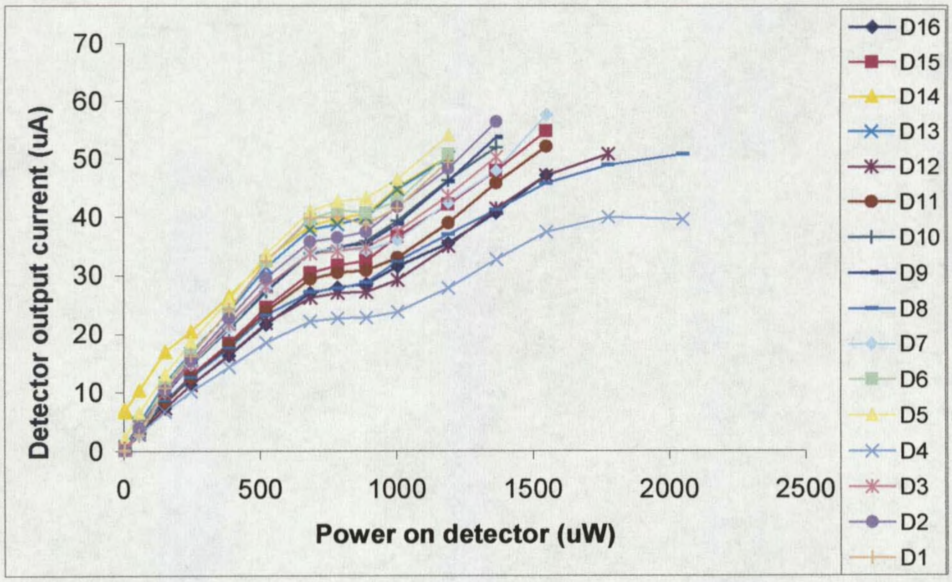

Figure 29. Responsivity (current less than $50\mu A$) of MSM detectors on Chip E3F.

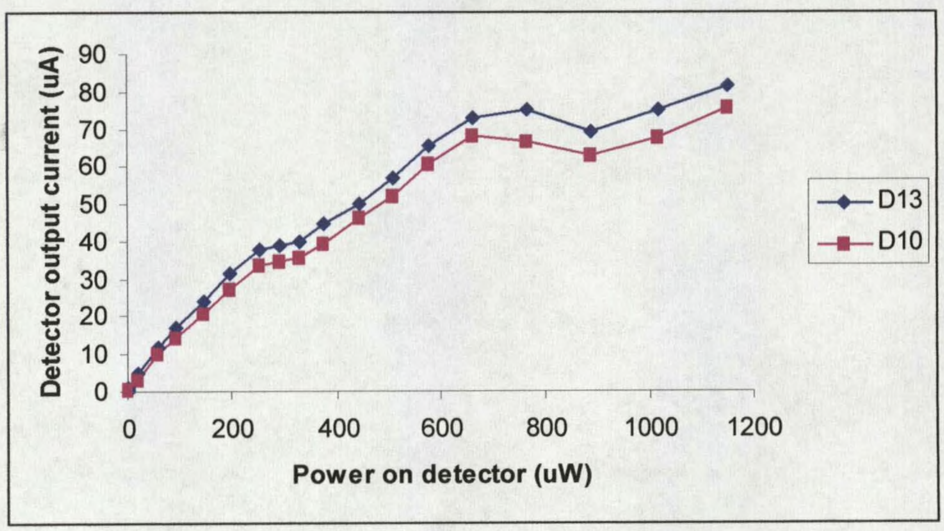

Figure 30. Responsivity of detector13 (D13) and detector 10 (D10) on Chip E3F.

	RESPONSIVITY (A/W)	DARK CURRENT(μA)
DETECTROR1	0.1161	0.01
DETECTROR2	0.1109	0.02
DETECTROR3	0.0995	0.11
DETECTROR4	0.0649	0.02
DETECTROR5	0.1253	1.69
DETECTROR6	0.1207	0.12
DETECTROR7	0.0999	0.02
DETECTROR8	0.0795	0.11
DETECTROR9	0.1064	0.01
DETECTROR10	0.1051	0.01
DETECTROR11	0.0905	0.02
DETECTROR12	0.0818	0.02
DETECTROR13	0.1137	0.1
DETECTROR14	0.1099	6.98
DETECTROR15	0.0951	0.02
DETECTROR16	0.0819	0.02

Table 4. Responsivity and dark current of MSM detectors on Chip E3F.

Summary

The data for the VCSEL's and MSM detectors on both OE chips show that they have quite linear characteristics. The VCSEL's on Chip E3F have more uniformity than those on Chip D3G. The power-current ratio of most of the VCSEL's on Chip E3F at $10\,mA$ is higher than that of the VCSEL's on Chip D3G. The MSM detectors on Chip E3F have higher photocurrent-power responses than those of the MSM detectors on Chip D3G. In a word, Chip E3F has better quality than Chip D3G. V14, D10 and D13 on Chip E3F are picked to form the single SPSI pixel. The multimode phenomenon is observed from the VCSEL's on Chip E3F. How this phenomenon affects the function of the single SPSI pixel needs future study.

CHAPTER 4

EXPERIMENTAL

The experimental setup for a single SPSI pixel to demonstrate normalized differential detection is depicted in Figure 31. Figure 32 is a photograph of the setup. The single SPSI pixel includes an optical part and an electronic part. The optical part splits the laser beam before illuminating a scene and images the illuminated spots onto corresponding detectors. The ND filter in front of each beam attenuates the beam, which is equivalent to using objects with different reflectivities. All of Chapter 4 is done with Chip E3F. The detail of the experimental setup and the alignment procedure for the optical part is given in the first section of this chapter. The electronic part consists of two circuits: one is the current driver and detector bias circuit, the other is the electronic feedback circuit. The first circuit provides current to drive the laser and bias the detectors with $5\,volts$. The drive current is modulated by an external modulation voltage V_{mod} that is provided by the second circuit. V_1' and V_2' are generated by the first circuit and are the inputs of the electronic feedback circuit. An oscilloscope is used to measure its outputs V' and V_{out}. The second section gives the detail of the electronic part. Equation (22) (see end of chapter 2) describes the output of the system (V_{out}) for the ideal situation that no crosstalk exists. However, the experiment showed that different kinds of crosstalk did exist in the system so that a more complicated model than the one described by Equation (22) is developed to describe the system. Section 3 will explain how the new model is developed. V_{out} was experimentally measured and compared to the prediction of the new model. Agreement between the experimental results and the predictions of the model is demonstrated. Based on these results, research on a SPSI edge detector can be carried out in the future.

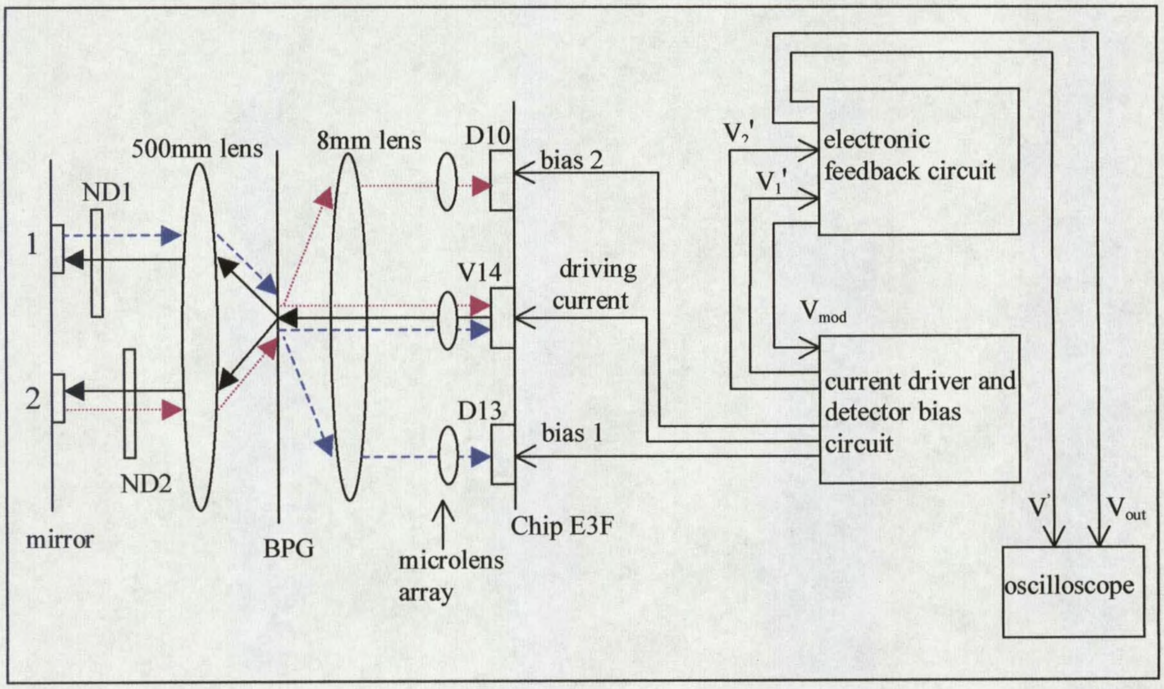

Figure 31. Schematic of the experimental setup for a single SPSI pixel. ND is ND filter. D10 is detector 10, D13 is detector 13 , V14 is VCSEL 14.

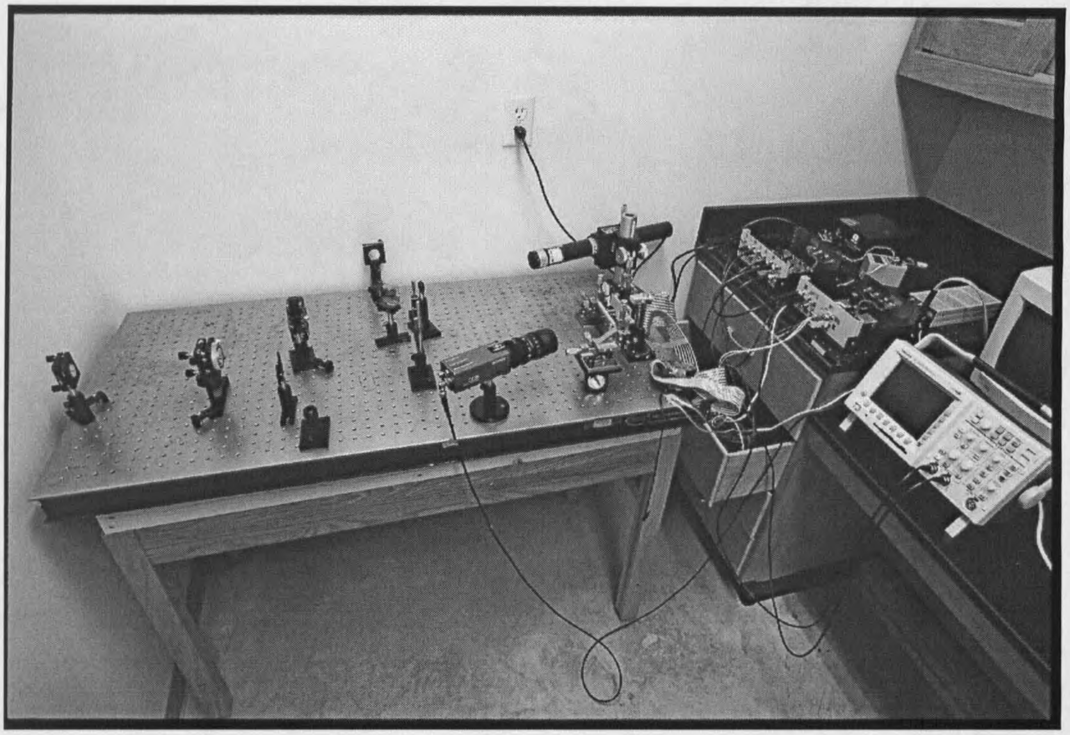

Figure 32. Photograph of the experimental setup for the whole system.

Optical Setup

The schematic of the experimental setup for the optical part of a single SPSI pixel is shown in Figure 33. In this figure, only the central branch of the optics is part of the single SPSI pixel, the HeNe laser, beam splitter, mirror1, mirror2 and CCD camera are used to help with the optical alignment. Figure 34 is a photograph of the setup. It is the optical portion of Figure 32.

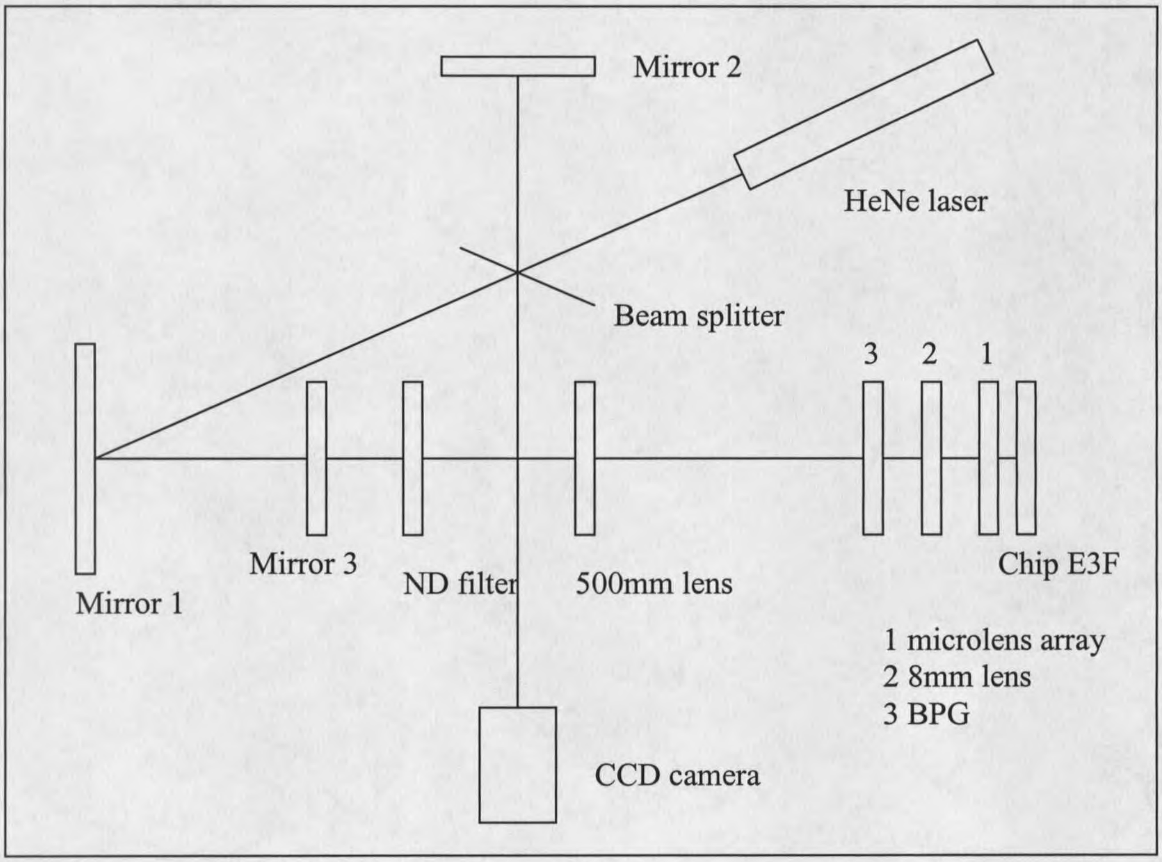

Figure 33. Schematic of the optical part of the experimental setup for a single pixel.

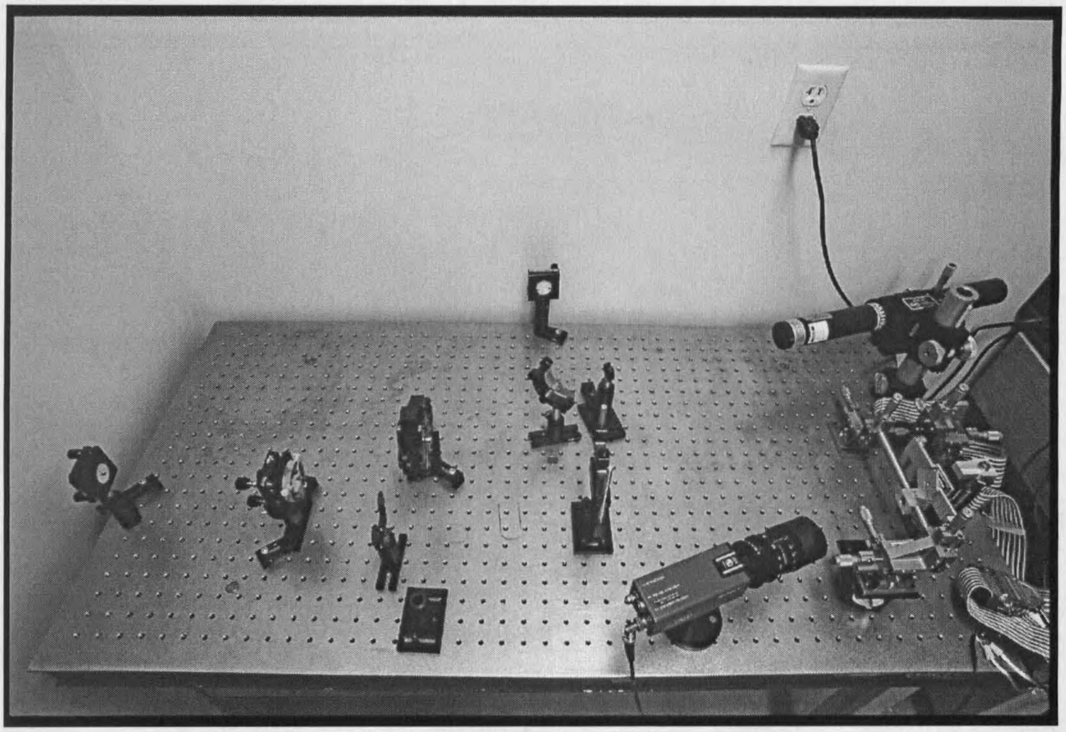

Figure 34. Photograph of the optical part of the experimental setup for a single SPSI pixel.

Figure 35a is a portion of Figure 34. Figure 35b is a portion of Figure 35a. They show more detail of how Chip E3F, the microlens array, 8 *mm* lens and BPG are mounted. It can be seen that they are mounted on home made metal holders. Dr. Kevin Repasky and Norman Williams of Montana State University helped to machine the metal holders. The holders of Chip E3F are mounted on a rotation stage so that Chip E3F surface can be adjusted more easily to be perpendicular to the reference beam in the horizontal direction. The holders of the microlens array, 8 *mm* lens and BPG are mounted on Newport 3-axis stages. Each stage has actuators for x, y and z directions. The SM

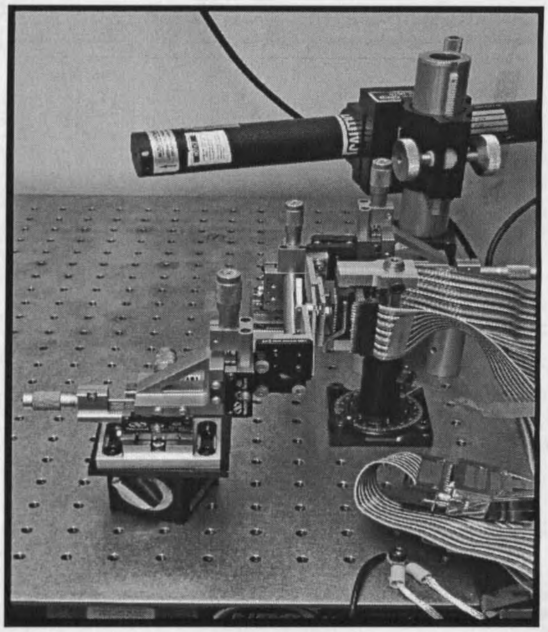

Figure 35a. Photograph of the mounting for Chip E3F, the microlens array, 8mm lens, and BPG. This photograph is a portion of Figure 34.

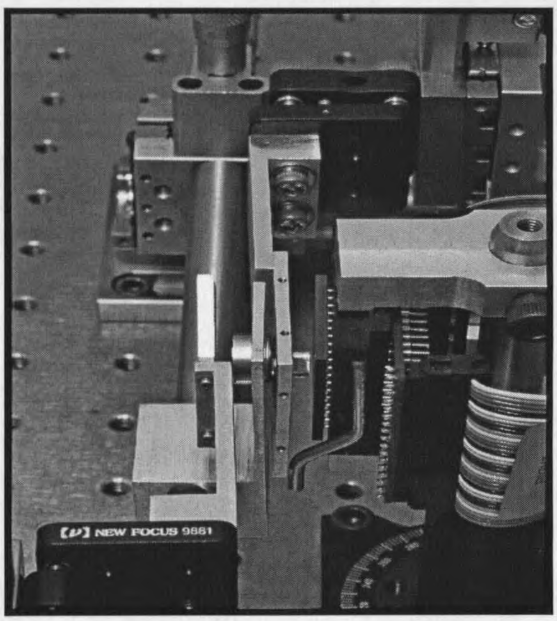

Figure 35b. A detail portion of Figure 35a displaying the home made metal holders for Chip E3F, the microlens, 8 *mm* lens, and BPG

series metric micrometers are used as actuators. They have 50.8 threads per inch and read directly in units of $0.01\,mm$, with vernier reading of $0.001\,mm$. Their travel range is $13\,mm$. With such positioning equipment, the tolerance requirements discussed in Chapter 2 can be met.

The microlens and the BPG were made by Digital Optics Corporation. They both are part of glass plates of $4mm \times 4mm$ size. On each microlens plate, there are four groups of 8×8 microlens arrays. They are depicted in Figure 36. All microlenses have a $176.8\mu m \times 176.8\mu m$ aperture. Each group of lenses has different focal length and coupling efficiency[28]. The lenses in group A have 407 μm focal length, an F-number[29] of 2.3, 4 phase levels and 68% coupling efficiency. The lenses in group B have 500 μm focal length, an F-number of 2.8, 4 phase levels and 57% coupling efficiency. The lenses of group C have 672 μm focal length, an F-number of 3.8, 4 phase levels and 40% coupling efficiency. The lenses in Group D has 831 μm focal length, an F-number of 4.7, 8 phase levels and 34% coupling efficiency. Group C is used in this thesis because when we designed the optical part of the single SPSI pixel that was the only microlens array information we got from the designer of the microlens arrays. We did not know there are other options of microlens arrays.

The microlens array and the BPG have a special requirement on how to mount them. The microlens plate needs to be mounted at 45° relative to the vertical direction to map the microlenses positions to the VCSEL's and MSM detectors positions. The combination of one VCSEL and two MSM detectors makes up the emitter and detectors of a single SPSI pixel. As stated before, the VCSEL is between the two MSM detectors, and they are in a line parallel to the diagonal line of the working area of the chip. This can be seen in the combination of [D10, V14, D13] in Figure 10. For this reason, the BPG also needs to be mounted at 45° relative to the vertical direction.

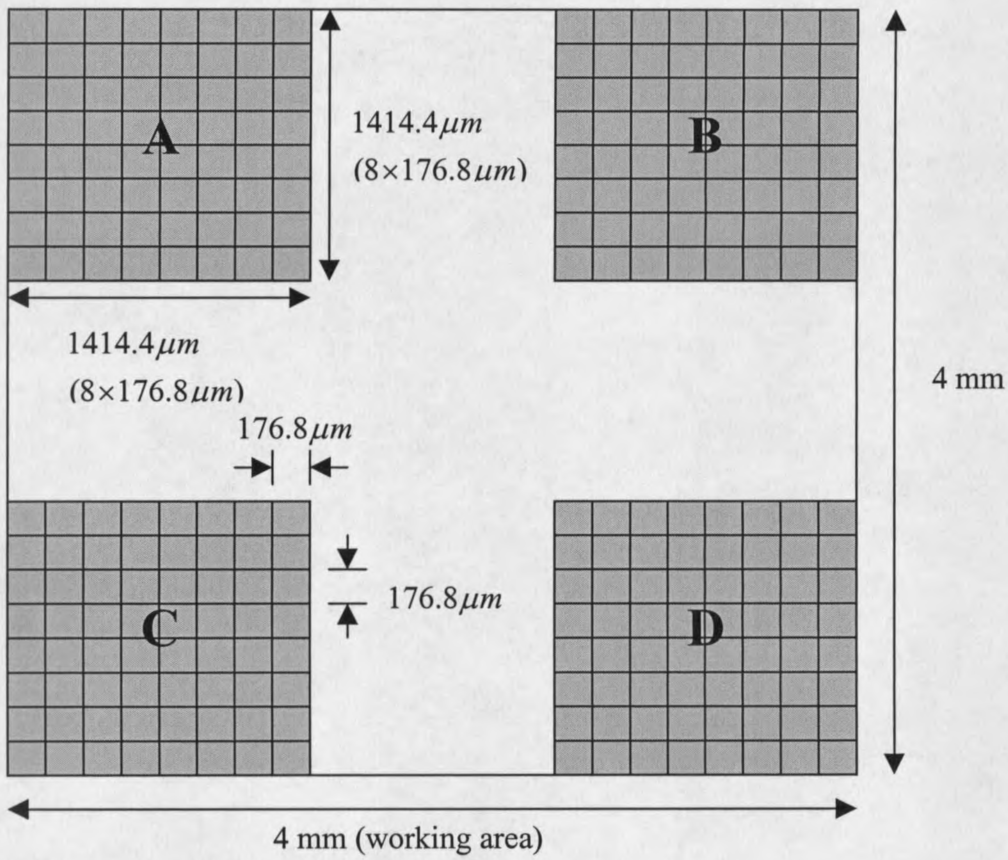

Figure 36. Microlens array plate.

Due to the very small size of the optical devices, it is a challenge to align them. A green HeNe beam was used as a reference beam to help with the alignment. The detail of the alignment procedure is given below.

The Chip E3F was mounted at the very end of the optics table. The chip was adjusted so that its surface was as parallel to the table as possible judging by eyes. The

HeNe laser was mounted at the position depicted in Figure 33. Mirror 1 was used to reflect the HeNe beam to the OE chip. The positions of the HeNe laser and of mirror1 were adjusted until the reflected HeNe beam was parallel to the optics table and was incident on the working area of the OE chip. Then, this beam was acting as the reference of the optical axis for the single SPSI pixel. A beam splitter was put in front of the HeNe laser. Its surface was positioned about $45°$ to the outgoing beam. Mirror 1 was blocked by a beam block. Mirror 2 was put at the position as depicted in Figure 32. Mirror 2 was adjusted to make the reflected beam overlap the outgoing beam. A CCD camera was positioned as shown in Figure 32. On the monitor of the camera, the HeNe beam was seen as a round spot. That spot shape was marked on the monitor. Then, the positions of the HeNe laser, mirror1, mirror 2 and beam splitter were not changed. The camera could be moved, but the mark of the laser beam on the monitor would need to be changed accordingly.

Now the beam block in front of mirror 1 was moved to block mirror 2. The reflection of the chip could be seen but it did not overlap the mark on the monitor. This means that the surface of the chip was not perpendicular to the reference beam. The chip's vertical position can be adjusted by tilting the chip between the two holders. It is relatively more difficult to get to the right position by this way. So, the vertical direction was adjusted first. Then the rotation stage was rotated to adjust the chip's horizontal position. These two adjustments were iterated until the reflection of the chip overlapped the mark on the monitor as well as possible. Then it could be said that the surface of the chip was perpendicular to the reference beam.

The reflection of the chip was a round spot with diameter of about $4mm$. The distance between the surface of the chip and the camera was $1725mm$. The reflection of the chip overlapped the mark within 20% vertically and within 10% horizontally. So the error of using this method to align the chip could be calculated as following:

$$\text{Horizontal: } 4\times 10\%/1725 = 2.3\times 10^{-4}\, radians \quad (24)$$

$$\text{Vertical: } 4\times 20\%/1725 = 4.6\times 10^{-4}\, radians \quad (25)$$

It was assumed the VCSEL output light would be emitted perpendicular to Chip E3F surface. To check this, an IR card was put in front of Chip E3F and both a VCSEL and the HeNe laser were turned on. It could be seen that the HeNe beam was centered in the VCSEL beam. That means the VCSEL emitted light is perpendicular to Chip E3F surface.

The same method was used to adjust the microlens plate perpendicular to the reference beam. The holder of the microlens plate was mounted on a New Focus pint-size mount so there was the option to adjust the plate's horizontal tilt position finely. But, in order to adjust its vertical tilt position, the holder needed to be adjusted by hand. Still, the result was very good. The reflection of the microlens plate had a diamond shape with a diagonal of about $5mm$. It overlapped the mark on the monitor within 10% horizontally and within 30% vertically. The distance between the plate and the camera was $1725mm$. So the error of the alignment was:

$$\text{Horizontal: } 5\times 10\%/1725 = 2.9\times 10^{-4}\, radians \quad (26)$$

$$\text{Vertical: } 5\times 30\%/1725 = 8.7\times 10^{-4}\, radians \quad (27)$$

After the microlens plate was adjusted perpendicular to the reference beam, the IR card was held in front of the microlens and the translation stage x-axis and y-axis actuators were adjusted until the VCSEL light passing through the microlens overlapped the HeNe beam. Then, the z-axis actuator was adjusted to position the microlens at the designed position relative to the chip. This procedure needed to be iterated until both requirements were met.

The beam profiler is used to help to decide if the microlens is at the designed position. The CCD camera of the beam profiler is put in front of the microlens, having the distance between them as big as possible. Since the VCSEL beam has a Gaussian profile only at low current, w_0 is measured when V14 runs at $4.7mA$. And V14 runs at $4.7mA$ all through the alignment procedure of the optics. From Chapter 2, the desired waist radius w_1 of the VCSEL light after it passes through the microlens is known. The beam radius that is expected to get on the camera can be calculated using the following equations[27]:

$$w(z) = w_1\sqrt{1+(\frac{z}{z_1})^2} \qquad (28)$$

$$\text{With } z_1 = \frac{w_1^2\pi}{\lambda},\ z = \ell - l_{11} \qquad (29)$$

Where ℓ is the distance between the camera and the microlens, l_{11} is the distance between the microlens and w_1 (see Figure 5), z is the distance between the camera and w_1, λ is the wavelength of the VCSEL light, $w(z)$ is the beam radius expected on the camera. The actuator on the translation stage is adjusted until the smallest spot can be seen on the profiler. At that position, the microlens is about $672\mu m$ away from the VCSEL. Then, the microlens is moved farther away from Chip E3F until the expected spot size of $2182.3\mu m$ at $z = 90334\mu m$ is reached. The error in z is ±2%, so the error in l_{01} is estimated to be $\pm 1.4\%$.

When the $8mm$ -lens surface was adjusted perpendicular to the reference beam, an interference pattern of the HeNe beam was seen on the monitor. So, instead of comparing the reflection position to the mark on the monitor, the room light was turned off and the reflection of the lens on mirror 1 was used directly. The lens was adjusted until the center of the reflection of the lens overlapped the HeNe beam. Then, the same way of adjusting the microlens was used to adjust the $8mm$ lens to its designed position.

The reflection of the BPG on the monitor was used to adjust the BPG perpendicular to the reference beam. The reflection of the BPG had a diamond shape with a diagonal of about $1.99mm$; and, it could be centered to the mark on the monitor within 20% horizontally and within 10% vertically. The distance between the BPG and the camera was $1675mm$. So the error of the alignment was:

$$\text{Horizontal: } 1.99 \times 20\% / 1675 = 2.38 \times 10^{-4} radians \quad (30)$$

$$\text{Vertical: } 1.99 \times 10\% / 1675 = 1.19 \times 10^{-4} radians \quad (31)$$

Then, the VCSEL was turned on. An IR card was used to show the two spots split by the BPG and the distance between them was measured. The same measurement was done at a different z-position. Then the splitting angle was calculated from these data. If it was not the designed one, the z-position of the BPG was adjusted until the designed splitting angle was obtained. Figure 37-Figure 39 are the spatial intensity plots of the beam split by the BPG. In Figure 37, V14 runs at $4.7mA$. It can be seen that most of the laser power is at the ±1 order of the diffraction and the ±1 order diffraction spots have mostly equal power. The spots are Gaussian. In Figure 38, V14 runs at 7mA. Even though V14 is running spatial multimode at this current, the spots are focused to the center of the microlens. In Figure 39, V14 runs at 15mA. The diamond shapes are the shapes of the microlens. The spots are no longer focused to round spots.

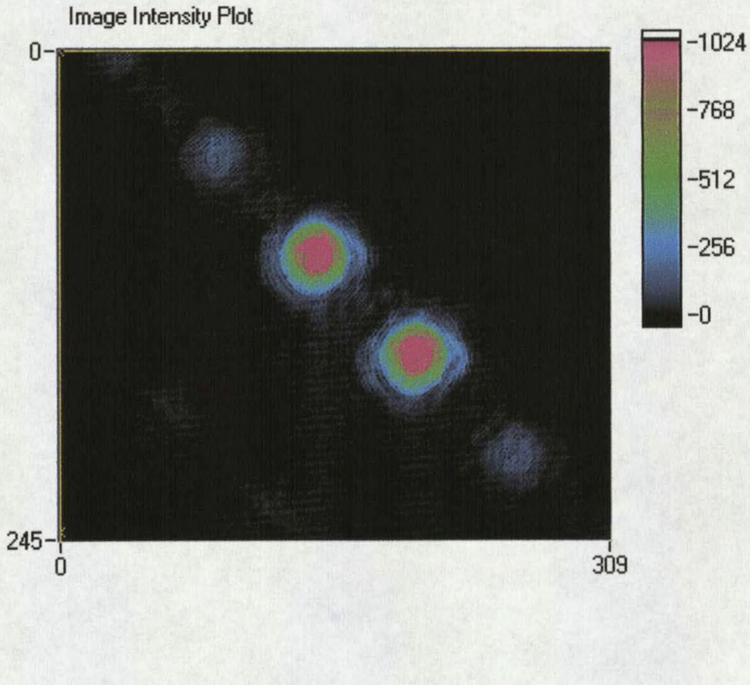

Figure 37. V14 beam split by the BPG. V14 runs at $4.7mA$.

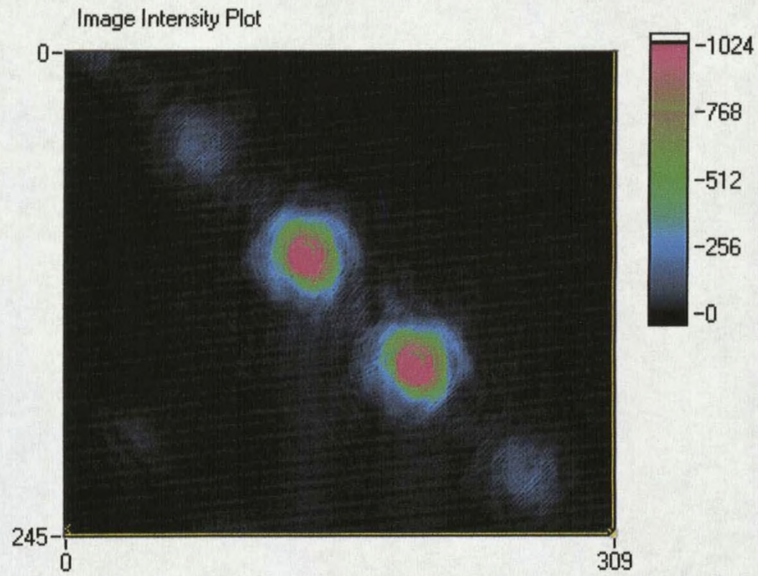

Figure 38. V14 beam split by the BPG. V14 runs at $7mA$.

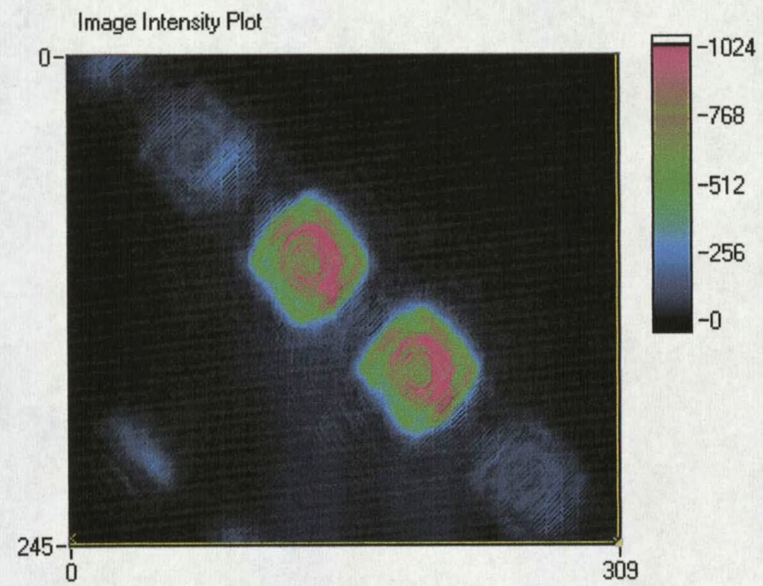

Figure 39. V14 beam split by BPG. V14 runs at $15mA$.

The $500\,mm$ lens was then mounted $500\,mm$ away from the BPG. The reflection on mirror 1 was used to adjust the $500\,mm$ lens perpendicular to the reference beam. Then, mirror 3 was put at the focal point of the $500\,mm$ lens. The CCD camera now was moved to observe the BPG. When mirror 3 was adjusted, the spots could be seen moving on the surface of the BPG holder. Mirror 3 was adjusted until the spots hit the BPG. Then some fine adjustment was done until both of the outputs of the detectors were peaked. If everything were aligned well, both outputs would be peaked at the same time. And that is what happened.

Opto-Electronic Feedback Circuit

Both the current driver and detector bias circuit and the electronic feedback circuit are built on printed circuit boards (PCB's). Steve Kelly and Johnathon Holroyd of Montana State University helped to make the PCB's. These two circuits make up the OE feedback circuit for a single SPSI pixel. Figure 40 is a photograph of the current driver and detector bias circuit. Figure 41 is a photograph of the electronic feedback circuit. They are the electronic portions of Figure 32.

Figure 42 is the block diagram of the OE feedback circuit. The current driver and detector bias circuit has actually two circuits with different functions on the same PCB. The detector bias part biases the MSM detector with $5\,volts$. When light is incident on D13 (D10), this circuit will generate an output voltage V_1' (V_2'). The current driver part provides current to drive V14. A Wavelength Electronics LDD200-2P current driver unit

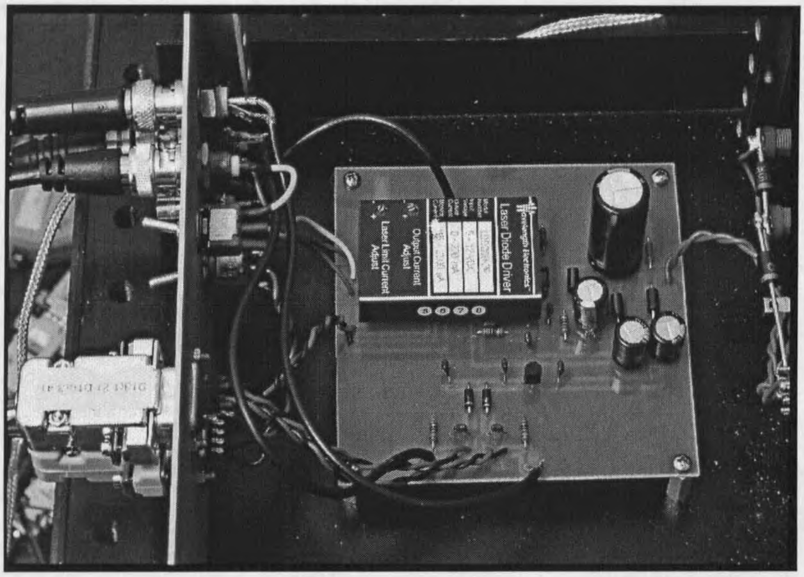

Figure 40. Photograph of the current driver and detector bias circuit.

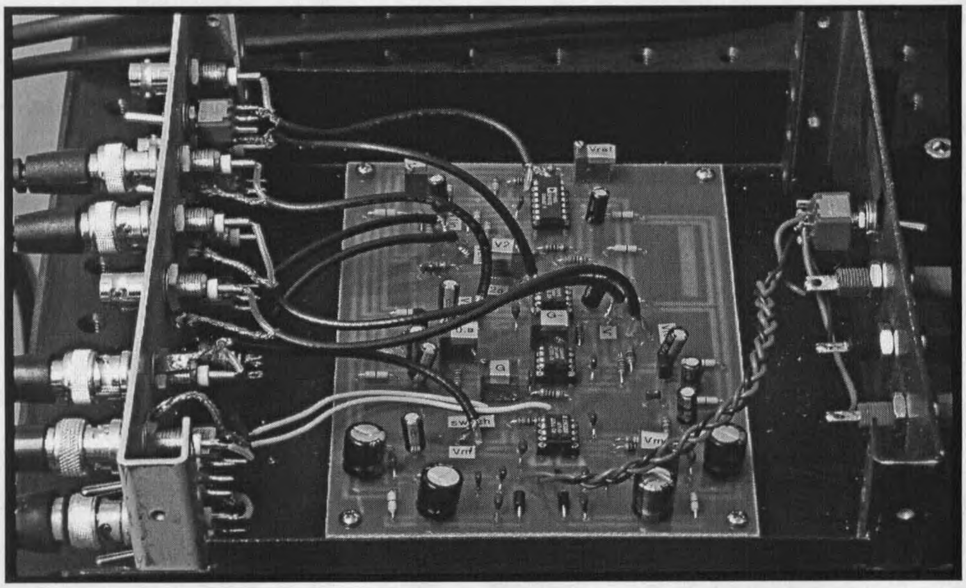

Figure 41. Photograph of the electronic feedback circuit.

is used in the current driver circuit. The current output of LDD200-2P is adjustable, and can be modulated by an external modulation voltage. However, it can not be modulated by a negative voltage. Equation (32) is the current modulation equation[30]. I_{LD} is the actual current through the laser diode, $I_{SETPOINT}$ is the current through the laser diode as set by the output current adjust trimpot, and V_{mod} is the modulation voltage.

$$I_{LD} = I_{SETPOINT} - 33.3mA / Volt \times V_{\text{mod}} \tag{32}$$

It can be seen from this equation that as the modulation voltage increases, I_{LD} will decrease.

On Figure 42 from right to left, the first two subtractors can subtract a dc offset $V_{offset1}$ ($V_{offset2}$) from V_1' (V_2') to produce V_1 (V_2). The second subtractor calculates the difference between V_1 and V_2 as the system output V_{out}. Then, from left to right, the adder calculates the sum (V') of V_1 and V_2. The differential amplifier calculates the difference between V' and V_{ref}, then amplifies the difference by a gain of G. The result of the differential amplifier is given in Equation (33). G can be varied from 2 to 1000 (see appendix). G should not be set too high. Otherwise, the OE feedback loop would oscillate.

$$V_{\text{mod}}' = G \times (V_{ref} - V') \tag{33}$$

The last subtractor produces a modulation voltage V_{mod} to modulate the current driver output current. Since the current driver will not react to a negative modulation voltage[30], a

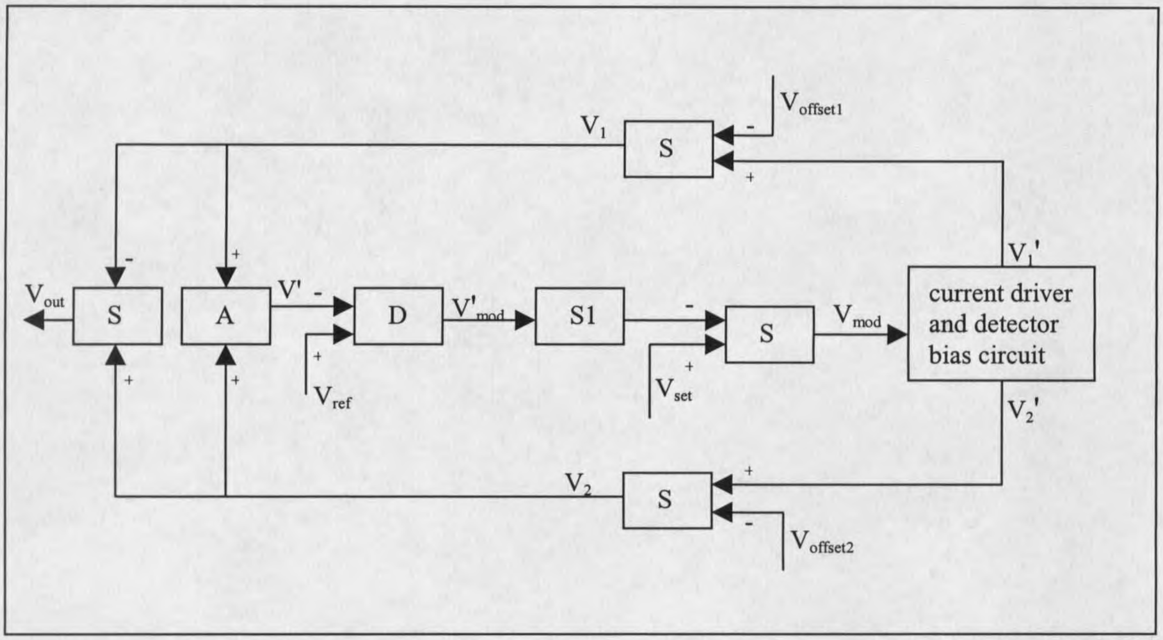

Figure 42. Block diagram of the OE feedback circuit. S is a subtractor. A is an adder. D is a differential amplifier with adjustable gain G. S1 is a switch. The values of $V_{offset1}$, $V_{offset2}$, V_{ref}, and V_{set} are adjustable.

pre-set voltage (V_{set}) is used to offset the driving current first. V_{mod} is described by:

$$V_{mod} = (V_{set} - V_{mod}^{'}) \tag{34}$$

such that $V_{mod} > 0$ always

After this expression of V_{mod} is plugged into Equation (32), I_{LD} is described by:

$$I_{LD} = I_{SETPOINT} - 33.3mA/Volt \times (V_{set} - V_{mod}^{'}) \tag{35}$$

S1 is a switch between the differential amplifier and the last subtractor. If S1 is turned on, the whole OE feedback circuit is connected. If S1 is turned off, the whole OE feedback circuit is not connected.

When S1 is turned on, and V_{ref} and G are set properly, V' will always stay very close to V_{ref}. For example, if for some reason beam 1 is attenuated that it causes V_1 to decrease, then the system will go through the following adjustment procedure automatically and keep V' stable. In the following procedure, the change before the symbol of "$\Rightarrow$" causes the change after it, $\downarrow$ means the value decreases, $\uparrow$ means the value increases:

$$
\begin{array}{ccccccccc}
V_1\downarrow & \Rightarrow & V'\downarrow & \Rightarrow & (V_{ref}-V')\uparrow & \Rightarrow & V_{\text{mod}}'\uparrow & \Rightarrow & (V_{set}-V_{\text{mod}}')\downarrow \\
 & & & & & & & & \Downarrow \\
 & & V'\uparrow & \Leftarrow & V_1\uparrow, V_2\uparrow & \Leftarrow & I_{LD}\uparrow & \Leftarrow &
\end{array}
$$

We see from this diagram that, when V_1 decreases, it causes the sum V' to decrease, which causes $(V_{ref}-V')$ to increase, which causes V_{mod}' to increase, which causes $(V_{set}-V_{\text{mod}}')$ to decrease, which causes I_{LD} to increase so the laser output power increases, which causes both V_1 and V_2 to increase, so V' increases. This is how the system makes V' stable.

Results

Since more side modes will appear as the driving current of the VCSEL increases, it is desirable to use as low current as possible. On the other hand, since the microlens has only 40% coupling efficiency and the BPG will split the original beam into two beams that each has 40% power, and because of other optical losses and due to the fact that the beam will go through the microlens and BPG twice, only about 2% of the original power can reach each detector. A higher driving current is needed in order to have enough power on the detector to produce big enough signals. Due to this trade off, $I_{SETPOINT}$ is set to $15mA$ in Equation (35). V_{set} is set to $60mV$. So, according to Equation (35), $I_{LD} = 13mA$ when S1 is open in the feedback circuit or $V_{\text{mod}}' = 0$. Now, the gain G also needs to satisfy the restriction in Equation (36). Therefore, the current modulation depth of the current driver is –2mA to 2mA.

$$\left|G \times (V_{ref} - V')\right| = \left|V_{\text{mod}}'\right| \leq 60mV \tag{36}$$

It can be seen in Chapter 2 that some objects with variable reflectivity are needed to demonstrate SPSI. A mirror and ND filters are used to mimic the variable reflectivity. ND filters attenuate the light power. Using ND filters of different optical density (OD) values in the different beam path is equivalent to using objects of different reflectivities. For the convenience of changing OD values, a New Focus 5215 ND filter wheel is used. It gives a wide range of optical densities, from 0.08 to 3.0 in 0.1 increments. Due to the relatively low power that can reach the detector, only ODs of 0.08 to 0.54 are used and the actual transmissions (T's) of the VCSEL light are measured. The ND filer wheel can be positioned so that it only attenuates one beam and does not affect the other beam that can be attenuated by a second ND filter. Equation (22) (see end of chapter 2) can be modified as Equation (37) where T_1 and T_2 are the transmissions of the ND filter in front of beam1 and beam2 respectively. They are squared because each beam passes the same ND filter twice.

$$V_{out} = \frac{T_2^2 - T_1^2}{T_2^2 + T_1^2} V_{ref} \tag{37}$$

In the first experiment, only beam 1 is attenuated by the ND filter. The OD value is set to 0.34 and S1 in the feedback circuit is turned off. First, both beams are blocked so no light is reflected back to the detectors. The potentiometers of the first stages of the feedback circuit are adjusted until the output of these stages are zero. In this way, the dc offset of the detectors are subtracted. The beam block is removed. V_{ref} is then set equal V' which is $118mV$. Now, S1 is turned on and the whole feedback loop is connected. The OD value is changed to 0.08. The gain G needs to be adjusted so that V' is as close to V_{ref} as possible without running into an oscillating problem. Then, the OD value is changed from 0.08 to 0.54 in 0.1 increments. V_{out} is measured and compared to the theoretical value calculated from Equation (37). It should be noticed that, here, $T_2 = 1$ in Equation (37) since no attenuation is done to beam2. Figure 43 is the plot for both results.

The experimental data does not match the theoretical data very well. That is because Equation (37) only describes the most ideal situation that there is not any form of crosstalk. In reality, there is crosstalk between laser and detector and crosstalk between the two detectors. These crosstalks are not constants and can not be subtracted by the first stages of the feedback circuit. Equation (37) needs to be modified to take the crosstalk effects into account.

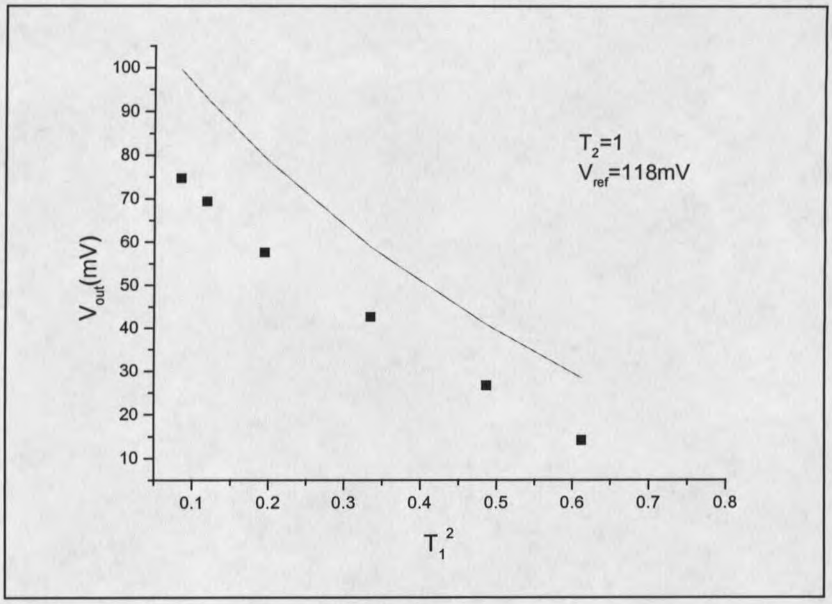

Figure 43. Beam 1 is attenuated by different value of ND filter, the markers are experimental data, the line is theoretical data.

Equation (38) describes the relationship between the laser output L_{out} and the driving current I. β is the coefficient of the current-power transform function. I_{th} is the threshold of the laser.

$$L_{out} = \beta I - \beta I_{th} \tag{38}$$

V_1 and V_2 can be described by the following equations:

$$V_1 = R_1 T_1^2 L_{out} + k_1 I + c_1 R_2 T_2^2 L_{out} + d_{k_1} \tag{39}$$

$$V_2 = R_2 T_2^2 L_{out} + k_2 I + c_2 R_1 T_1^2 L_{out} + d_{k_2} \tag{40}$$

R is the coefficient of the power that can reach the detector. T is the transmission of the ND filter. k is the coefficient of the crosstalk between laser and detector. c is the coefficient of the crosstalk between detectors. d_k is a constant. When Equation (39) and

Equation (40) are combined with Equation (38), they become Equation (41) and Equation (42) respectively.

$$V_1 = (\beta R_1 T_1^2 + \beta k_1 + \beta c_1 R_2 T_2^2)I - R_1 T_1^2 \beta I_{th} - c_1 R_2 T_2^2 \beta I_{th} + d_{k_1} \quad (41)$$

$$V_2 = (\beta R_2 T_2^2 + \beta k_2 + \beta c_2 R_1 T_1^2)I - R_2 T_2^2 \beta I_{th} - c_2 R_1 T_1^2 \beta I_{th} + d_{k_2} \quad (42)$$

If β and R are merged as R, β and k are merged as k, β and c are merged as c, $-R\beta I_{th}$ are merged as d_R, $-cR\beta I_{th}$ are merged as d_c, Equation (41) and Equation (42) can be written as :

$$V_1 = (R_1 T_1^2 + k_1 + c_1 R_2 T_2^2)I + T_1^2 d_{R_1} + T_2^2 d_{c_1} + d_{k_1} \quad (43)$$

$$V_2 = (R_2 T_2^2 + k_2 + c_2 R_1 T_1^2)I + T_2^2 d_{R_2} + T_1^2 d_{c_2} + d_{k_2} \quad (44)$$

To find out the parameters in the above two equations, both T's are set to 1, and the equations are broken into different parts then some data are taken. Then, the data are fit linearly to get the parameters.

First, to find out k and d_k, both beams are blocked that means $R_1 = R_2 = 0$. Equation (43) and Equation (44) become Equation (45) and Equation (46) respectively.

$$V_1 = k_1 I + d_{k_1} \quad (45)$$

$$V_2 = k_2 I + d_{k_2} \quad (46)$$

I is changed from $11mA$ to $15mA$ with $0.5mA$ increments, V_1 and V_2 values are measured accordingly. Figure 44 is the plot of V_1 versus I and the linear fit of the data. The result of the linear fit is $k_1 = 0.54, d_{k_1} = 0.29$. The same method is used to get

$k_2 = 1.03$ and $d_{k_2} = 1.77$. Figure 45 is the plot of V_2 versus I and the linear fit of the data.

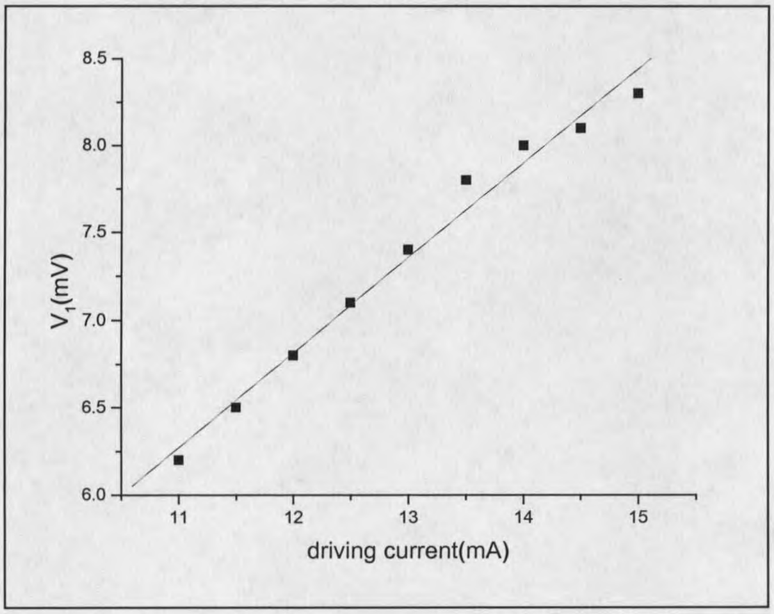

Figure 44. V_1 versus I and the linear fit ($R_1 = R_2 = 0$). The markers are experimental values, the line is the linear fit.

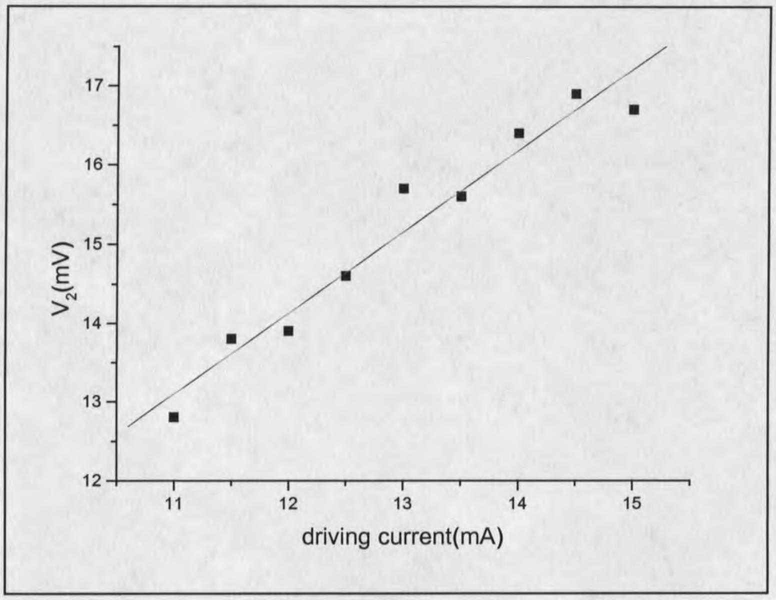

Figure 45. V_2 versus I and the linear fit ($R_1 = R_2 = 0$). The markers are the experimental data, the line is the linear fit.

Second, to find out R_1 and d_{R_1}, beam 2 is blocked that means $R_2 = 0$. Equation (43) becomes Equation (47). Figure 46 is the plot of $V_1 - k_1 I - d_{k_1}$ versus I and the linear fit of the data. The result of the linear fit is $R_1 = 7.18, d_{R_1} = -10.25$.

$$V_1 - k_1 I - d_{k_1} = R_1 I + d_{R_1} \tag{47}$$

Similarly, beam 1 is blocked which means $R_1 = 0$. Equation (44) becomes Equation (48). Figure 47 is the plot of $V_2 - k_2 I - d_{k_2}$ versus I and the linear fit of the data. The result of the linear fit is $R_2 = 10.07, d_{R_2} = -31.39$.

$$V_2 - k_2 I - d_{k_2} = R_2 I + d_{R_2} \tag{48}$$

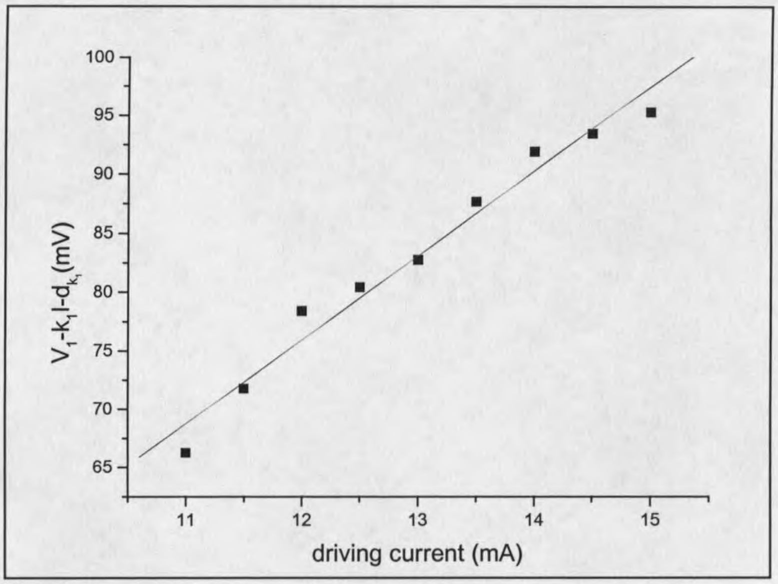

Figure 46. $(V_1 - k_1 I - d_{k_1})$ versus I and the linear fit $(R_2 = 0)$. The markers are experimental data. The line is the linear fit.

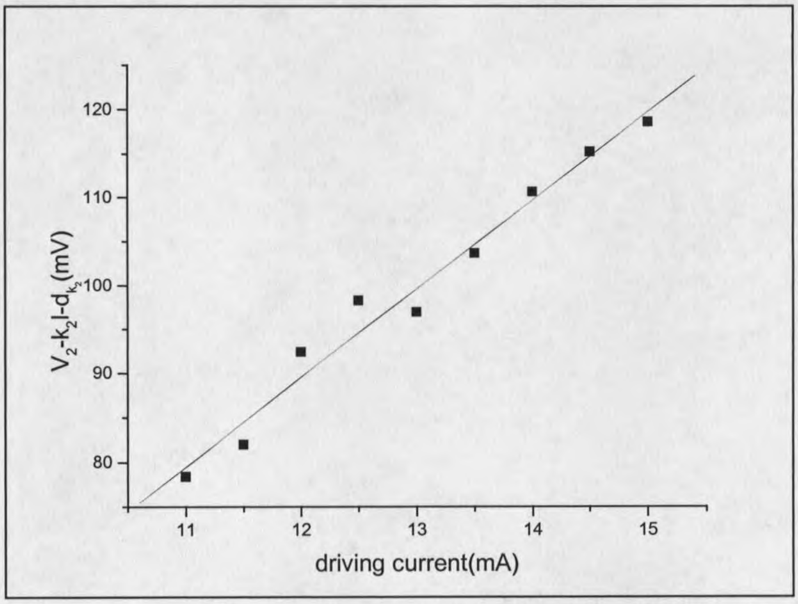

Figure 47. $(V_2 - k_2 I - d_{k_2})$ versus I and the linear fit $(R_1 = 0)$. The markers are experimental data. The line is the linear fit.

Last, to figure out c and d_c, no beam is blocked. Equation (43) and Equation (44) become Equation (49) and Equation (50) respectively. Figure 48 is the plot of $V_1 - k_1 I - d_{k_1}$ versus $R_2 I$ and the linear fit of the data. The result of the linear fit is $c_1 = 0.10, d_{c_1} = -1.83$. Figure 49 is he plot of $V_2 - k_2 I - d_{k_2}$ versus $R_1 I$ and the linear fit of the data. The result of the linear fit is $c_2 = 0.17, d_{c_2} = -2.88$.

$$V_1 - k_1 I - d_{k_1} = c_1 R_2 I + d_{c_1} \quad (49)$$

$$V_2 - k_2 I - d_{k_2} = c_2 R_1 I + d_{c_2} \quad (50)$$

Figure 48. ($V_1 - k_1 I - d_{k_1}$) versus $R_2 I$ and the linear fit. The markers are experimental data. The line is the linear fit.

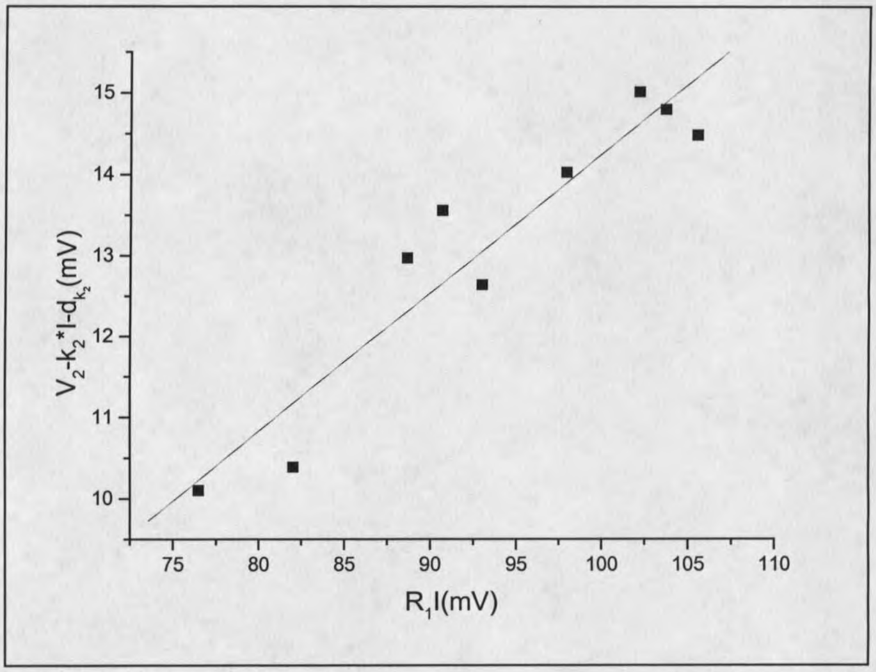

Figure 49. ($V_2 - k_2 I - d_{k_2}$) versus $R_1 I$ and the linear fit. The markers are experimental data. The line is the linear fit.

Now, Equation (43) and Equation (44) can be written as Equation (51) and Equation (52) when T does not equal 1.

$$V_1 = (7.18T_1^2 + 0.54 + 1.05T_2^2)I - 10.25T_1^2 - 1.83T_2^2 + 0.29 \quad (51)$$

$$V_2 = (10.07T_2^2 + 1.03 + 1.23T_1^2)I - 31.39T_2^2 - 2.88T_1^2 + 1.77 \quad (52)$$

Figure 50 is the plot of the experimental data V_1 versus I and of the calculated data V_1 from Equation (51) versus I when $T = 1$. Figure 51 is the plot of the experimental data V_2 versus I and of the calculated data V_2 from Equation (52) versus I when $T = 1$. The graphs show that Equation (51) and Equation (52) can predict V_1 and V_2 well when $T = 1$.

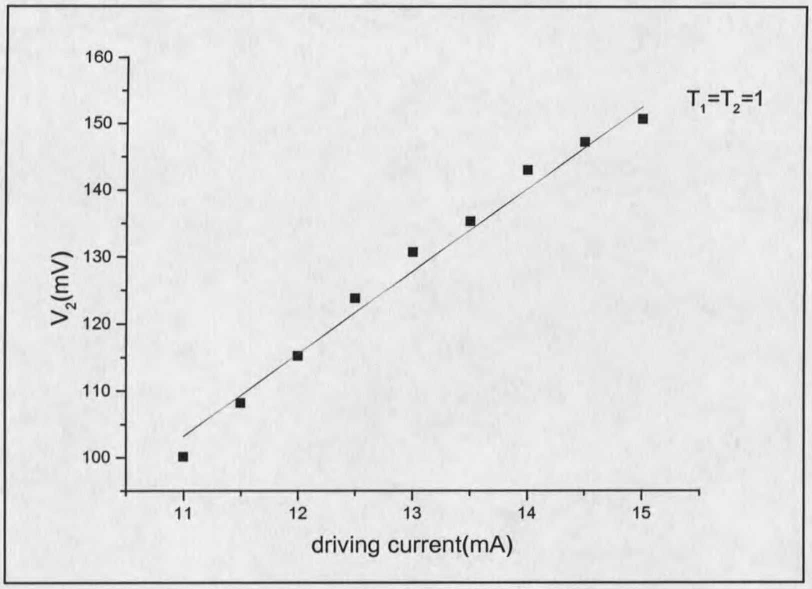

Figure 50. V_1 versus I (the markers are the experimental data, the line is the calculated).

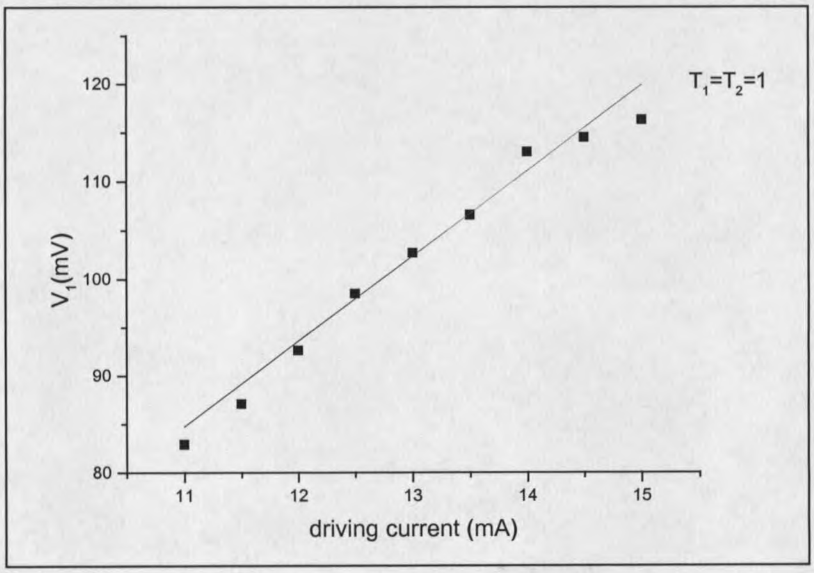

Figure 51. V_2 versus I (The markers are the experimental data, the line is calculated).

Figure 52-Figure 57 are the plots of the experimental data V_1 versus I and of the calculated data V_1 from Equation (51) versus I when $T_1 = 1$ and T_2 equals six different values. Figure 58-Figure 63 are the plots of experimental data V_2 versus I and the calculated data V_2 from Equation (52) versus I when $T_1 = 1$ and T_2 equals six different values. The percentage errors are calculated by :

error%=(experimental value-calculated value)/(calculated value)*100%

(53)

From the plots and the percentage errors, it can be seen that Equation (51) and Equation (52) can predict V_1 and V_2 pretty well at the situation of $T_1 = 1$ but $T_2 \neq 1$.

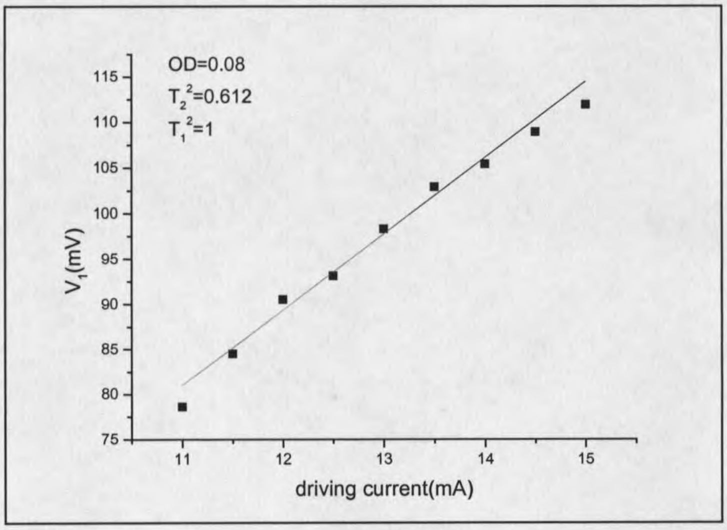

Figure 52. V_1 versus I (the markers are the experimental data, the line is calculated, max. deviation is 3.0%, min. deviation is 0.6%).

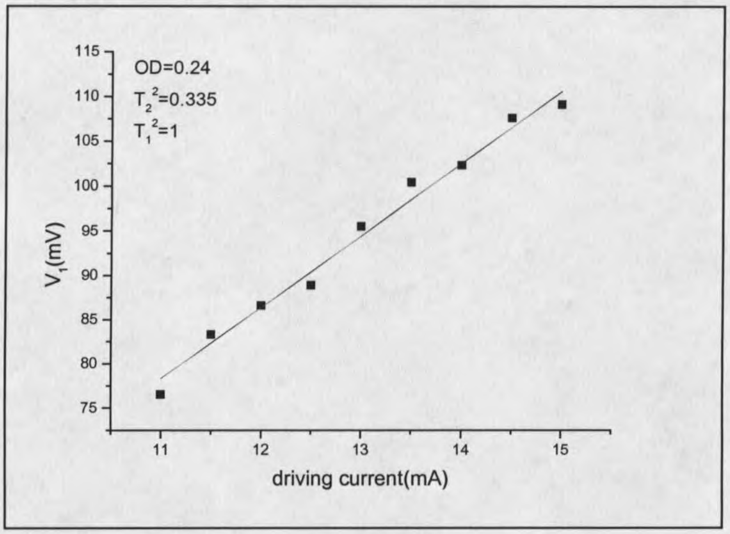

Figure 53. V_1 versus I (the markers are the experimental data, the line is calculated, max. deviation is 3.7%, min. deviation is 0.08%).

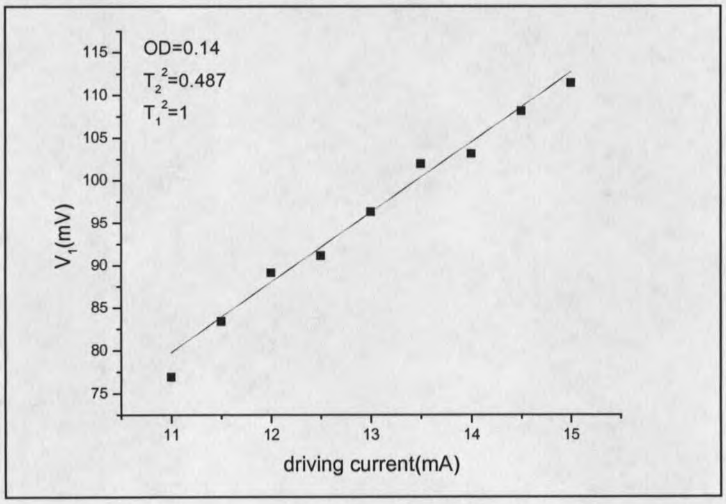

Figure 54. V_1 versus I (the markers are the experimental data, the line is calculated, max. deviation is 2.3%, min. deviation is 1.9%).

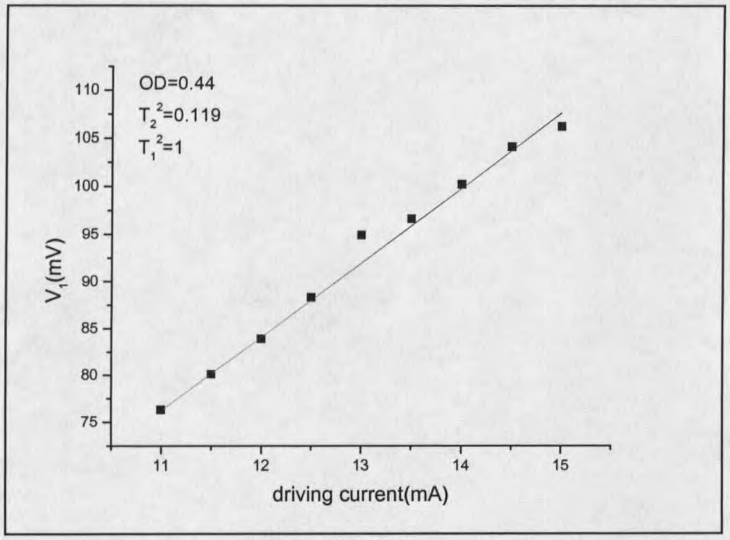

Figure 55. V_1 versus I (the markers are the experimental data, the line is calculated, max. deviation is 2.6%, min. deviation is 1.8%).

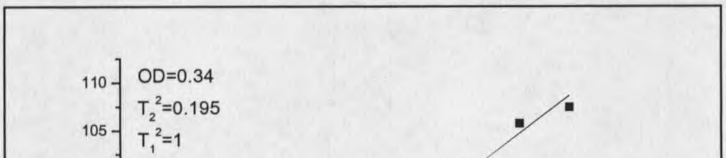

Figure 56. V_1 versus I (the markers are the experimental data, the line is calculated, max. deviation is 3.2%, min. deviation is 0.02%).

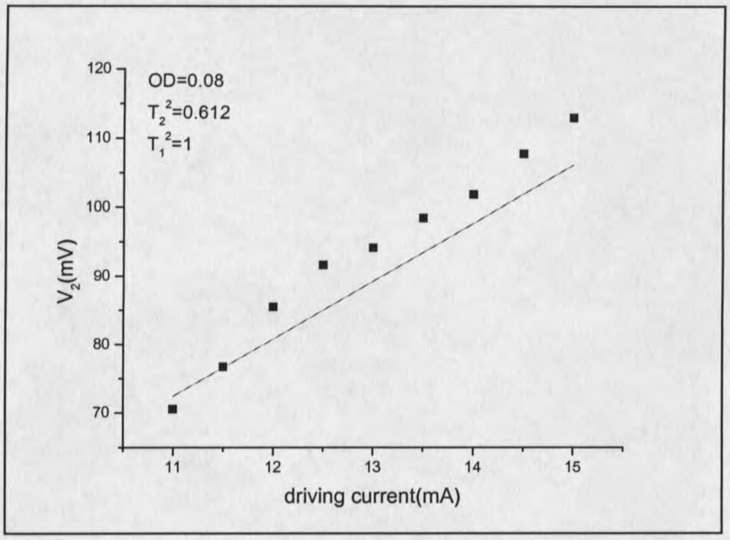

Figure 57. V_1 versus I (the markers are the experimental data, the line is calculated, max. deviation is 2.5%, min. deviation is 1.3%).

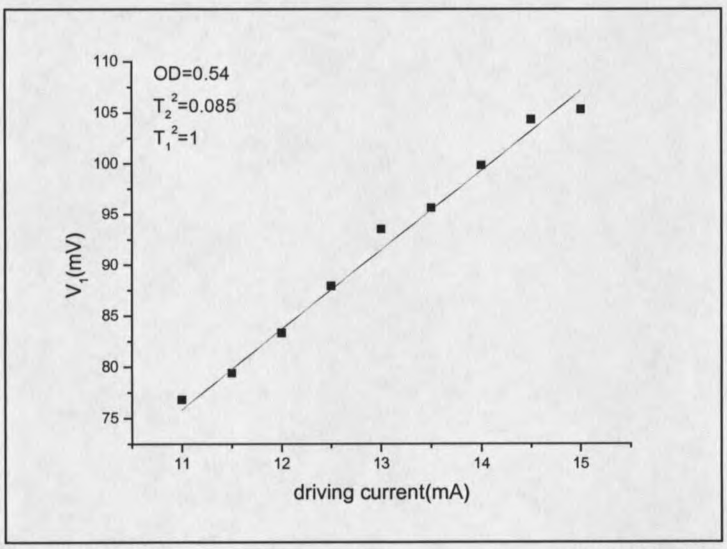

Figure 58. V_2 versus I (the markers are the experimental data, the line is calculated, max. deviation is 7.2%, min. deviation is 0.2%).

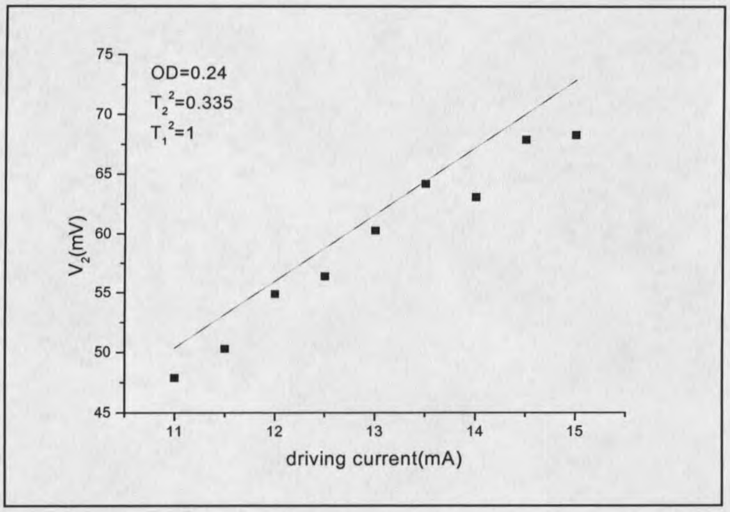

Figure 59. V_2 versus I (the markers are the experimental data, the line is calculated, max. deviation is 3.9%, min. deviation is 0.07%).

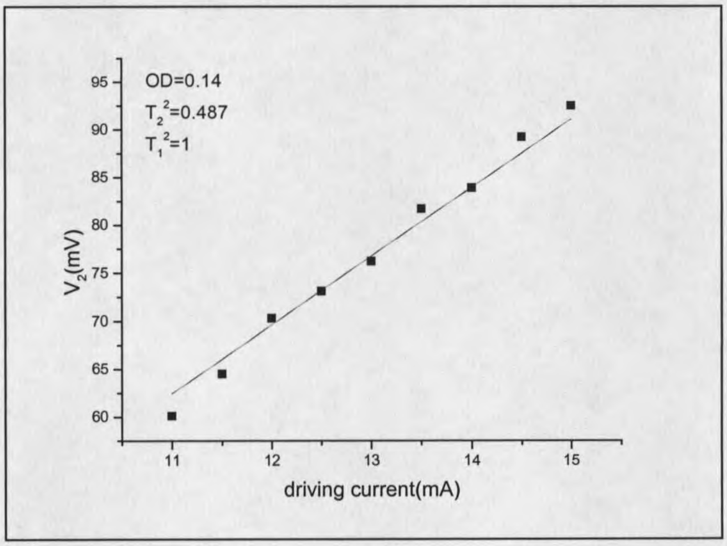

Figure 60. V_2 versus I (the markers are the experimental data, the line is calculated, max. deviation is 6.7%, min. deviation is 0.4%).

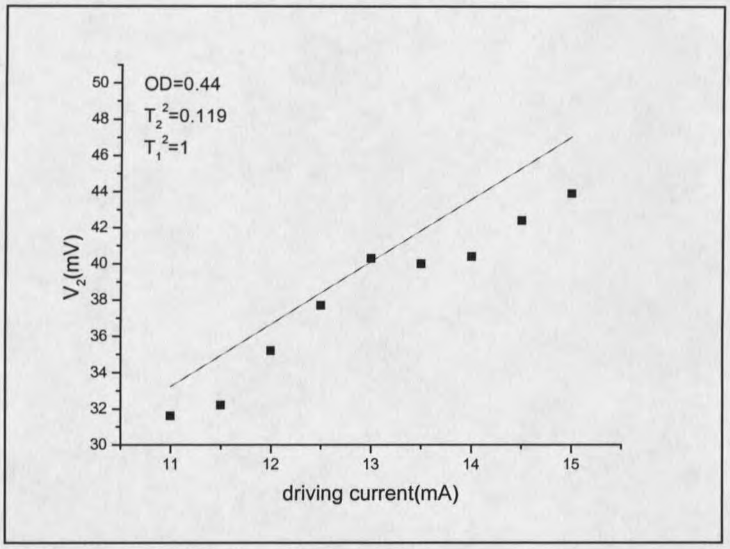

Figure 61. V_2 versus I (the markers are the experimental data, the line is calculated, max. deviation is 11.4%, min. deviation is 3.9%).

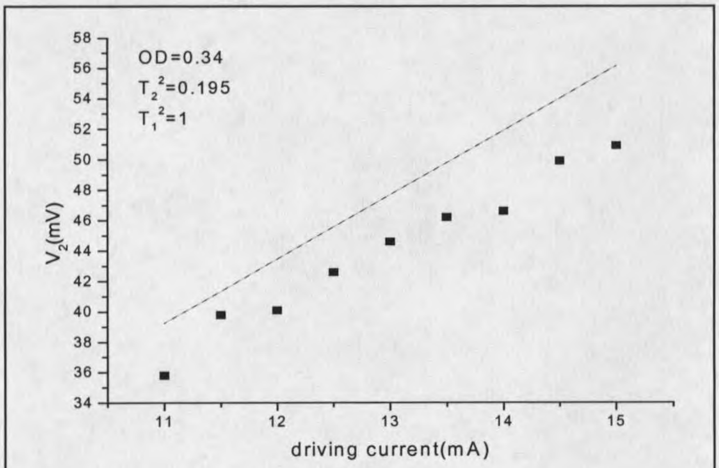

Figure 62. V_2 versus I (the markers are the experimental data, the line is calculated, max. deviation is 8.5%, min. deviation is 0.5%).

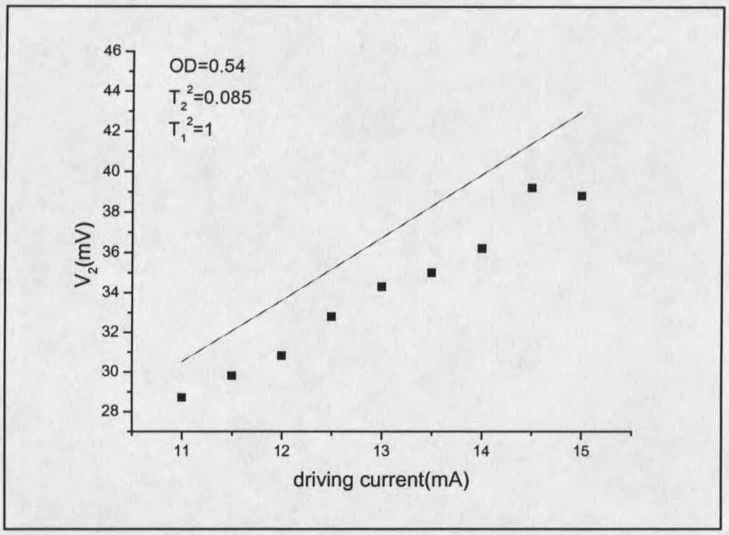

Figure 63. V_2 versus I (markers are the experimental data, the line is calculated, max. deviation is 10.7%, min. deviation is 6.3%).

From the above results, we can see that when the crosstalk of the system is taken into account, V_1 and V_2 are expressed by Equation (51) and (52) respectively. Then, Equation (22) (see end of chapter 2) is modified as Equation (54) by combining Equation (19), (20), (21), (51) and (52).

$$V_{out} = 1.47 - 29.57T_2^2 + 7.37T_1^2 + (V_{ref} - 2.06 + 33.23T_2^2 + 13.13T_1^2) \times \frac{9.02T_2^2 - 5.95T_1^2 + 0.49}{11.13T_2^2 + 8.41T_1^2 + 1.57} \quad (54)$$

Some experiments are done to see if the experimental V_{out} will match the one predicted by Equation (54). In the first experiment, only beam 2 is attenuated by the ND filter. That means in Equation (54) $T_1 = 1$. The OD value is set to 0.34 and S1 in the feedback circuit is turned off. V_{ref} is then set to equal V' which is $134.8mV$. Then, S1 is turned on and the whole feedback loop is connected. The OD value is changed from 0.08 to 0.54 in 0.1 increments. V_{out} is measured and compared to the theoretical value calculated from Equation (54). Figure 64 is the plot for both results. The percentage error is calculated from Equation (53). Table 5 shows the values of V' and percentage deviation from V_{ref} at different OD values. The percentage deviation is calculated from Equation (55).

$$\text{deviation\%}=(V_{ref}-V^{'})/V_{ref}*100\% \qquad (55)$$

Figure 64 shows that the experimental V_{out} matches the theoretical value pretty well. Table 5 shows $V^{'}$ can stay very close to V_{ref}. All these show that the SPSI system works very well.

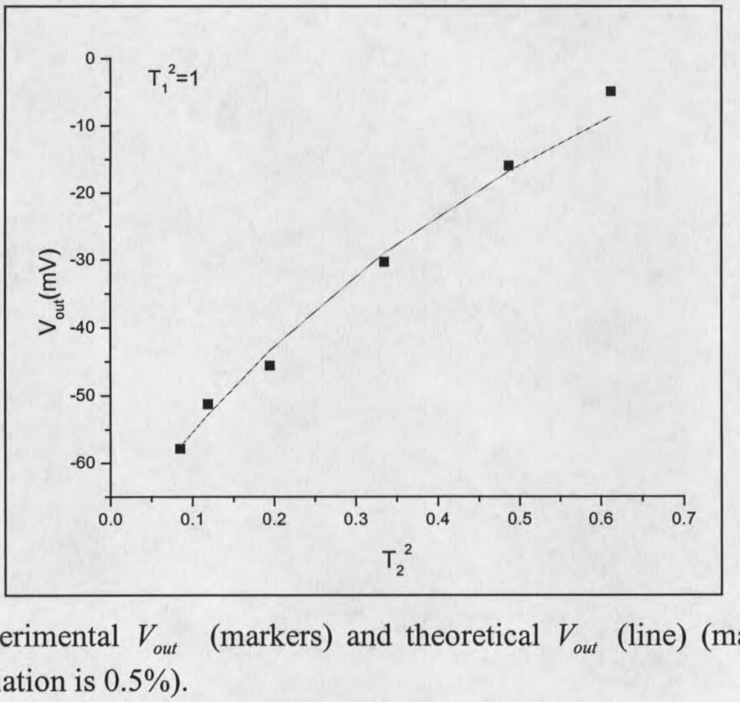

Figure 64. Experimental V_{out} (markers) and theoretical V_{out} (line) (max. deviation is 75.8%, min deviation is 0.5%).

OD value	0.08	0.14	0.24	0.34	0.44	0.54
$V^{'}(mV)$	143	141	136	133	131	129
deviation(mV)	8.2	-6.2	-1.2	1.8	3.8	5.8
deviation%	-6.08%	-4.39%	-0.89%	1.34%	2.82%	4.30%

Table 5. $V^{'}$ values and percentage deviation from V_{ref}.

In the second experiment, only beam 1 is attenuated by the ND filter. That means in Equation (54) $T_2 = 1$. A similar method is used to set V_{ref} to equal V' which is $159mV$. Then S1 is turned on and the whole feedback loop is connected. The OD value is changed from 0.08 to 0.54 in 0.1 increments. Figure 65 is the plot for V_{out}. The percentage error is calculated from Equation (53). Table 6 shows the values of V' and percentage deviation from V_{ref} at different OD values. The percentage deviation is calculated from Equation (55). These results also show that the system is working well.

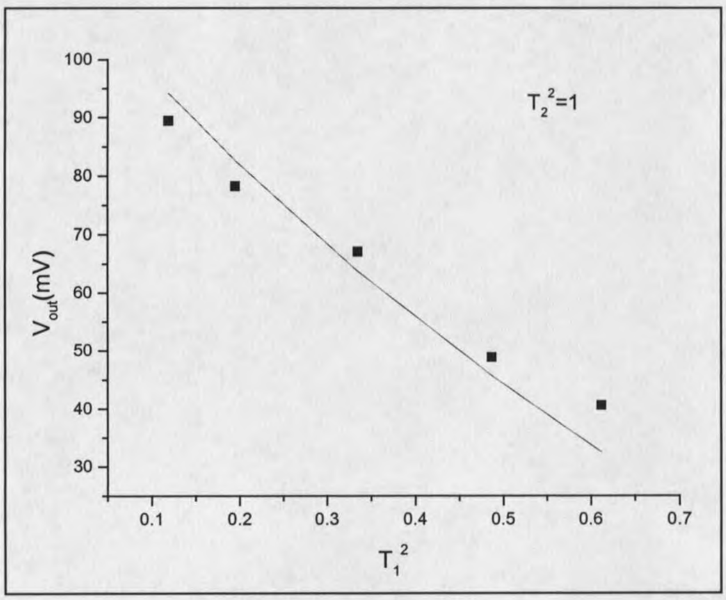

Figure 65. Experimental V_{out} (markers) and theoretical V_{out} (line) (max. deviation is 19.9%, min deviation is 4.5%).

OD value	0.08	0.14	0.24	0.34	0.44	0.54
$V'(mV)$	164	162	159	154	151	150
deviation(mV)	-5	-3	0	5	8	9
deviation%	-3.14%	-1.89%	0.00%	3.14%	5.03%	5.66%

Table 6. V' values and percentage deviation from V_{ref}.

In the third experiment, three different values of ND filter are used to attenuate beam 1. For each value of T_1, the OD value of the filter to attenuate beam 2 is changed from 0.08 to 0.54 in 0.1 increments. Figure 66-Figure 68 are the plots of V_{out}. Table 7-Table 9 show the values of V' at different T_1. From those figures and tables, it can be seem that though the system can not produce as good results as those in the first two experiments, it is still working pretty close to what is expected to do.

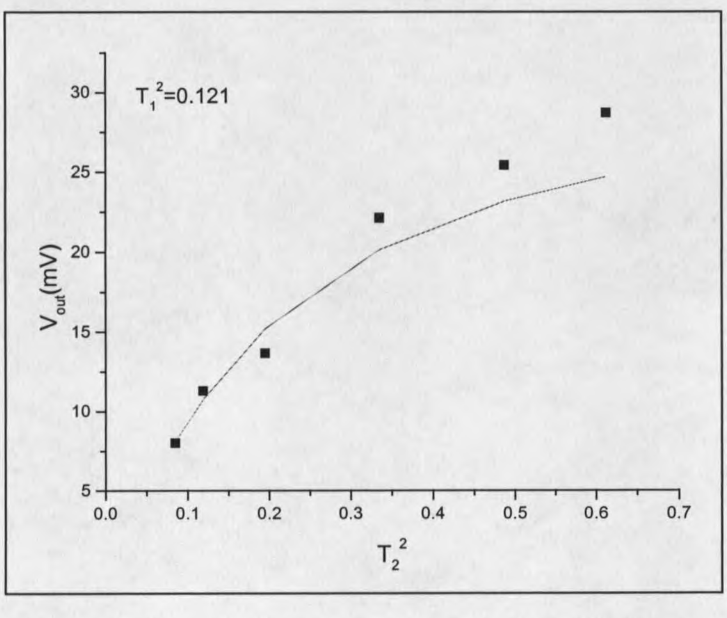

Figure 66. Experimental V_{out} (markers) and theoretical V_{out} (line) max. deviation is 14.0%, min deviation is 0.6%) ($V_{ref} = 52mV$).

OD value	0.08	0.14	0.24	0.34	0.44	0.54
$V'(mV)$	48.8	43.2	37.6	154	151	150
deviation(mV)	-5.2	-4.4	-2.4	0.8	1.6	3.2
deviation%	-10%	-8.46%	-4.62%	1.54%	3.08%	6.16%

Table 7. V' values and deviations from V_{ref} ($V_{ref} = 52mV, T_1^2 = 0.121$).

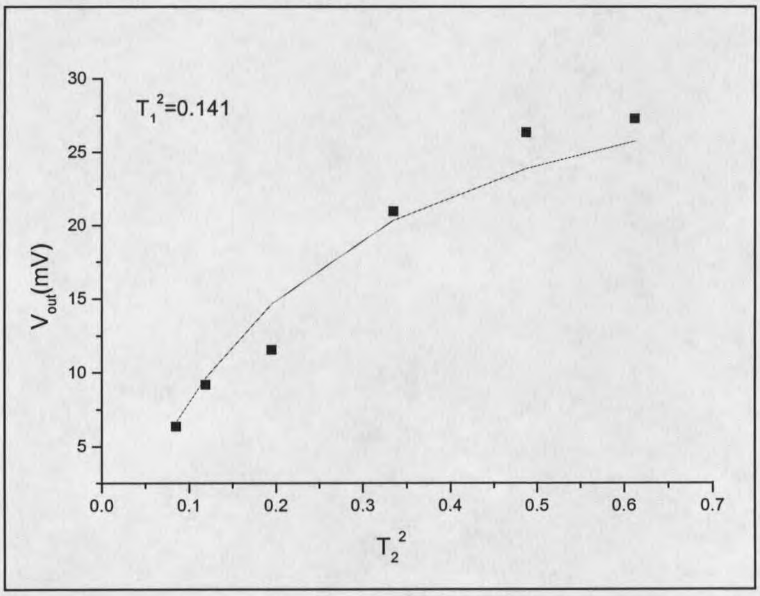

Figure 67. Experimental V_{out} (markers) and theoretical V_{out} (line) (max. deviation is 26.9%, min deviation is 3.9%) ($V_{ref} = 56.4mV$).

OD value	0.08	0.14	0.24	0.34	0.44	0.54
$V'(mV)$	60	59.2	37.6	154	151	150
deviation(mV)	-3.6	-2.8	-1.2	1.6	2.4	3.6
deviation%	-6.38%	-4.96%	-2.13%	2.84%	4.26%	6.38%

Table 8. V' values and deviations from V_{ref} ($V_{ref} = 56.4mV, T_1^2 = 0.141$).

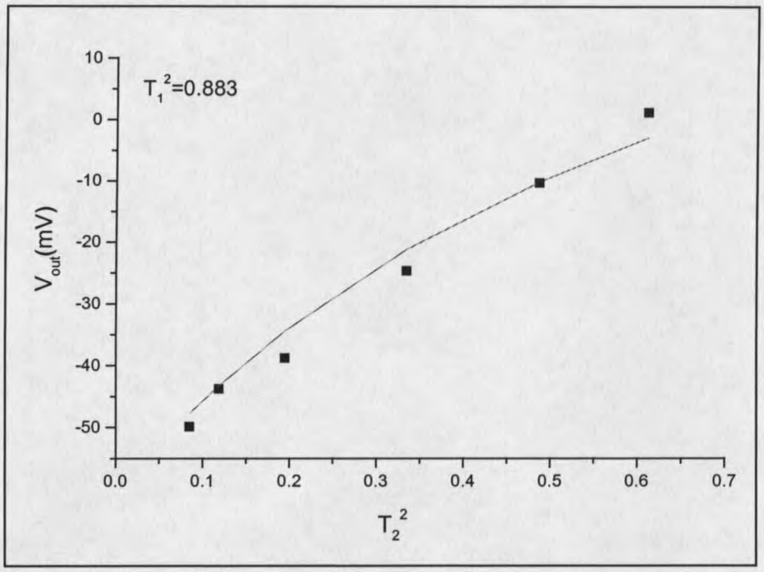

Figure 68. Experimental V_{out} (markers) and theoretical V_{out} (line) (max. deviation is 35.86%, min deviation is 1.06%) ($V_{ref} = 120mV$).

OD value	0.08	0.14	0.24	0.34	0.44	0.54
$V'(mV)$	136	130	126	119	118	117
deviation(mV)	-16	-10	-6	1	2	3
deviation%	-13.30%	-8.33%	-5.00%	0.83%	1.66%	2.49%

Table 9. V' values and deviations from V_{ref} ($V_{ref} = 120mV, T_1^2 = 0.883$).

In the fourth experiment, three different values of ND filter are used to attenuate beam 2. For each value of T_2, the OD value of the filter to attenuate beam 1 is changed from 0.08 to 0.54 in 0.1 increments. Figure 69-Figure 71 are the plots of V_{out}. Table 10-Table 12 show the values of V' at different T_2. The experimental V_{out} of this experiment seems to be off the theoretical V_{out} by a constant. But the slope of the experimental V_{out} and that of the theoretical one match pretty well.

From these four experiments, we mapped out the values of V_{out} at the T_1-T_2 space. The first two experiments mapped out the situation that either T_1 or T_2 equals one, and the last two experiments mapped out the situation that neither T_1 nor T_2 equals one, which shows some possible variations in the T_1-T_2 space. The fact that we got satisfying results from these experiments shows that the single SPSI pixel demonstrated in this thesis is capable of performing normalized differential detection.

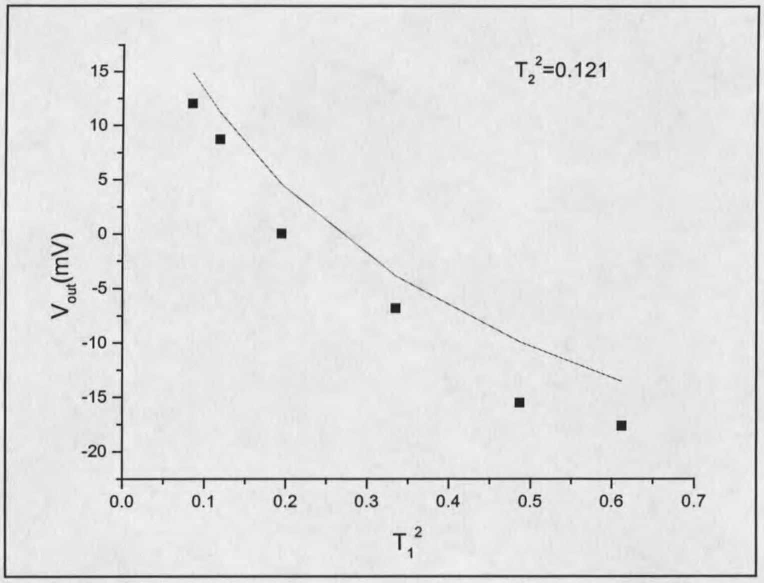

Figure 69. Experimental V_{out} (markers) and theoretical V_{out} (line) (max. deviation is 43.04%, min deviation is 23.20%) ($V_{ref} = 52.4mV$).

OD value	0.08	0.14	0.24	0.34	0.44	0.54
$V'(mV)$	52.8	52.4	52.4	51.2	49.6	46.3
deviation(mV)	-0.4	0	0	1.2	2.8	6.1
deviation%	-0.76%	0.00%	0.00%	2.29%	5.34%	11.60%

Table 10. V' values and deviations from V_{ref} ($V_{ref} = 52.4mV, T_2^2 = 0.121$).

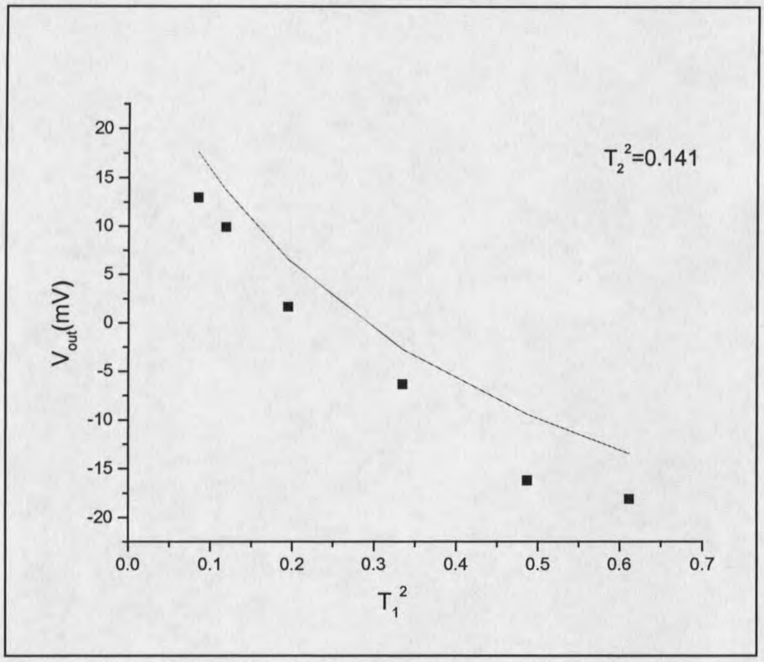

Figure 70. Experimental V_{out} (markers) and theoretical V_{out} (line) (max. deviation is 39.4%, min deviation is 25.4%) ($V_{ref} = 56.8mV$)

OD value	0.08	0.14	0.24	0.34	0.44	0.54
$V^{'}(mV)$	58.4	57.6	56.8	55.2	52.8	48.8
deviation(mV)	-1.6	-0.8	0	1.6	4	8
deviation%	-2.82%	-1.41%	0.00%	2.82%	7.04%	14.08%

Table 11. $V^{'}$ values and deviations from V_{ref} ($V_{ref} = 56.8mV, T_2^2 = 0.141$).

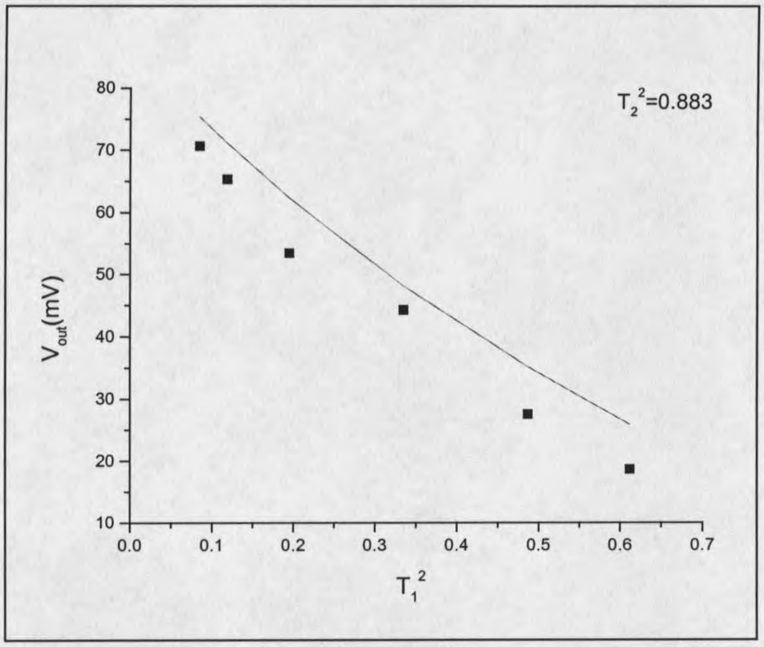

Figure 71. Experimental V_{out} (markers) and theoretical V_{out} (line) (max. deviation is 39.33%, min deviation is 6.67%) ($V_{ref} = 123mV$).

OD value	0.08	0.14	0.24	0.34	0.44	0.54
$V'(mV)$	134	132	129	123	119	119
deviation(mV)	-11	-9	-6	0	4	4
deviation%	-8.94%	-7.32%	-4.88%	0.00%	3.25%	3.25%

Table 12. V' values and deviations from V_{ref} ($V_{ref} = 123mV, T_2^2 = 0.883$).

CHAPTER 5

CONCLUSION

The main spirit of SPSI is to use the electronic signals from the detector as feedback to dynamically control the emitter, and therefore, to dynamically control the illuminations on the scene. If this idea is realized successfully, it will lead to a series of exciting potential applications[20-22]. This thesis uses a single pixel of one kind of SPSI configuration to demonstrate the SPSI idea of normalized differential detection. It experimentally proves this idea is practical.

This thesis first uses a single pixel to illustrate the SPSI idea. Then, two OE chips are characterized, from which the best combination of VCSEL and MSM detectors is chosen for the experiment. An effective alignment procedure is developed and the optical part of the single SPSI pixel is aligned successfully. Two PCB's are designed and built to make up the OE feedback circuit. Due to the existence of different crosstalk in the system, a more sophisticated model is built to describe the system. Sufficient data of different reflectivity situations are taken and compared to the values calculated from the new model. The experimental data match the theoretical ones pretty well, which shows the single SPSI pixel of this configuration does dynamically control the illumination and measure the normalized difference of two reflectivities.

The success of this demonstration enables further research on edge detector. The nearest plan will be to turn on a couple of pixels at a time to detect a sharp change in neighboring reflectivity. Theoretically, the SPSI pixels explored in this thesis will be able to find an edge regardless of overall reflectivity. Experiments need to be done to confirm this in practice.

REFERENCE CITED

REFERENCE CITED

1. P.A. Kiely, G.W. Taylor, D.P. Docter, "Demonstration of a smart pixel using DOES device technology," IEE-Proceedings. -Part-J, -Optoelectronics. 139, 208 (1992)

2. L.A. D'Asaro, L.M.F. Chirovsky, E.J. Laskowski, "Batch fabrication and operation of GaAs-AlxGal-xAs field-effect transistor-self-electrooptic effect device (FET-SEED) smart pixel arrays," IEEE-Journal-of-Quantum-Electronics. 29, 670 (1993)

3. P. Clarke, "Technology focus: optical computing," Electronic-Engineering. 66, 31 (1994)

4. M. Welker, B. Knupfer, S. Malzer, "Smart pixel using a vertical cavity surface-emitting laser," Applied-Physics-Letters. 71, 3561 (1997)

5. T. Kurokawa, S. Matso, T. Nakahara, "Design approaches for VCSEL's and VCSEL-based smart pixel toward parallel optoelectronic processing systems," Applied-Optics. 37, 194 (1998)

6. B.L. Shoop, R.W. Sadowski, G.P. Dudevoir, "Smart pixel technology and an application to two-dimensional analog-to-digital conversion," Optical-Engineering. 37, 3175 (1998)

7. T.J. Cloonan, G.W. Richards, A.L. Lentine, "A complexity analysis of smart pixel switching nodes for photonic extended generalized shuffle switching networks," IEEE-Journal-of-Quantum-Electronics. 29, 619 (1993)

8. T.K. Woodward, A.L. Lentine, L.M.F. Chirovsky, "Experimental sensitivity studies of diode-clamped FET-SEED smart-pixel optical receivers," IEEE-Journal-of-Quantum-Electronics. 30, 2319 (1994)

9. J.S. Kane, T.J. Grycewicz, T.G. Kincaid, "Realizing optical logic with a smart-pixel spatial light modulator," Applied Optics. 35, 1249 (1996)

10. Y.J. Wang, Z.Y. Guo, Y.X. Zhang, "Liquid crystal smart pixel neuron array," Optical-Engineering. 36, 2074 (1997)

11. T.M. Slagle, K.H. Wagner, "Optical smart-pixel-based Clos crossbar switch," Applied-Optics. 36, 8336 (1997)

12. J.S. Kane, "A smart pixel-based feedforward neural network," IEEE Transactions on Neural Networks. 9, 159 (1998)

13. J.S. Kane, T.G. Kincaid, P. Hemmer, "Optical processing with feedback using smart-pixel spatial light modulators," Optical-Engineering. 37, 942 (1998)

14. D.V. Plant, A.Z. Shang, M.R. Otazo, "Design, modeling, and characterization of FET-SEED smart pixel transceiver arrays for optical backplanes," IEEE Journal of Quantum Electronics. 32, 1391 (1996)

15. D.R. Rolston, B. Robertson, H.S. Hinton, "Analysis of a microchannel interconnect based on the clustering of smart-pixel-device windows," Applied Optics. 35, 1220 (1996)

16. T.M. Pinkston, C. Kuznia, "Smart-pixel-based network interface chip," Applied Optics. 36, 4871 (1997)

17. W.C. Holton, "Free-space interconnects pick up speed," Laser-Focus-World. 34, 34+ (1998)

18. B. Robertson, "Design of an optical interconnect for photonic backplane applications," Applied Optics. 37, 2974 (1998)

19. E.J. Lerner, "Smart-pixel optical processors clear traffic jams," Laser-Focus-World. 35, 129 (1999)

20. W.R. Babbitt, R.B. Darling, "Efficient optical sensor design for multi-function integrated emitter-detector arrays," Optics in Computing. 8, 61 (1997)

21. M. Azadeh, W.R. Babbitt, R.B. Darling, "Smart pixels with smart illumination," Optical Society of America Annual Meeting. Oct. 12-17 (1997)

22. M. Azadeh, W.R. Babbitt, R.B. Darling, "Smart pixels with smart Illumination," Optics Letters. 23, 786 (1998)

23. W. Lauterborn, T. Kurz, M. Wiesenfeldt, "Coherent Optics," (Springer-Verlag Berlin Heidelberg New York, 1999), p.152-155, p.164-166.

24. B.E.A. Saleh, M.C. Teich, "Fundamentals of photonics," (Wiley and Sons, N.Y., 1991), p.85-86.

25. K. Repasky of Montana State University designed the optical part of the single SPSI pixel in this thesis.

26. J. Jahns, B.A. Brumback, "Integrated-optical split-and-shift modulate based on planar optics," Optics Communications. 76, 318 (1990)

27. B.E.A. Saleh, M.C. Teich, "Fundamentals of photonics," (Wiley and Sons, N.Y., 1991), p.92-100.

28. The contact person for the information of the microlens is Dr. Charlie Kuznia of University of Southern California. His phone number is (213) 740 4143.

29. B.E.A. Saleh, M.C. Teich, "Fundamentals of photonics," (Wiley and Sons, N.Y., 1991), p.95, 141-143, 371.

30. Wavelength Electronics Laser Diode Drivers Manual, p.5.

APPENDIX

ELECTRONIC FEEDBACK CIRCUIT

APPENDIX

ELECTRONIC FEEDBACK CIRCUIT

Figure 72 is the actual feedback circuit. The OP-497 is a quad op amp that provides the combination of exceptional precision with low power and extremely low input bias current. The OP-97 is a low-power precision amplifier. The AMP04 is an instrument amplifier that offers an excellent combination of accuracy, low power consumption, wide input voltage range, and excellent gain performance. There are only 4 chips in the whole circuit, which makes the circuit simple and therefore reduces noise. From left to right in Figure 72, the first stage using the OP-497 is a subtractor to subtract dc background from the input. Inputs V_1' and V_2' are the voltage outputs of the detectors. The first AMP04 calculates the difference between V_1 and V_2. With the variable resistor, the gain of the first AMP04 can change from 2 to 10. The third OP497 add V_1 and V_2 to yield V'. By adjusting the potentiometer, the last OP-497 will produce different value of V_{ref}. The last AMP04 calculate the difference between V' and V_{ref} as Equation (52). G is the gain of AMP04 and is determined by Equation (A-1). R_{gain} is equal to 100Ω plus the percent value of the $50k\Omega$ potentiometer in this circuit. G can be varied from 2 to 1000 by adjusting the potentiometer.

$$G = 100k\Omega / R_{gain} \qquad \text{(A-1)}$$

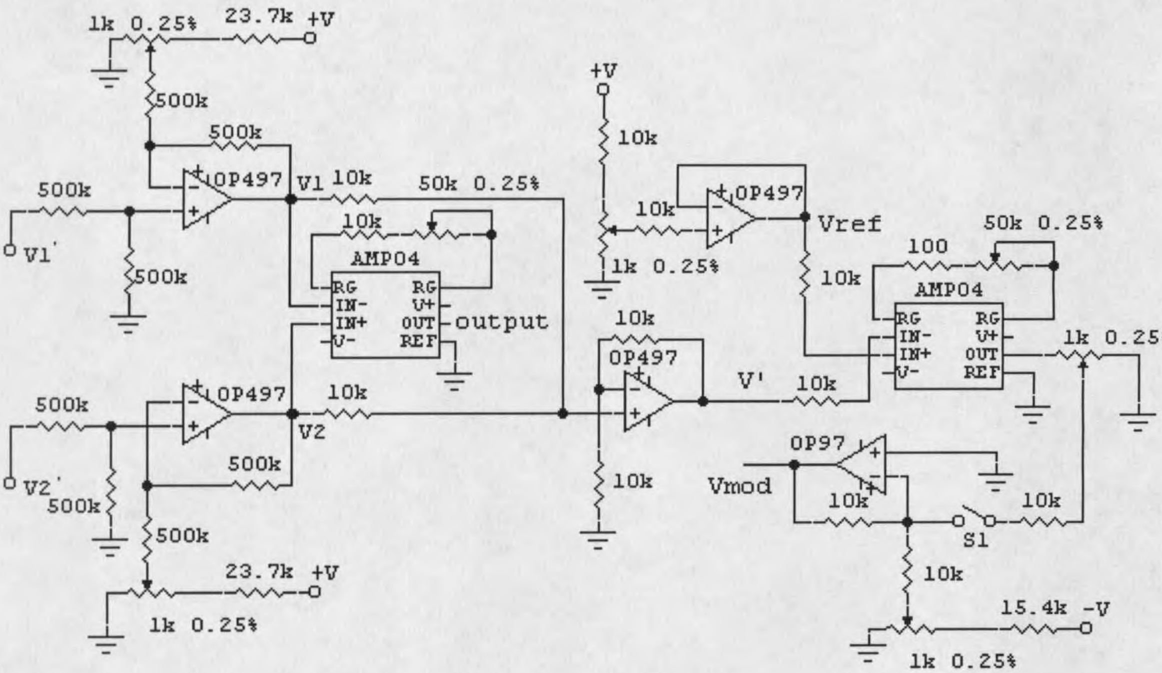

Figure 72. Schematic of the actual electronic feedback circuit.